Negative Ion Photoelectron Imaging Spectroscopy of Iodine Monobromide and Copper Hydrides

by

Ryan M. D. Calvi

B.S., University of California Santa Barbara, 2004

A thesis submitted to the

Faculty of the Graduate School of the

University of Colorado in partial fulfillment

of the requirements for the degree of

Masters of Science

Physical Chemistry

2007

This thesis entitled:

Negative Ion Photoelectron Imaging Spectroscopy of

Iodine Monobromide and Copper Hydrides

Written by Ryan M. D. Calvi

has been approved for the Physical Chemistry program by

_____

W. Carl Lineberger

_____

Mathias J. Weber

Date: _____

The final copy of this thesis has been examined by both the signatories, and we find that both the content and the form meet acceptable presentation standards of scholarly work in the above mentioned discipline.

Calvi, Ryan M. D. (M.S. Physical Chemistry)

Negative Ion Photoelectron Imaging Spectroscopy of Iodine Monobromide and Copper Hydrides

Thesis directed by W. Carl Lineberger

This thesis contains the results of several negative ion photoelectron spectroscopy experiments performed on two types of anions. The first class of anions studied consisted of copper containing complexes, including CuH^-, CuD^-, CuH_2^-, CuD_2^-, and $CuCD_3O^-$. The photoelectron spectra of these molecules allowed us to measure (for the first time) the electron-binding energies of the ground and excited states of the neutrals as well as the electron affinities when possible. Franck-Condon simulations were performed on the molecules to determine the bond length change between the anion and neutral. A predicted but until now unobserved, **a** $^3\Sigma^+$ excited state of CuH and CuD is seen in the anion spectra; the electron affinity is measured as 0.444(6) eV for CuH. The spectra of CuH_2^- and CuD_2^- allow us to study the neutrals for the first time; two geometric isomers are present in the spectra. The CuH_2^- photoelectron spectrum is dominated by a strong transition to the linear excited $^2\Sigma_g$ state and accompanied by an extended weak-unresolved vibrational progression involving the bent ground $^2B_2$ state. *Ab initio* calculations of the 0.255 eV energy difference between these two states show EA(CuH_2) to be 2.60(5) eV. Copper methoxy is only briefly presented as a detailed analysis will follow in a subsequent publication; however, a measured electron affinity of 1.077 eV is determined for this molecule from the photoelectron spectra presented here.

The second type of molecule studied is the heterodiatom IBr. The photoelectron spectra of the IBr anion are characterized by three distinct electronic states. An extended vibrational progression is present for the ground state in the neutral, which lacked a distinct

origin; it is caused by a shortening of the bond length between the anion and the neutral. Several excited states are present in the spectra, providing confirmation to previous experimental results. The IBr^- photoelectron spectrum exhibits transitions to the ground (**X** $^1\Sigma$) and lowest-excited triplet **A** $^3\Pi_1$ and **A** $^3\Pi_2$ states. Previous experimental results of the term-splitting energy between the ground $^1\Sigma$ and excited $^3\Pi_1$ states of 1.525 eV give an electron affinity of 2.51(1) eV. The vibrational progression observed in the excited states matches extremely well to previous results, confirming the correct identification of the electronic states.

Acknowledgments

I would like to thank my parents Wendy and David Calvi who have supported my educational goals since I started elementary school. They never looked down on my choices and always allowed me to strive for the best. They have been a real motivating factor in my success and achievements; they have sacrificed some of their ambitions to help me attain mine, and for that I must thank them for all they have done.

I would like to thank Professor Alec Wodtke at the University of California at Santa Barbara who took me in as a young undergrad and got me excited about the world of gas-phase physical chemistry. Without the opportunities I obtained working in his lab, I would not have been able to advance as quickly as I have. I learned a lot, but it was only a drop in the bucket compared to what I ended up learning about experimental design and performing experiments.

W. Carl Lineberger has been the greatest influence in my educational endeavors I knew that Carl was the one I wanted to work for when I entered graduate school. He took me in and let me run wild. It was in his lab that I really learned how to carefully design an experiment and see it through from conception to completion. Whenever there was a problem in lab, he always had an idea for problem solving. Even if we thought we had tried everything else, there was always something more that could be done. Even with his hectic travel schedule, he always had time to sit down and figure out what was going on, even if I had no idea. He has been supportive of my decision to leave graduate school to pursue my other educational goals, while still allowing me to work in his lab. I thank him for that.

I also thank Django Andrews, Jeff Rathbone, and Lenny Sheps. Without these three individuals, none of this work would have been possible. They are the ones who really took the time to allow me to learn the experiment and figure out all the intricacies that are usually

left out. Having spent many of hours with me, they have become great friends. They know what they are doing and will succeed in their future endeavors.

None of this work would be possible without support from the JILA instrument and electronic shops. Tom Foote and Hans Green of the instrument shop have done so much for our lab. They always provide ideas that are practical and inventive saving us from strategies that otherwise would be very complex and prone to failure. James Fung-A-Fat in the electronics shop has been instrumental in the design of many of the circuits in our lab; without his help, many things would not have been done as well as they were.

Contents

List of Figures and Tables

Introduction to Negative Ion Photoelectron Spectroscopy

1.1 Overview of Negative Ion Photoelectron Spectroscopy

Negative ion photoelectron spectroscopy (PES) has allowed for the study of the structures and energetics of anion and neutral molecules.[1] Important measurements obtained from negative ion photoelectron spectroscopy are the electron binding energies, more specifically the electron affinity of the neutral molecule.[2] Using the measured electron affinity allows for the determination of bond strengths in the neutral and anion molecule. Vibrational frequencies of neutral molecules can be extracted from vibrational progressions present in the spectra, while the vibrational frequencies of the anion can be determined from vibrational hot bands, if present. The electronic-term splitting energies of different electronic states in the neutral molecule such as spin-orbit splittings and bond lengths of both the anion and neutral can be measured. An advantage of negative ion PES over traditional spectroscopic methods is in the study of reactive/metastable neutral species formed via the photodetachment of the precursor anion. These species cannot otherwise be directly prepared. In photoelectron spectroscopy, the spin of the molecule must change when the electron is photodetached, $\Delta S=1/2$, which is not the case in optical spectroscopy. This change in spin allows access to a greater number of electronic states. The neutral is formed by photodetachment of the anion at the vertical detachment geometry on the neutral surface.

Negative ion photoelectron spectroscopy can be simply described by the process:

$$AB^- + h\nu \rightarrow AB + e^-(eKE), \qquad (1.1)$$

where AB^- is the molecular anion, $h\nu$ is the photon energy utilized in the photodetachment, AB is the photodetached neutral, and $e^-(eKE)$ is the photodetached electron, which receives all of the recoil kinetic energy. Which knowledge of the energy of the molecular anion and a

well-defined narrow photon source, measurement of the kinetic energy of the photodetached electron will give a direct energy separation between the initial electronic states of the anion and the final electronic states of the neutral. The term reported by the measured electron kinetic energy is the electronic-binding energy (eBE). The relationship between the electron kinetic energy and binding energy is given by

$$eBE = h\nu - eKE, \qquad (1.2)$$

where the electron binding energy (eBE) is found by subtracting the electron kinetic energy (eKE) from the photon energy. The electron-binding energy is reported to allow a direct comparison of photoelectron spectra independent of photon energy. Transitions to excited states of the neutral molecule are accomplished by changing the photon energy to meet or exceed the term-splitting energy. This process is diagramed in Figure 1.1. The process can be conceptualized as; a photon comes into the molecular anion and excites it to a continuum level, i.e. the photon energy. Subsequently, the molecule relaxes into a given electronic state and vibrational level. The excess energy between the continuum level and that of the relaxed state is transferred to the photodetached electron.

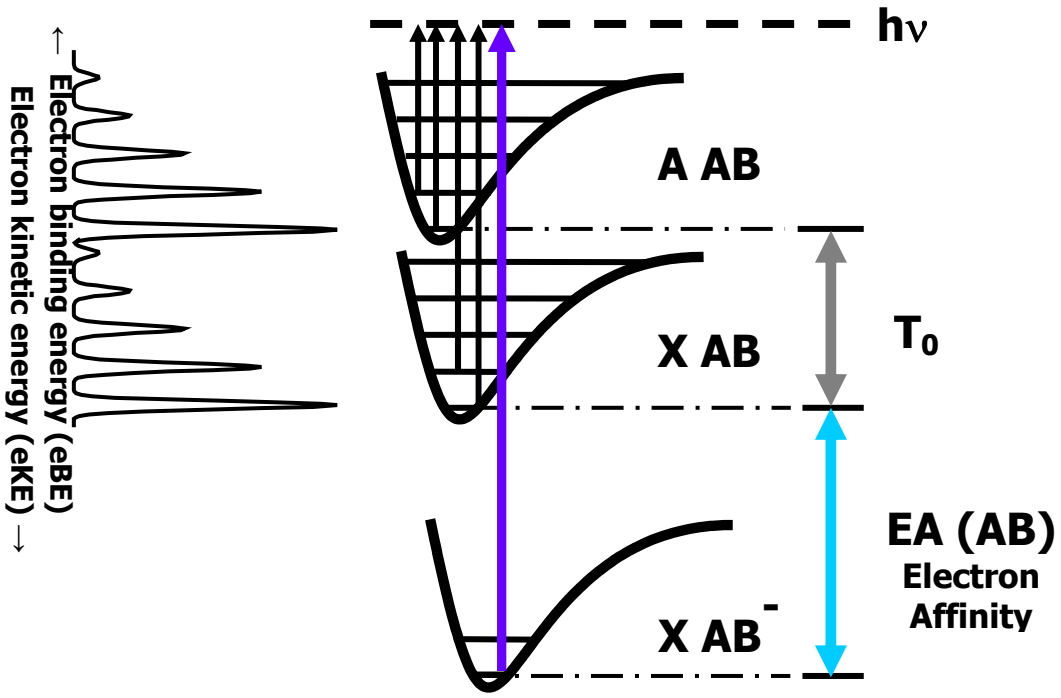

Figure 1.1 Schematic diagram depicting processes and energies present in photoelectron spectra.

In Figure 1.1, the anion state is represented by AB^-. The absorption of the incoming photon is the upward arrow to the continuum level, labeled hν. The kinetic energy given to the ejected electron is proportional to the length of the arrows between the continuum level and the level the neutral molecule resides on. The longer the arrow, the more kinetic energy is imparted to the ejected electron. The adiabatic electron affinity of the neutral molecule is the energy measured directly between the two ground vibrational states of the anion and neutral. If the photon energy is sufficient to access higher electronic states of the neutral, the splitting of the states can be measured (represented as T_0 in Figure 1.1). The photoelectron spectrum on the left side of Figure 1.1 is a schematic diagramming the spacing between the vibrational levels. It is what a "typical" spectrum collected looks like.

1.2 Franck-Condon Profiles

The Franck-Condon principle constrains the geometries of the anion and the neutral to be equal during photodetachment. For anions and neutrals with similar equilibrium geometries, the electron affinity can be measured as a transition between the lowest vibrational energy levels of the ground state of the two species. When the equilibrium geometries are significantly different, this transition is very weak and usually unobserved in the spectra. In this case, the vertical detachment energy (VDE) is then reported as the transition from the ground state of the anion to a vibrationally excited state in the neutral with the same geometry as the anion. The quantum mechanical version of the Franck-Condon principle is based on the fact that the intensity of a given transition is proportional to the square of the integral overlap between the two states:[1,3]

$$M_{e\nu} = |\langle \Psi' | \Psi'' \rangle|^2 . \qquad (1.3)$$

The Franck-Condon factor determines how the intensity is distributed among the vibrational bands. The intensity of the vibrational bands of an electronic transition is determined by the population of the vibrational levels, the strength of a transition, and the Franck-Condon factors. Here Ψ' is the vibrational wave function of the final neutral state, and Ψ'' is the vibrational wave function of the initial anion state. Governed by symmetry, only transitions to and from totally symmetric vibrational levels or even quanta of nonsymmetric modes are allowed.

1.3 Photoelectron Angular Anisotropy Parameter

Photoelectron angular distributions are also obtained from photoelectron spectra and used to determine the anisotropy parameter, β. The anisotropy parameter reflects the symmetry of the electronic orbital from which the electron is photodetached. β is rigorous for atomic systems, but is less exact for molecular systems. The β parameter is given by

$$I(\nu,\theta)=(\frac{1}{4\pi})f(\nu)(1+\beta\ P_2(\cos\theta)), \qquad (1.4)$$

where θ is the angle between the **ε** vector of the photolysis laser radiation and the direction of photofragment recoil, f(ν) is the speed distribution of the detected photofragment, β is the anisotropy parameter, and $P_2(\cos\theta) = \frac{3\cos^2\theta - 1}{2}$ is a second-order Legendre polynomial.[4] β ranges between −1 and +2 depending on the prompt dissociations following, respectively, a purely parallel, ΔΩ =0, or a purely perpendicular ΔΩ=±1, excitation of the parent diatomic molecule. Electrons photodetached from s orbtials in the case of atomic systems and Σ orbitals in a molecular system have positive β values. Electrons detached from p or d atomic orbitals and Π or Δ molecular orbitals have a negative β value.[4] We use the β parameter of features in the photoelectron spectra to assign transitions to different electronic states of the neutral.

1.4 Photoelectron Imaging

Imaging techniques for molecular spectroscopy were first conceived by Houston and Chandler for photo fragments formed from the photodissociation of neutral molecules.[5] Such images simultaneously provide full three-dimensional velocity distributions of all photodetached species imaged. From these, the individual velocities (kinetic energies) and angular distributions can be obtained. The photoelectron images are used to reconstruct the photoelectron energy spectra. In addition, they contain the photoelectron angular distributions, which are now observable in the images and necessary for obtaining the β values. Both the electron kinetic energies and angular distributions are obtained simultaneously, allowing for an enormous amount of information to be continuously collected.

Imaging resolution increased dramatically with the development of velocity-map imaging by Parker and Eppink.[6] Prior to the development, images were often blurred because of the extended, nonpoint source of the anions from which photodetachment occurs. Image quality is dependent on how three-dimensional photoelectron distributions are mapped onto a two-dimensional detector. A three-element open-electrode configuration was found to minimize imaging distortions by acting as a lens. Parker and Eppink determined that when appropriate voltages are applied to the respective electrodes, particles with the same initial velocity vector are mapped onto the same point of the detector, regardless of their initial position upon photodetachment. This method gives rise to the term velocity-map imaging. Utilizing a velocity-map imaging configuration allows for high quality images to be acquired, even with the presence of an extended ion source.

1.5 Image Reconstruction

The image acquired is not a full representation of the three-dimensional electron distribution necessary to obtain the photoelectron spectra and angular distributions. To

reconstruct the three-dimensional distribution from the two-dimensional projection on the detector, cylindrical symmetry must exist for the reconstruction of the image by use of the Abel integral. This cylindrical symmetry requirement requires that the photodetachment laser polarization be parallel to the plane of the detector. The Abel transformation can lead to significant artifacts in the reconstruction. However, a new method, was developed by Reisler and co-workers, known as the basis set expansion (BASEX) method.[7] The BASEX method is able to produce higher quality reconstructions while avoiding the mistakes of the Abel transformation. This method expands the two-dimensional image projection in a basis set of well-behaved Gaussian-like functions. The full three-dimensional distribution is then reconstructed as a linear combination of these well-behaved functions. The BASEX software takes a two-dimensional slice through the three-dimensional distribution reconstruction from which the photoelectron spectrum as a function of camera pixels is produced, and the values of β as a function of pixels are calculated.

1.6 Thesis Overview

This thesis contains the photoelectron spectra of two different types of molecular species collected with a pulsed-ion source that utilizes a velocity map-imaging spectrometer to measure the photodetached-electron kinetic energy. The experimental apparatus and laser system, along with the theory explaining the experiment are described in Chapter 2.

The first system presented here addresses the solvation dynamics of $IBr(CO_2)_n$, n=0-16 and includes the photoelectron spectra of the bare IBr molecule. An updated measurement of the electron affinity is reported. The results of this study are presented in Chapter 3.

The second system presented addresses copper monohydride (CuH^-) and copper dihydride (CuH_2^-). The electronic structures and vibrational frequencies of the molecules are presented and compared to high-level theoretical calculations. The electronic affinities of

these molecules are reported here. A low-lying triplet state in the copper monohydride is observed for the first time is reported in Chapter 4.

The last system presented in this thesis addresses the copper methoxy anion ($CuCH_3O^-$). The photoelectron spectrum is briefly mentioned. The binding energies and vibrational frequencies are listed in Chapter 5.

References for Chapter I

1 *Advances in Gas Phase Ion Chemistry*, edited by N. G. Adams and L. M. Babcock (JAI Press Inc., 1992), Vol. 1.

2 S. J. Blanksby and G. B. Ellison, Accounts of Chemical Research **36** (4), 255 (2003).

3 P. F. Bernath, *Spectra of atoms and molecules*. (Oxford University Press, New York, 1995).

4 R. N. Zare, *Angular Momentum*. (Wiley, New York, 1988).

5 *Imaging in Molecular Dynamics Technology and Applications*, edited by B. Whitaker (Cambridge University Press, 2003).

6 A. Eppink and D. H. Parker, Review of Scientific Instruments **68** (9), 3477 (1997).

7 V. Dribinski, A. Ossadtchi, V. A. Mandelshtam, and H. Reisler, Review of Scientific Instruments **73** (7), 2634 (2002).

Experimental Setup

2.1 Velocity Map-Imaging Photoelectron Spectrometer Overview

The photoelectron velocity-map imaging apparatus is diagrammed in Figure 2.1, although it has been described in some detail in previous publications,[1-3] an overview will be presented here. All experiments were performed in a Wiley-McLaren-type time-of-flight photoelectron-imaging spectrometer[4] and a velocity map-imaging photoelectron detection region.[5,6] The apparatus consists of three regions within our chamber. The first region contains the source of the negative ions, the second contains the ion-optics and a drift tube for mass separation, and the third consists of an interaction and detection region, where the velocity map imaging setup is housed. The detection region is isolated from the first two sections by a pneumatically operated gate valve. The two anion sources utilized in these experiments are described in Section 2.2. The Wiley-McLaren time-of-flight mass spectrometer is described in Section 2.3 and the velocity map-imaging detector in Section 2.4. A brief overview of the laser system utilized in the experiments is given in Section 2.5, and the reconstruction of the collected images and data analysis are presented in Sections 2.6 and 2.7, respectively.

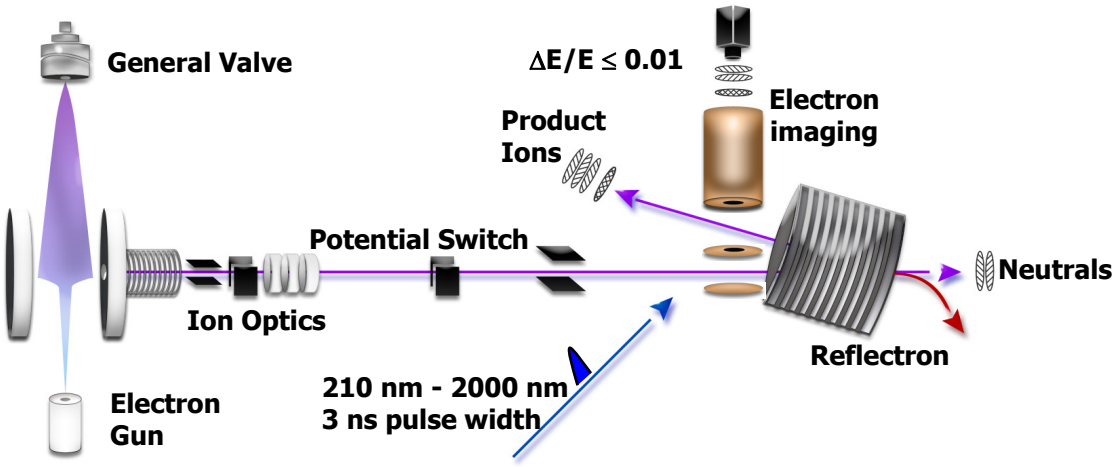

Figure 2.1 Photoelectron velocity map imaging spectrometer

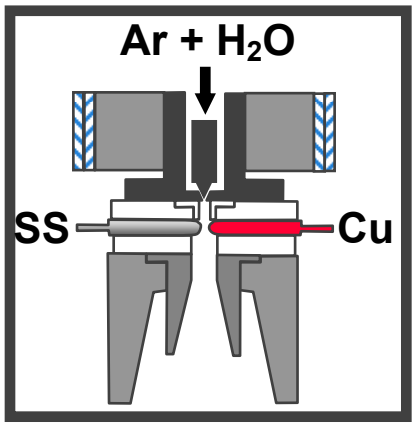

Figure 2.2 Sputter source utilized in the anion copper studies, a Stainless Steel (SS) rod is held at ground potential, while the copper (Cu) rod is held at –3 kV.

2.2 Velocity-Map Imaging Ion Sources

The purpose of the source chamber is to create the negative ions under investigation. The formation of negative ions consists of mixing a backing gas seeded with trace amounts of our molecule or precursor of interest. Typical backing pressures range from 5 to 45 psi. The gas mixture is pulsed into the source chamber using a General Valve (Series 9) with a nozzle diameter of 800 μm. The General Valve is driven by a single-channel Iota One pulse drive made by Parker and Hannifin. Typical base pressures in the source chamber prior to pulsing are 4×10^{-7} torr; typical pressures while pulsing the General Valve are 2×10^{-5} torr.

Formation of the negative ions utilized in the case of the copper complex studies includes a dc discharge sputtering-ions source, (Figure 2.2) or, in the case of the IBr studies, a homemade electron gun.

After the dc discharge sputtering-ion source is fitted to the General Valve, the emerging molecular beam initiates a discharge across a gap of 1.0 mm between a copper cathode at −3 kV and a stainless steel pin, held at ground potential. This discharge produces Cu^- anions and small clusters. The sputtered-plasma produces significant quantities of copper anions, and molecular anions are formed during the expansion of the plasma. The anions produced in the plasma are cooled and stabilized inside a cone-shaped expansion channel and then allowed to expand into the source chamber.

The second of our two ion sources is a homemade electron gun, which is positioned in the chamber to be collinear with the molecular jet pulse from the General Valve. The electron gun consists of a thoriated-tungsten filament, which is focused utilizing an Einzel lens and steered using a set of vertical and horizontal deflectors. Electrons are emitted by resistively heating the thoriated tungsten filament by passing 5.5 amps through the filament. The ejected electrons are repelled by a plate biased at −100 V relative to the filament. The filament and anode power supplies are floated at 1 kV. The Einzel lens is composed of three

annuli with the first and third held at ground potential and the middle annulus biased between 900 and 1100 V. The electron beam is steered via a set of vertical and horizontal deflectors. Different pairs of deflectors have a typical potential difference of 0—30 V. The electron beam is measured daily with a Faraday cup, yielding an average reading of 320 μA. The electron beam is focused into the General Valve with a 5 mm thick samarium-cobalt magnet annulus mounted to the front of the pulsed-valve face plate.

Producing IBr^- is done by attachment of slow secondary electrons. The slow secondary electrons are produced by interaction of an electron beam with a CO_2 molecule acting as moderator. The first mechanism is rather straightforward and is responsible for the formation of dihalide anion clusters. A particular anion, IBr^- for example, is formed by attachment of secondary electrons to the neutral dihalide species found in the expansion. Cluster growth then occurs as the solvent molecules (CO_2 in this case) condense around the newly formed charge centers by the following mechanism:[7]

$$IBr + \text{secondary } e^- + M \rightarrow IBr^- + M$$

$$IBr^- + CO_2 + M \rightarrow IBr(CO_2)^- + M$$

$$IBr(CO_2)^- + CO_2 + M \rightarrow IBr(CO_2)_2^- + M$$

$$IBr(CO_2)_n^- + CO_2 + M \rightarrow IBr(CO_2)_{n+1}^- + M$$

This mechanism shows that cluster formation depends on the presence of neutral CO_2 molecules along with third-body collision partners. As the density of the expansion increases, a shift toward larger cluster formation is favored. The resulting anions formed in the molecular jet drift approximately 15 cm in the source chamber before being repelled perpendicularly into the acceleration flight tube.

2.3 Ion Beam Formation and Time-of-Flight Mass Selection

The molecular anions produced from the expansion are repelled perpendicularly into a time-of-flight mass spectrometer by a pulsed-repeller plate. The repeller plate obtains a

negative voltage pulse generated from a home-built switch and triggered by a TTL pulse, which, in turn, is generated by a Stanford Research Systems Delay Generator with a dc input voltage varied between 400–700 volts. The input voltage is varied to help obtain the best possible signal on the inline detection multichannel plates (MCP) further down the chamber.

The ions are extracted into an acceleration stack consisting of 10 metal annuli separated by 0.43 cm. Each annulus is 7.62 cm in diameter with a 2.54 cm aperture for the ions to pass through. A voltage of 2.3 kV is connected to the last annulus on the acceleration stack and resistively connected to ground with 1 MΩ resisters across the 10 annuli, which creates a field that accelerates the ions to a kinetic energy of 2.8 keV. The acceleration stack marks the beginning of the Wiley-McLaren time-of-flight mass spectrometer.[4] Upon exiting the acceleration stack, the ions encounter a set of horizontal and vertical deflector plates, each with a potential difference between 0–60 V above the float voltage of 2.3 kV. The deflectors are followed by an Einzel lens, which is composed of three elements. Each element is 3.81 cm long with a 2.54 cm aperture for the ions to pass through. The first and third elements are held at the float voltage of 2.3 kV, with the middle element operating in a deceleration mode at a static 800–1000 V above ground.

Upon exiting the Einzel lens, the ions enter a 70 cm long potential-switch drift tube, electrically isolated from the ion options and chamber. When the repeller plate is triggered, the potential of the drift tube is switched from ground to the float voltage using a Directed Energy Inc. PVX-4140 pulse switch. When the anion of interest is in the drift tube, the potential is rapidly switched to ground. The potential switch allows for a defined mass range of ~200 amu to make it through the drift tube without being deflected upon exiting. The entrance and end of the potential switch are fitted with an annulus with a 2.54 cm hole to limit the field penetration into the potential switch and deflect the ions. Upon exiting the drift tube, the ions are steered through a 1.5 degree bend introduced in the flight tube to separate out any neutral particles formed from collisions in the drift tube. After the 1.5 degree bend, a

deflector is introduced to steer the ions down the remaining portion of the flight tube; the neutrals collide with the side of the chamber.

After the 1.5 degree deflector, the ions encounter a mass gate composed of three sets of parallel horizontal plates. The mass gate is arranged in a configuration where the first and third set of plates are held at ground, while one of the middle pair of plates is held at a high potential (600 V) and pulsed down to ground when the anion of interest is between the plates. It is pulsed back to the high potential once the anion of interest has passed. After exiting the mass gate the ion enters a differentially pump chamber containing the photoelectron velocity map-imaging setup, a reflectron (not used), and a horizontal deflector before it impinges on the front face of a microchannel plate detector. The inline MCP detector consists of two impedance-matched plates housed in a chevron configuration (Hamamatsu Corp. F4612-09 and Burle 32733). Electrons emitted from the microchannel plates are collected by an anode plate biased at 200 V above the back face of the MCPs. A diagram of the voltage separator for the MCP's and anode plate is diagrammed in Figure 2.3.

The anode signal is amplified by a Stanford Research Systems (SR 240A) 350 MHz fast preamplifier, increasing the gain of the signal by a factor of 10. This signal is monitored on a 200 MHz oscilloscope (Tektronix 2445B). This signal is monitored as a time-of-flight mass spectrum by recording the anion arrival time in reference to the pulse of the repeller plate.

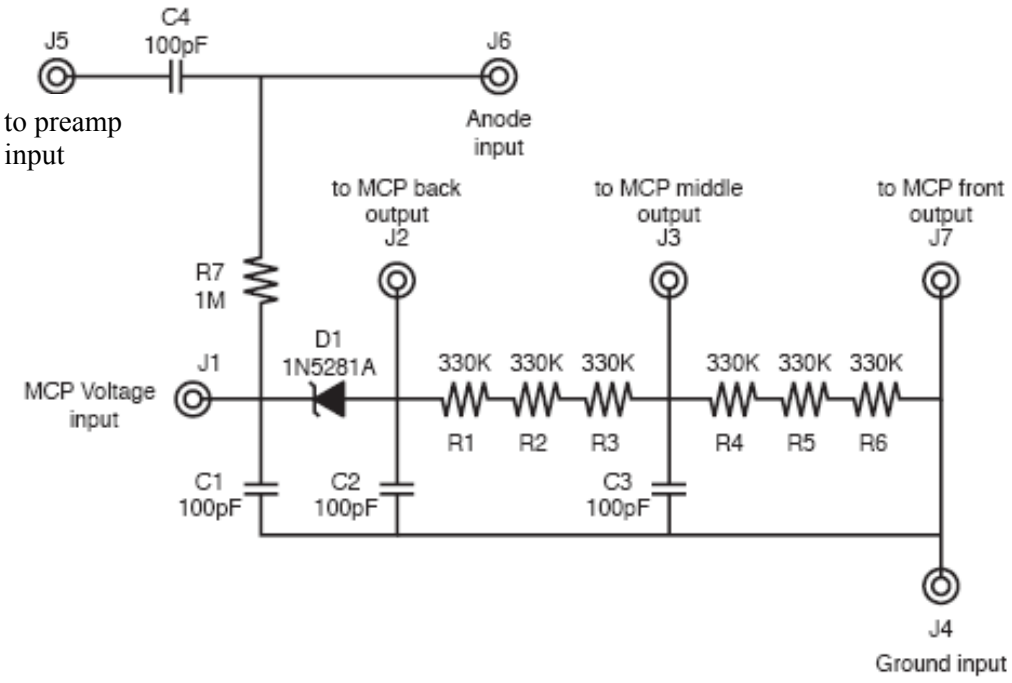

Figure 2.3 Electronic scheme of the MCP-box, acting as a voltage divider to the MCPs, and the input from the collection anode.

2.4 Velocity Map-Imaging Photoelectron Detection

The photoelectron-imaging spectrometer, displayed in Figure 2.4, is based on the velocity map-imaging technique developed by Eppink and Parker.[5] Our spectrometer is a modified version of the spectrometer employed by Sanov and co-workers.[6] The imaging setup is composed of a three-element copper lens, a copper flight tube, a MCP stack housed in a chevron configuration, a P47 phosphor screen (Burle) with a μ-metal cup covering the three copper elements, and 4 rolled sheets of μ-metal, forming a sleeve inside of the copper flight tube. The three copper electrodes are arranged vertically in a stack separated from one another by 2.54 cm.

The first lens consists of a negative repelling voltage, the second element is at ground potential, and the third element is a positive extraction voltage. All lenses are 7.62 cm in diameter, and 0.762 mm thick, with 2.54 cm apertures on the ground and extraction plate allowing the electrons to fly through; the repelling plate has no apertures. The electrodes are contained in a μ-metal (Magnetic Shielding Corp.) enclosure with a 2.54 cm aperture for the entrance and exit laser beam and entrance for the ion beam. A slit 1.25 cm wide and 3.6 cm long on the exit path allows ions to be directed towards the reflectron (not used in these experiments). An aperture 1.25 cm in diameter on the bottom of the enclosure allows for efficient pumping of the imaging region. Typical voltages on the repeller plate range between −15 and −200 V at the time of photodetachment. The middle plate is held at ground potential, and the third plate is held at a positive voltage between 45 and 600 V, helping to extract the electrons into the flight tube. The extraction plate is in physical contact with a 15-cm-long—7-cm-diameter—oxygen-free high-conductivity—copper-field free-flight tube. The flight tube is mounted on an 8” conflate flange.

The inner surface of the flight tube is lined with four layers of a 0.5 mm thick μ-metal sheet rolled to line the flight tube. At the exit of the flight tube is a 40 mm active

diameter-imaging dual-impedance-matched chevron-configured microchannel plate detector and a P47 ($Y_2SiO_5:Ce^{3+}$) type phosphor screen coupled by a fiber optic bundle to a chamber window (Burle Electro-Optics, Inc.). This window is imaged by a 1280 x 1074 pixel CCD camera (LaVision 3Ls, 6.7 μm x 6.7 μm pixel size, Peltier cooled). This camera is interfaced with a desktop PC, which is utilized in data collection.

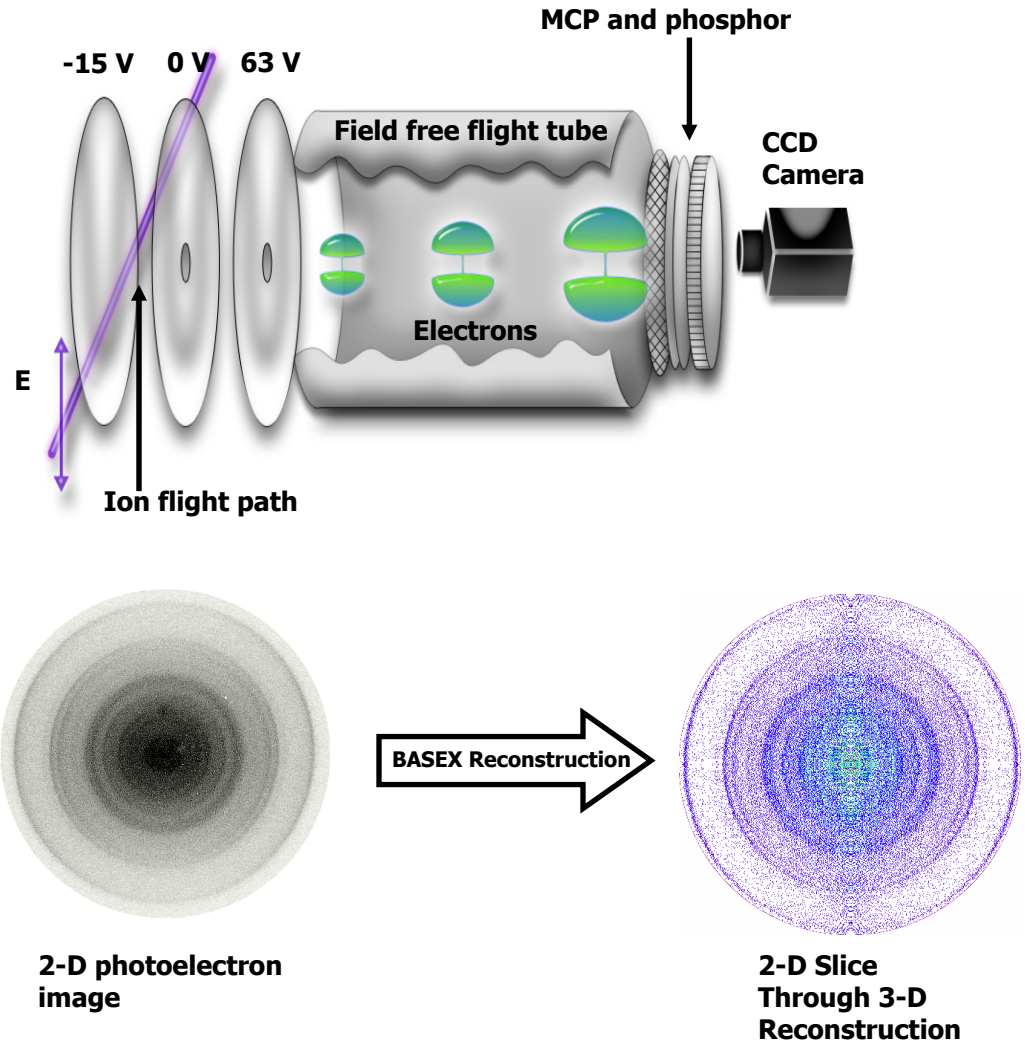

Figure 2.4 Velocity map imaging setup (top of image), with the repeller, ground, and extraction plates, field-free flight tube, and detection system. A typical raw image is displayed on the bottom of the image, with the reconstructed image obtained with the BASEX reconstruction.

Photodetachment of the electron from the molecule occurs approximately half way between the repeller and ground plate in the electron-imaging assembly. The repelling plate is pulsed to a negative voltage by an externally controlled switched-power supply (Directed Energy Inc. PVM-4210) ~ 10 μs prior to the arrival of the laser pulse. The voltage applied to the repeller must be optimized for each laser wavelength used for photodetachment because of minute changes in the position of the laser pulse. These changes in position affect the focusing of the electrodes on the photodetached electrons. The voltages are optimized by monitoring the full width at half maximum of a well-known electronic transition in the photoelectron spectra of an atomic anion. In the studies conducted here, the $^2S \leftarrow {}^1S$ transition in copper was monitored in the cases utilizing copper. In the case of IBr^-, the $^2P_{3/2} \leftarrow {}^1S$ transition in I^- was monitored.

The microchannel plates in the imaging setup are arranged to help eliminate background noise. The front of the imaging detector is held at the flight tube voltage, while the back of the detector is pulsed from 1700 to 2300 V above the frond face by an externally switched high-voltage pulse generator (Directed Energy Inc. PVM-4140). The voltages are externally provided. The switching between 1700 and 2300 V produces a ringing on the front face of the microchannel plate. The ringing causes a transient in the electron lens that leads to the image size changing with the delay introduced in the switching time. To alleviate this image size discrepancy, the back of the microchannel place is switched high 1 μs before the arrival of the photodetachment laser pulse. By this time, the ringing has subsided, allowing the background signals to continue to be reduced. The phosphor screen is held 3000 V above the high voltage of the microchannel plate. The electrons emitted from the MCPs impinge upon the phosphor screen, fluoresceing at 400 nm. Images of the phosphor screen are acquired by a CCD camera, which is interfaced to a PC and operates in a digital event-

counting mode. The CCD is exposed between 50 – 500 ms. At this point an event recorded with a intensity profile greater than our background threshold is interpreted as a photoelectron. A typical data set contains 5000–100,000 images, which are continuously summed together to create the final image. The exposure time for each image is set to record the greatest number of events without stacking events on top of each other. Otherwise, the event counting software would count the two events as a single event, thereby reducing the data collected.

We have a resolution detection limit of approximately 2% of the electron kinetic energy. We determine this limit by measuring the full width at half maximum of the electron's kinetic energy divided by a single electron's kinetic energy (ΔeKE/eKE). For electron kinetic energies below 200 meV, electron-binding energies can be determined with an accuracy of ±0.005 eV or better. To date, the best resolution obtained has been the detection of a Cu ^{2}S peak where the ΔeKE/eKE was measured at 1%. The energy resolution is limited because the ion propagation is perpendicular to electron extraction. Ion propagation introduces a Doppler shift in the ion velocity. This shift in velocity introduces an irregular anisotropy profile in the image, stretching out the image and making it more elliptical as oppose to circular. This problem has been observed when using relatively low mass atoms and low repeller voltages for electron extraction. It can be corrected by utilizing higher mass atoms and molecules and higher repeller voltages for photodetachment.

2.5 Tunable Nanosecond Nd:YAG Laser System

The laser system utilized in our experiments has a fundamental laser radiation of 1064 nm with a variable repetition rate of 0.1–100 Hz and a characteristic pulse duration of 3 ns. The pulse is generated from a Coherent Infinity laser system, described previously.[8] The 1064 nm pulse is created in a diode-pumped Nd:YAG prism in a ring resonator. The initial 1064 nm pulse is amplified in a dual-pass—flash-lamp-pumped Nd:YAG rods. The

amplified 1064 nm laser light has a maximum pulse energy of 600 mJ/pulse. The fundamental laser pulses undergo frequency doubling in an angle-tuned beta barium borate (BBO) crystal to produce 532 nm pulses with 50% efficiency. These 532 nm pulses are mixed with the residual 1064 nm pulses in another angle tuned BBO crystal to produce the third harmonic of the 1064 nm pulse, yielding 355 nm pulses with 50% efficiency. The resulting laser pulses consist of the remaining 1064 and 532 nm pulses plus the newly formed 355 nm laser pulses, which are separated by use of the appropriate mirrors. The 1064 nm and 532 nm pulses are steered into a beam dump, while the 355 nm pulses are either utilized for photodetachment or used to pump an optical parametric oscillator (OPO). The 355 nm pulse produces signal and idler pulses in a BBO crystal by optical parametric generation. Combined signal and idler beams can be scanned between 410 and 2000 nm, with the wavelength tuning accomplished through the changing of the angle of the BBO crystal that produced the beams. Selection of the signal or idler beam is done optically. The typical setup uses a signal beam, which is passed through a second angle-tuned BBO crystal undergoing frequency doubling. At 710 nm, the OPO produces both signal and idler beams; this is the "degeneracy" of the OPO. As the BBO crystal angle is tuned away from the degeneracy, the line width decreases, until it increases dramatically when degeneracy is reached. A more detailed look at the laser system is presented in Appendix A.

2.6 Image Reconstruction

The image recorded with the CCD camera is interfaced to a desktop PC running the DaVis imaging software by LaVision. Because the center of the image is offset in the frame of the camera, the center of the recorded image must be found. This is accomplished by masking a circle over the image until the recorded image is completely masked by the circle. This is all done by eye and has proved to be the most accurate and reliable method of finding the center.[8] After the initial center is found, the pixels surrounding the center are also utilized

as a center until the best fit is found. The image is then imported into the BASEX program, developed by Dribinski and Reisler to allow a reconstruction of the full 3D distribution.[9] A slice through the center of the 3D distribution from the center of the image outward is outputted as a radial integration of the 2D slice. The output represents a pixel distribution that is indicative of electron velocity. In addition to producing a velocity plot of the photoelectron energy spectra, the image contains the angular distribution described by the angular anisotropy (β) parameter.[10]

Calibration of the speed distribution is done in a two step manner. The relationship between the pixels and the electron kinetic energy (eKE) is given by the relationship

$$eKE \propto c * P^2, \tag{2.1}$$

where c is the proportionality constant used for the calibration, and P is the distance in pixels from the center of the image outward. Since the electrons are traveling at a given velocity, the further out from the center of the image they are, the faster their velocity. The relationship between pixels and velocity is

$$P \propto v. \tag{2.2}$$

The proportionality constant between the velocity and eKE are lumped together and found by plotting the electron kinetic energy vs. P^2 for a known atomic transition measured in the photoelectron spectrometer just prior to calibration. A linear function is fitted to the plot, with the slope of the plot being equal to the proportionality constant. Once the constant is found, the plot can be converted from a pixel scale to an electron kinetic energy scale. The scale is then converted to electron-binding energy (eBE) by subtraction of the electron kinetic energy from the photon energy, i.e.,

$$eBE = hv - eKE, \tag{2.3}$$

Plotting the spectra in terms of eBE allows for a direct comparison between several spectra independent of the photodetachment wavelength.

2.7 Data Analysis

The analysis of the photoelectron spectra is complemented with theoretical studies, which aid in the spectral assignments. More often than not, features that were not expected are present in the photoelectron spectra; the theoretical calculations aid in the determination of these features. The primary method utilized in the study of these systems calculates the ground state geometry and vibrational frequency of the anion, neutral, and any excited state present using the Gaussian suite of programs.[11] Most information is obtained through energy calculations, that aid in estimating electron-binding energies.

To aid in the determination of the spectral assignments, the Gaussian output files are converted for input into the FCFGaus03 program by running a FCF Gaussian job. The FCF Gaussian job is used to extract the geometries and vibrational frequencies from the Gaussian output file, where the new FCF output files are imported into the FCFGaus03 program. FCFGaus03 uses the normal coordinates and frequencies to calculate the Dushinsky rotation matrix J and the displacement vector K. The Dushinsky rotation matrix and displacement vector are transformed into the Sharp and Rosenstock arrays A, B, C, D, and E. These new outputs are matrices that are used to calculate a spectral simulation in the PESCAL program.[12]

The PESCAL program is utilized to calculate a simulated spectrum from the initial geometry of the anion and neutral species. The parameters of the anion and neutral geometries, and frequencies can by manually inputted or they can be imported from the Dushinsky rotation matrix previously calculated using the FCFGaus03 program. Several of the parameters such as anion temperature, the intensity of the origin, and eKE of the origin are adjustable in the PESCAL program. These adjustments are used to create a representative spectrum of the collected photoelectron spectrum. The software also allows for the electron kinetic energy vs. intensity data to be imported for direct comparison to the simulated spectra.

For further optimization of the simulated spectra, a statistical weighting on a Chi-square limit can be run against the simulated spectra and imported data to produce a cohesive match between the data and simulation. Once a match between the two spectra is accomplished, the simulation is exported in two formats, a stick spectrum where the intensity and positions of the transitions occur, and a convolution of the data. A comparison of the simulated spectra to the photoelectron spectra allows for assignments to be made, that are independent of the individual states present in the spectra; thus each electronic state can be independently simulated and compared.

References for Chapter II

1 M. E. Nadal, P. D. Kleiber, and W. C. Lineberger, The Journal of Chemical Physics **105** (2), 504 (1996).

2 G. J. Rathbone, T. Sanford, D. Andrews, and W. C. Lineberger, Chemical Physics Letters **401** (4-6), 570 (2005).

3 A. Sanov, T. Sanford, S. Nandi, and W. C. Lineberger, The Journal of Chemical Physics **111** (2), 664 (1999).

4 W. C. Wiley and I. H. McLaren, Review of Scientific Instruments **26** (12), 1150 (1955).

5 A. T. J. B. Eppink and D. H. Parker, Review of Scientific Instruments **68** (9), 3477 (1997).

6 E. Surber, R. Mabbs, and A. Sanov, Journal of Physical Chemistry A **107** (40), 8215 (2003).

7 T. Sanford, S. Y. Han, M. A. Thompson, R. Parson, and W. C. Lineberger, Journal of Chemical Physics **122** (5), 054307 (2005).

8 D. H. Andrews, Ph.D. Thesis, University of Colorado, 2006.

9 V. Dribinski, A. Ossadtchi, V. A. Mandelshtam, and H. Reisler, Review of Scientific Instruments **73** (7), 2634 (2002).

10 R. N. Zare, *Angular Momentum*. (Wiley, New York, 1988).

11 M. J. Frisch, G. W. Trucks, H. B. Schlegel, G. E. Scuseria, M. A. Robb, J. R. Cheeseman, J. A. Montgomery, Jr. , T. Vreven, K. N. Kudin, J. C. Burant, J. M. Millam, S. S. Iyengar, J. Tomasi, V. Barone, B. Mennucci, M. Cossi, G. Scalmani, N. Rega, G. A. Petersson, H. Nakatsuji, M. Hada, M. Ehara, K. Toyota, R. Fukuda, J. Hasegama, M. Ishida, T. Nakajima, Y. Honda, O. Kitao, H. Nakai, M. Klene, X. Li, J. E. Knox, H. P. Hratchian, J. B. Cross, C. Adamo, J. Jaramillo, R. Gomperts, R. E. Stratmann, O. Yazyev, A. J. Austin, R. Cammi, C. Pomelli, J. W. Ochterski, P. Y. Ayala, K. Morokuma, G. A. Voth, P. Salvador, J. J. Dannenberg, V. G. Zakrzewski, S. Dapprich, A. D. Daniels, M. C. Strain, O. Farkas, D. K. Malick, A. D. Rabuck, K. Raghavachari, J. B. Foresman, J. V. Ortiz, Q. Cui, A. G. Baboul, S. Clifford, J. Cioslowski, B. B. Stefanov, G. Liu, A. Liashenko, P. Piskorz, I. Komaromi, R. L. Martin, D. J. Fox, T. Keith, M. A. Al-Laham, C. Y. Peng, A. Nanayakkara, M. Challacombe, P. M. W. Gill, B. Johnson, W. Chen, M. W. Wong, C. Gonzalez, and J. A. Pople, Gaussian 03, Revision B.05 (Gaussian, Inc., Pittsburgh, PA, 2003).

12 K. M. Ervin, J. Ho, and W. C. Lineberger, Journal of Chemical Physics **91** (10), 5974 (1989).

Photoelectron Velocity-Map Imaging Spectroscopy of IBr^-

3.1 Introduction

Much of the chemistry that governs chemical reactions takes place in solution. A solvent has many important effects on reactivity, including acting as a medium for energy exchange. In effect, the solvent alters the potential energy surface of the reacting molecules by raising or lowering the barriers to the reaction. Studying the effects of solvent molecules on chemical reactions at the molecular level in solution provides many challenges, including the lack of a well-defined solvent environment. However, molecular ionic clusters can offer a picture of a solvent molecule in a well-defined microenvironment that provides characteristics of the condensed phase moiety. Because we can vary the cluster size, the study of these gas phase clusters enhances our ability to investigate properties that bridge the gas-phase to condensed phase in a controlled environment.

Much work using photoelectron spectroscopy has focused on the effects of CO_2 solvation in $X_2^-(CO_2)_n$ clusters, where n is the cluster size and X is one of the halogens (F, Cl, Br, or I).[1-3] This work led, in turn, to investigations of mixed dihalide anions (i.e., ICl^-, IBr^-).[4-8] IBr^- and other halogen molecules are useful in spectroscopic studies, because they absorb visible and ultraviolet light quite easily. Because these molecules exhibit a large number of low-lying excited states due to spin-orbit splitting, interesting studies have emerged, especially on IBr.[9-15] Our ability to study these systems with negative ion photoelectron spectroscopy allows us to measure potential energy curves and investigate molecular photodissociation dynamics. Previous experiments in the Lineberger group[16-19] investigated the photodissociation dynamics of the negative ion cluster $IBr^-(CO_2)_n$ (n=0–14). In these experiments, a long-lived excited state was found for the $IBr^-(CO_2)_8$ cluster. Its

recombination time was two orders of magnitude longer than previously predicted by recombination studies on $I_2^-(CO_2)_8$. This very slow recombination was hypothesized to be caused by the trapping of the cluster anion in a shallow well formed on the otherwise repulsive A' state potential-energy surface as solvent molecules were added. An investigation was subsequently proposed to characterize the solvent-induced well through a pump-probe photoelectron-imaging experiment.[2,4,20,21] Before this experiment could be done, however, a single photon photoelectron-imaging experiment had to be conducted on the system to map the binding energies of the various electronic states of the solvated $IBr^-(CO_2)_n$ molecule. Because the binding energy of a specific electronic state at a given cluster size will not change, identification of the binding energies for these states prior to the pump-probe studies, will allow for identification of the final electronic states in future studies. A schematic is presented in Figure 3.1 outlining the electronic states to be accessed in these studies, the ground $\mathbf{X}\ ^1\Sigma$ state, and the two excited $\mathbf{A}\ ^3\Pi_1$ and $\mathbf{A}\ ^3\Pi_2$ states.

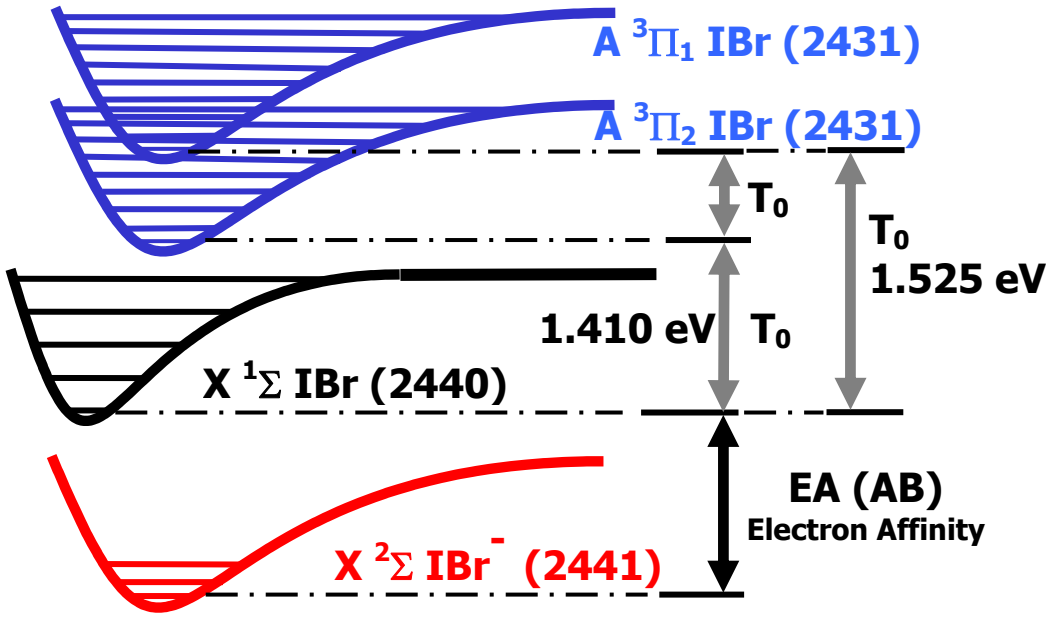

Figure 3.1 Schematic diagramming of the potential energy curve of possible photodetachment states arising from IBr^-. Electronic states are labeled according to Hund's case (c) notation. See text for details.

Identification of the electronic states in the photoelectron spectra of IBr is aided by using the previously measured photoelectron spectra of I_2^- by Neumark *et al*.[22] Changing the molecule from a homo-diatomic molecule (I_2), to a hetero-diatomic molecule (IBr), should yield a photoelectron spectra that contains the same type of electronic state features. Adapting the features of the I_2^- spectra to IBr^- should result in a shift in the electronic states toward higher-binding energies, even with a reduction in symmetry. This shift in binding energy is caused by the change in electron affinity between I and Br at 3.059 and 3.363 eV, respectively.[23,24]

The single photon studies of solvated IBr^- clusters will be geared toward accurately measuring the binding energy of the first excited **A** $^3\Pi_1$ and $^3\Pi_2$ states of IBr using a photodetachment wavelength of 300 nm. A 300 nm photon has an energy of 4.132 eV, which is enough energy to access the excited **A** states in I_2. Even with a shift toward higher-binding energies in IBr, the photon energy used will allow the ground **X** $^1\Sigma$ and excited **A** $^3\Pi_1$ and $^3\Pi_2$ states of IBr to be accessible. These relevant electronic states are presented in a schematic in Figure 3.1. The electronic states are labeled according to the electron configuration from which they arise, in conjunction with Hund's case (c) notation. The $\ldots(\sigma_g)^m(\pi_u)^p(\pi_g^*)^q(\sigma_u^*)^n$ notation for the electron configuration is abbreviated as mpqn.[25]

In this chapter, we report the use of negative-ion photoelectron spectroscopy to determine a much improved value for the electron affinity of IBr and the bond dissociation energy of the anion. The rest of this chapter has six sections: (3.2) a brief experimental section, (3.3) an overview of the results, (3.4) a detailed analysis of the IBr ground state, (3.5) and (3.6) analyses of the excited **A** $^3\Pi_2$ and **A** $^3\Pi_1$ states, respectively, and (3.7) conclusion.

3.2 Experiment

IBr anions are formed by secondary electron attachment, as described in Chapter 2. Photoelectron spectroscopy of IBr^- is carried out with a velocity map-imaging photoelectron spectrometer that has also been described previously.[26] IBr^- clusters are formed in a pulsed supersonic expansion containing IBr and CO_2. The IBr anions are produced in this expansion by low-energy electron attachment to IBr by the following mechanism:[18]

$$IBr + \text{secondary } e^- + M \rightarrow IBr^- + M.$$

A sample holder was constructed to house IBr (Aldrich, 224847, Iodine monobromide) with the greatest amount of surface area of IBr exposed. CO_2 flows over the IBr at a pressure of 0–30 psi, while the IBr sample is gently heated to 30 ºC. This configuration relies on the vapor pressure of IBr to seed the carrier gas. The line connected from the IBr sample holder to the General Valve is made of a polytetrafluoroethylene (PTFE), "Teflon," tube. The amount of metal coming into contact with the IBr sample has been minimized, because IBr reacts with the metal, causing corrosion to occur and producing undesirable by-products. The CO_2 gas mixture is passed through a General Valve (series 9) with an 800 μm orifice expanding into our source chamber where it is crossed with an electron gun, producing the negative ions. The anions are then repelled perpendicularly into a Wiley-McLaren[27] type time-of-flight mass spectrometer. Typical anion signals of 800 mV are detected from the microchannel plates (MCP) combined with a preamplifier. A typical time-of-flight mass spectrum is shown in Figure 3.2.

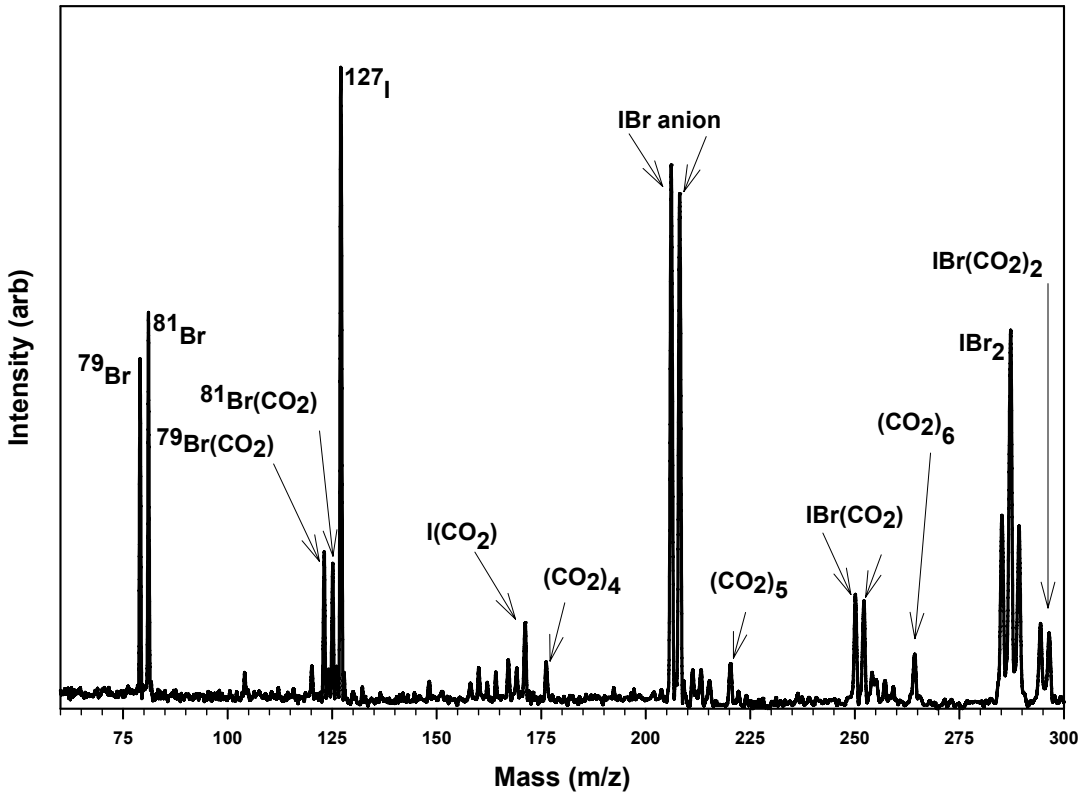

Figure 3.2 Time-of-flight mass spectrum obtained from a pulsed source, peaks are labeled accordingly. The sample contains IBr and CO_2; expansion conditions were chosen to favor the formation of the bare IBr^-.

Photoelectron spectra are recorded at an ultraviolet photodetachment wavelength of 300 nm using the doubled light of the optical parametric oscillator (OPO) pumped by the Infinity laser system. Two photoelectron images of IBr^- were recorded at 300 nm, with each image focusing on a different part of the spectra. In each image, the optics are optimized to focus and maximize the size of the photoelectron image. This optimization is done to collect the greatest amount of photodetached electrons from IBr^-. It is done using a reference ion, I^-. The well-known electron affinity of the I atom observed in the photoelectron spectrum of the $I^-\ ^2P_{3/2} \leftarrow\ ^1S$ transition is used to focus the photoelectron-imaging optics and calibrate the energy scale.[24] A 300 nm photoelectron spectrum of I^- is presented in Figure 3.3. For electron kinetic energies below 200 meV, electron-binding energies can be determined with an accuracy of ±0.005 eV or better.[26] The ground ($\mathbf{X}\ ^1\Sigma$) and excited ($\mathbf{A}\ ^3\Pi_{1,2}$) states of IBr are collected in the first image (Figure 3.8). The photoelectron-imaging optics were then optimized to magnify the excited ($\mathbf{A}\ ^3\Pi_{1,2}$) states in the second photoelectron image (Figure 3.9). An image is magnified by decreasing the repeller and extraction voltages. This reduces the potential felt on the photodetached electrons, allowing them to expand more by the time they reach the detector. All images are recorded in event-counting mode with 250 ms charge-coupled device (CCD) exposures at very moderate laser pulse energies of less than 100 μJ at 300 nm.

The pulse energy is chosen to reduce the background signal as much as possible while still allowing the ground and excited triplet states to be accessible with the desired photon energy.

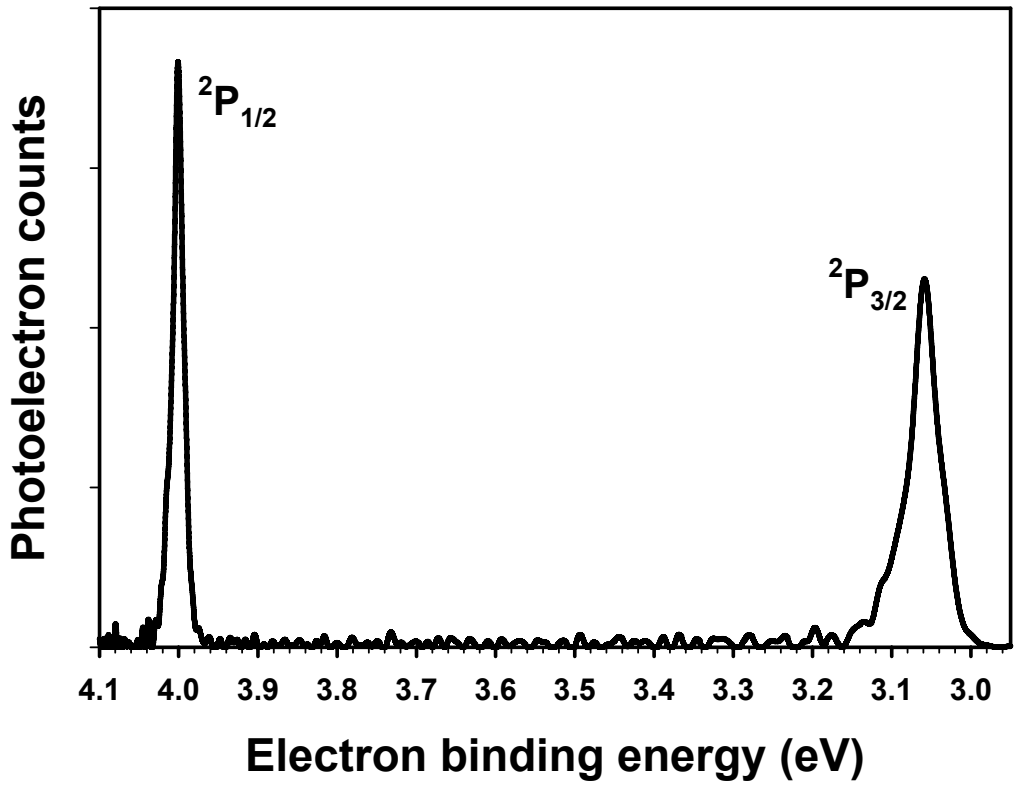

Figure 3.3 Photoelectron spectra of I^- recorded at 300 nm. The two lowest states of I neutral are observed; both states are utilized in the calibration of the photoelectron spectra of IBr^- and are labeled accordingly. The $^2P_{3/2}$ peak occurs at a electron-binding energy of 3.059 eV, with the $^2P_{1/2}$ peak occurring at an electron-binding energy of 4.001 eV.[24,28]

3.3 Results

A photoelectron spectrum of IBr^- was recorded with a photodetachment wavelength of 300 nm and compared to that of I_2^-. Identification of the electronic states in IBr were aided by using the previously measured photoelectron spectra of I_2^- of Neumark *et al*.[22] As can be seen in the photoelectron spectra for I_2^- (Figure 3.4), seven electronic states are observed. With the electronic states of IBr occuring at higher-binding energies than I_2 the trend in the electronic states can easily be followed. The I_2^- photoelectron spectrum lacks a vibrational progression in the excited states. In contrast, a vibrational progression is observed for both the ground and excited states in the photoelectron spectra for IBr.

The photoelectron spectra of IBr^- is shown in Figure 3.5. Three electronic states are observed. A 300 nm photon has an energy of 4.132 eV, which is slightly higher than the **A** states observed in the I_2^- photoelectron spectra, giving an indication of the electronic states that will be observed in the IBr spectra. The IBr spectra were generated by integrating the photoelectron image (Figure 3.6) from the center out, over all angles.

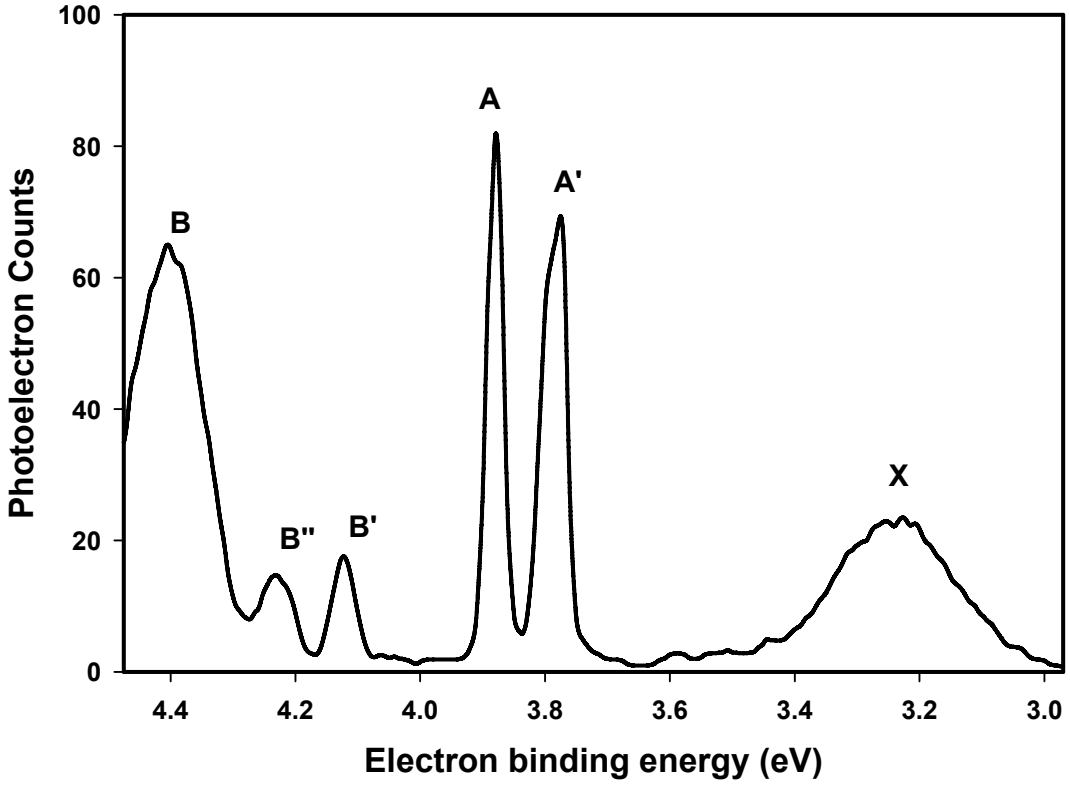

Figure 3.4 Photoelectron image of I_2^- recorded at 266 nm. Three of the six states are observed in our spectra, allowing for a comparison of binding energies.[22]

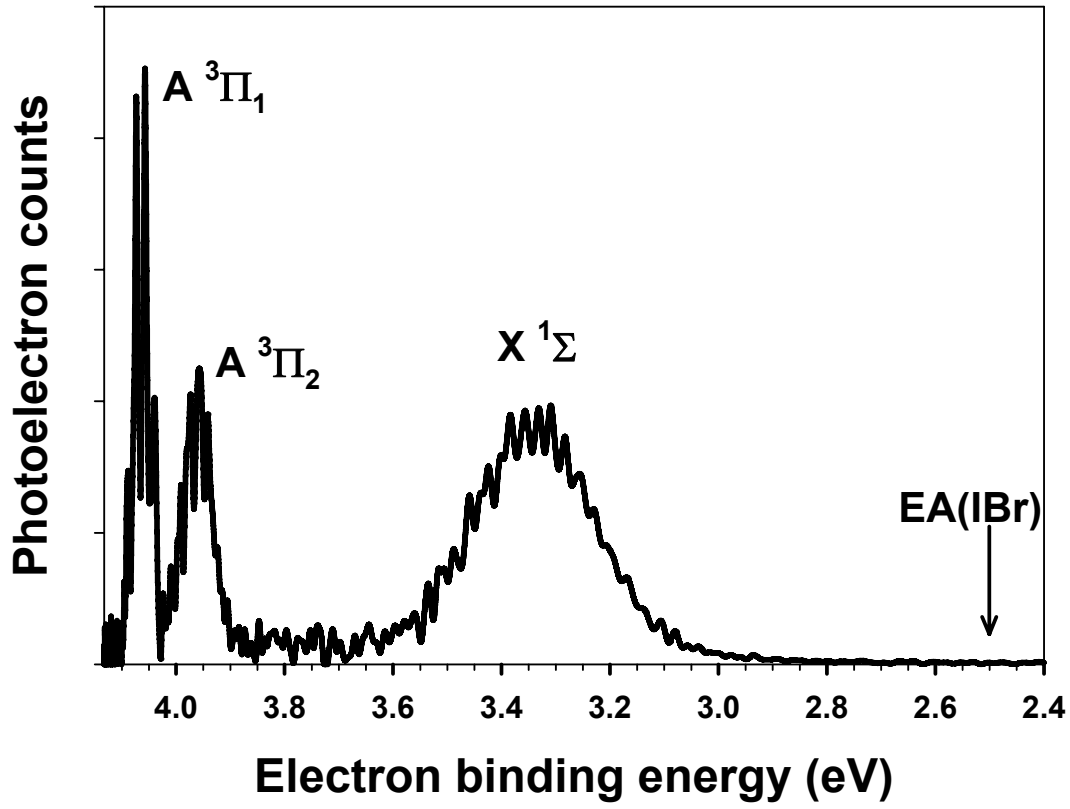

Figure 3.5 Photoelectron spectra of IBr^- recorded at 300 nm. Data are obtained from integration of the BASEX-reconstructed image in Figure 3.6.

The raw photoelectron images and BASEX[29]-reconstructed images of IBr^- are recorded at 300 nm and presented in Figures 3.6 and 3.7. The images in Figure 3.6 contain the raw and reconstructed image of IBr^- and show the ground **X** $^1\Sigma$ and first-excited triplet **A** $^3\Pi_1$ and $^3\Pi_2$ states. The raw and reconstructed images display an energy span of 2.66 eV from one side of the image to the other. The rings found in the image correspond to the three observed electronic states of IBr. A vibrational progression is observed in the image for each of the three electronic states. Very little detachment occurs at lower electron velocities (center of image), indicating that we are not on the threshold of an electronic state. A distinct ring occurring at higher electron velocities (outer edge of image) corresponds to the ground state of the neutral.

The second set of raw and reconstructed images (Figure 3.7) magnifies the first-excited **A** $^3\Pi_1$ and $^3\Pi_2$ states of IBr. The images display an energy span of 0.42 eV from one side of the image to the other A vibrational progression is clearly resolved for the two electronic states, with each state having a different vibrational spacing, indicating different electronic states and subsequently different equilibrium bond lengths for each state. These vibrational progressions are used to measure the bond length of the anion. The measurement of the binding energy of these excited **A** states will be used extensively when a pump-probe experiment is carried out in these systems, as it will be the only accessible state from the anion electronic configuration.

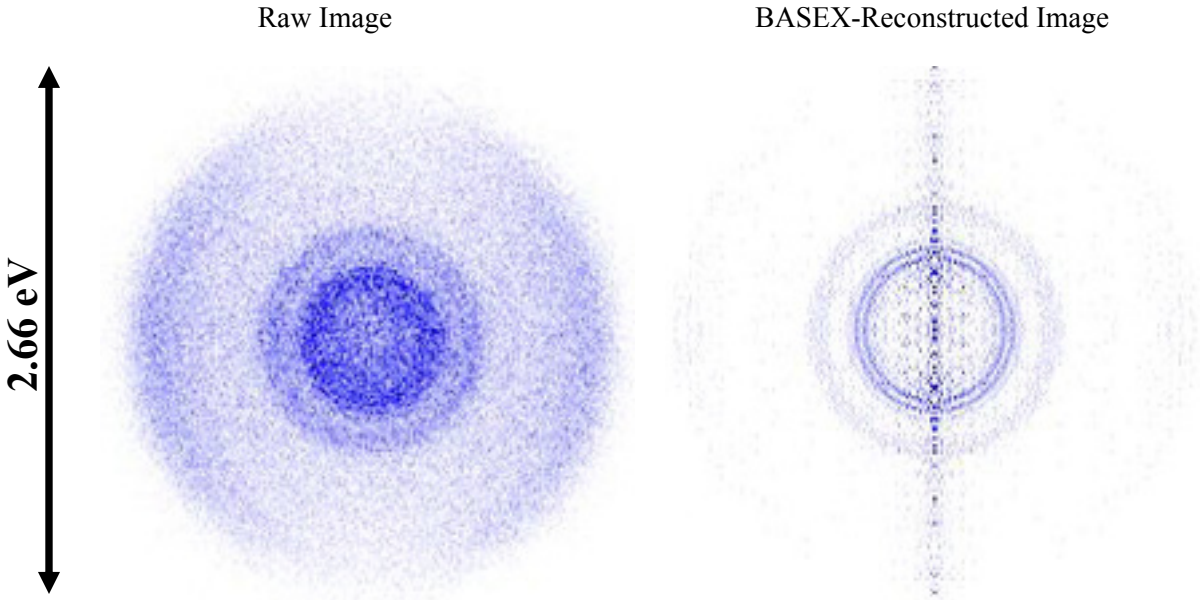

Figure 3.6 (Left) Raw IBr^- photoelectron image showing all photoelectron energies from 0 to 1.33 eV. This image was recorded at a wavelength of 300 nm. (Right) BASEX-reconstructed image. Three electronic states are present, and the image has an energy span of 2.66 eV.

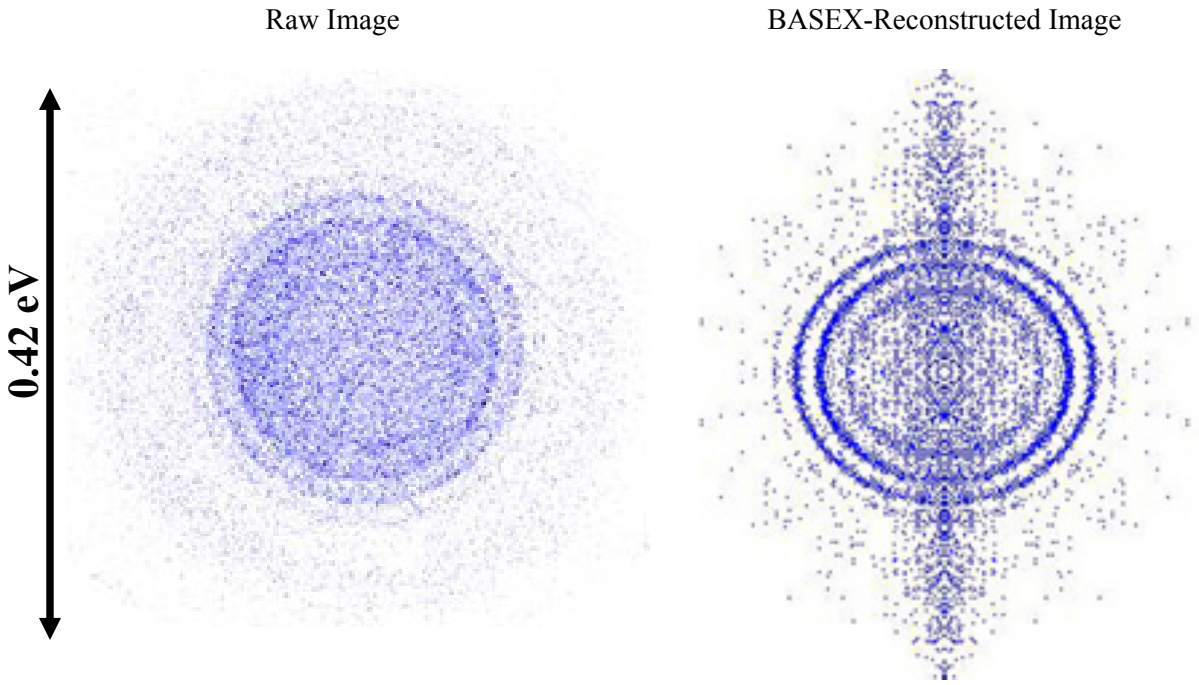

Figure 3.7 (Left) Raw IBr^- photoelectron image showing all photoelectron energies from 0 to 0.21 eV. The image was recorded at a wavelength of 300 nm. Electron optics were adjusted to magnify the excited $^3\Pi_{1,2}$ states. (Right) BASEX-reconstructed image. The energy scale of the image spans 0.42 eV.

The anion starts out in a 2441 configuration. When photodetachment occurs, an electron from the σ_u* orbital is removed, resulting in IBr in the ground **X** state, a 2440 configuration. If photodetachment of an electron occurs from the π_g* orbital, this results in the neutral 2431 configuration, producing the first excited **A** $^3\Pi_1$ and $^3\Pi_2$ states observed in the spectra. Accurate energy levels of the anion and neutral have been previously calculated.[18,30]

The potential energy curves for IBr were calculated by Jungwirth (Figure 3.8),[30] and the anion potential energy curves were calculated by Thompson and Parson (Figure 3.9).[18] These previous calculations not only gave a starting point for determining what electronic states would be accessible, but also were used in the photoelectron simulations using the PESCAL program developed by Ervin.[31] The PESCAL program calculates the Franck-Condon overlap between the anion and neutral structures of the molecule of interest, allowing a photoelectron spectrum to be calculated. The calculated photoelectron spectrum is used in assigning the spectral features and spectroscopic constants. In the calculated IBr photoelectron spectra, the neutral configurations are held constant to previously measured spectroscopic constants[14,32,33] while the anion parameters are adjusted. Holding the neutral structure constant allows us to determine an accurate change in the bond length from the anion to neutral.

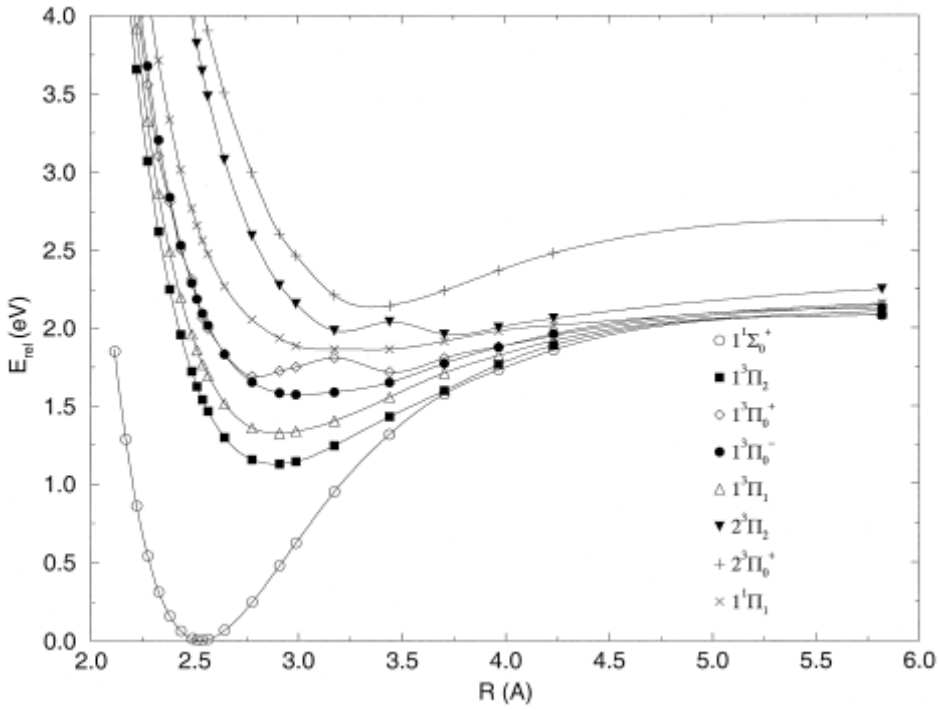

Figure 3.8 Calculated potential energy curves of the ground and seven lowest-excited potentials of IBr including the spin-orbit interactions. Energy is relative to the ground state minimum. Symbols represent the calculated points.[30]

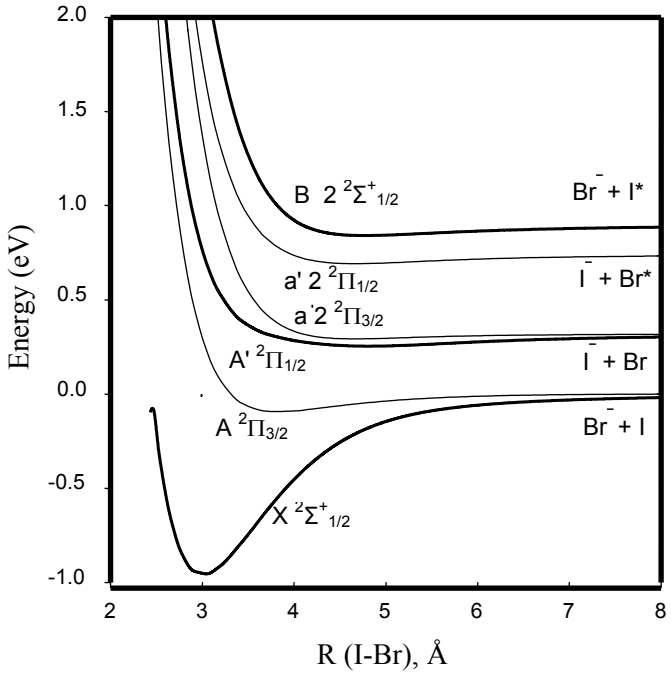

Figure 3.9 Potential energy curves of the ground and five lowest-excited potentials of the IBr^- molecule.[18]

3.4 Ground Electronic $X\,^1\Sigma$ State of IBr

The photoelectron spectrum presented in Figure 3.5 was obtained by integrating the reconstructed (right hand column) image in Figure 3.6. Present in this image are both the ground and first-excited triplet states of IBr. The individual electronic states are labeled accordingly in the photoelectron spectra. The ground electronic state of the neutral is observed in the raw and reconstructed image in Figure 3.6 as the outermost ring of the image. A vibrational progression is observed in the reconstructed image as a series of less intense rings radiating towards the center of the image originating from the outermost ring. Measurement of the binding energy of the ground state only yields a vertical detachment energy of ~3.3 eV. The restriction for measuring a vertical detachment energy is due to a geometry change between the anion and neutral state that is too great to allow for overlap of the electronic states, an inherent problem in photoelectron spectroscopy.

The technique of photoelectron spectroscopy limits our ability to measure the adiabatic electron affinity in certain systems where the Franck-Condon overlap between the anion and neutral state geometries is nonexistent. This poor Franck-Condon overlap is due to the excessive bond-length change between the anion and neutral. The equilibrium bond length of the neutral has been previously measured at 2.468 Å.[34]

The change in bond length results from the photodetachment of an electron from the antibonding σ_u* orbital. Photodetachment of an electron from an antibonding orbital results in greater bonding character, yielding a shorter bond. Because of the shifted potential energy curve of the neutral to a shorter equilibrium bond length, the Franck-Condon overlap only becomes significant at higher vibrational levels. This overlap is observed at higher-binding energies relative to the origin in the photoelectron spectra. For instance, a vibrational progression is observed in the spectrum with a spacing of 201(80) cm^{-1}. Previous

measurements placed the vibration spacing at 267.01 cm^{-1}.[14] This discrepancy is caused by accessing such a high vibrational level in the ground state and by our imaging method where the ground state is on the edge of the detector. Obtaining meaningful information on the ground state isn't favorable, even if a proper wavelength (~340 nm) is chosen to access the ground state and focused properly onto the imaging detector. This difficulty stems from the anharmonicity of the ground state and the high vibrational level that is accessed between the anion and neutral states. Even so, to extract additional information from the ground state, we must use the excited states.

Using the excited triplet **A** states observed in the spectra, useful thermochemical information from the ground state can be extracted. We use these two features to determine the adiabatic electron affinity, (as opposed to using the generalized vertical detachment energy) and calculate the bond dissociation energy of the anion. Both values are reported in the following sections.

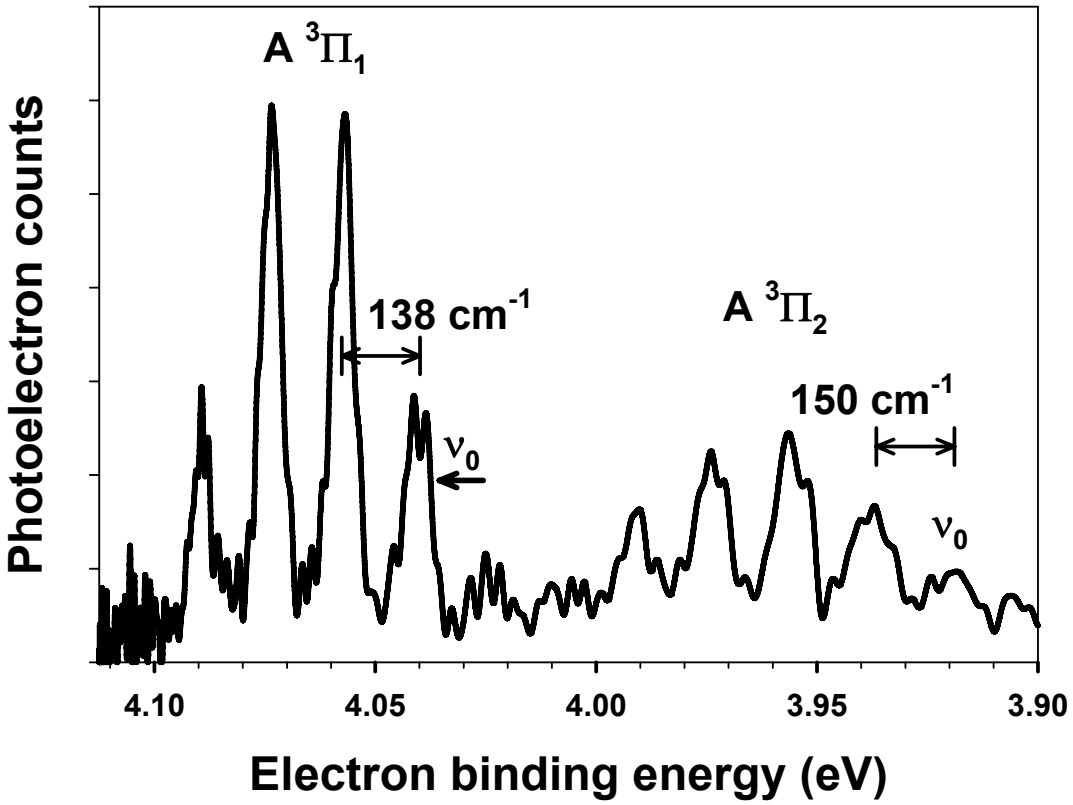

Figure 3.10 High-binding energy portion of the 300 nm photoelectron spectrum of IBr^-, showing magnification of the two excited $^3\Pi_{1,2}$ states. Data are obtained from integration of the BASEX-reconstructed image of Figure 3.7.

3.5 First Excited A $^3\Pi_2$ State of IBr

The IBr molecule has been studied by many authors since the 1920s, but there were no reports of the measurement of the first excited $^3\Pi_2$ state of IBr until the 1990s. The **A** $^3\Pi_2$ state is elusive in conventional optical spectroscopy because of the $\Delta J=0\pm1$ selection rule. Yet it is easily accessible using negative ion photoelectron spectroscopy. The first reported spectra of the $^3\Pi_2$ state came from Tellinghuisen in 1992.[15,33,35] He used state-selective spectroscopy to measure the D' $\rightarrow$ A' transition and determined the spectroscopic constants that will be compared to our reported values.

The most direct measurements obtained in our photoelectron spectra of the **A** $^3\Pi_2$ state is of the binding energy and the vibrational and electronic-state splittings. The binding energy of the **A** $^3\Pi_2$ state origin (Figure 3.10) appears at 3.912(5) eV between the **A** $^3\Pi_2 \leftarrow$ **X** $^2\Sigma$ electronic states. A splitting energy of 1.401 eV between the **A** $^3\Pi_2 \leftarrow$ **X** $^1\Sigma$ transition was previously reported by Tellinghuisen.[33] This splitting allows the splitting energy between the **A** $^3\Pi_2$ and $^3\Pi_1$ states of 124 meV to be calculated.[14,33]

Six distinguishable vibrations with a peak spacing of 150(5) cm^{-1} are observed in the spectra. This compares well with Tellinghuisen's previous measurement of 147.631(9) cm^{-1}.[33] Using the vibrational spacing in the spectra, a bond length change from the anion to the neutral-excited state can be determined. Using a Franck-Condon analysis, the neutral parameters were held constant to known literature values of r_e(**A** $^3\Pi_2$)= 2.842 Å and ω_e=147.631.[33] The anion parameters were adjusted until the vibrational progression in the spectra had a coherent fit. This fit was then repeated using the **A** $^3\Pi_1$ state parameters to confirm these results. The spectra were found to have a best fit with an equilibrium bond length for the anion of 3.025(.01) Å and ω_e of 115(20) cm^{-1}. Simulated spectra containing the

Franck-Condon overlap of the excited **A** $^3\Pi_1$ and $^3\Pi_2$ states of IBr are shown in Figure 3.11. The data from the photoelectron spectra is presented as a black trace, the simulation of the **A** $^3\Pi_1$ state is presented as a red trace, and the **A** $^3\Pi_2$ state is presented as a blue trace. The simulation was run with an anion temperature of 100 K. Hot bands are observed in the spectra, giving rise to the feature below the origin of the peak. A collection of reported values appears in Table 3.1.

Table 3.1 Measured values for the IBr anion, neutral, and excited states.

	$T_{0\text{-}0}$ (eV)		$\omega_{1\text{-}0}$ (cm^{-1})		r_e (Å)	
State	Results	Literature	Results	Literature	Results	Literature
A $^3\Pi_1$	-	1.525[14]	138(5)	135.2[14]	-	2.8583[36]
A $^3\Pi_2$	-	1.410[33]	150(5)	147.631[33]	-	2.8417[33]
X $^1\Sigma$	0	0	201(80)	268.68[14]	-	2.468[34]
X$^-$ $^2\Sigma$	-2.51(1)	-2.55[37,38]	115(20)	136[18]	3.025(.01)	2.9[37]

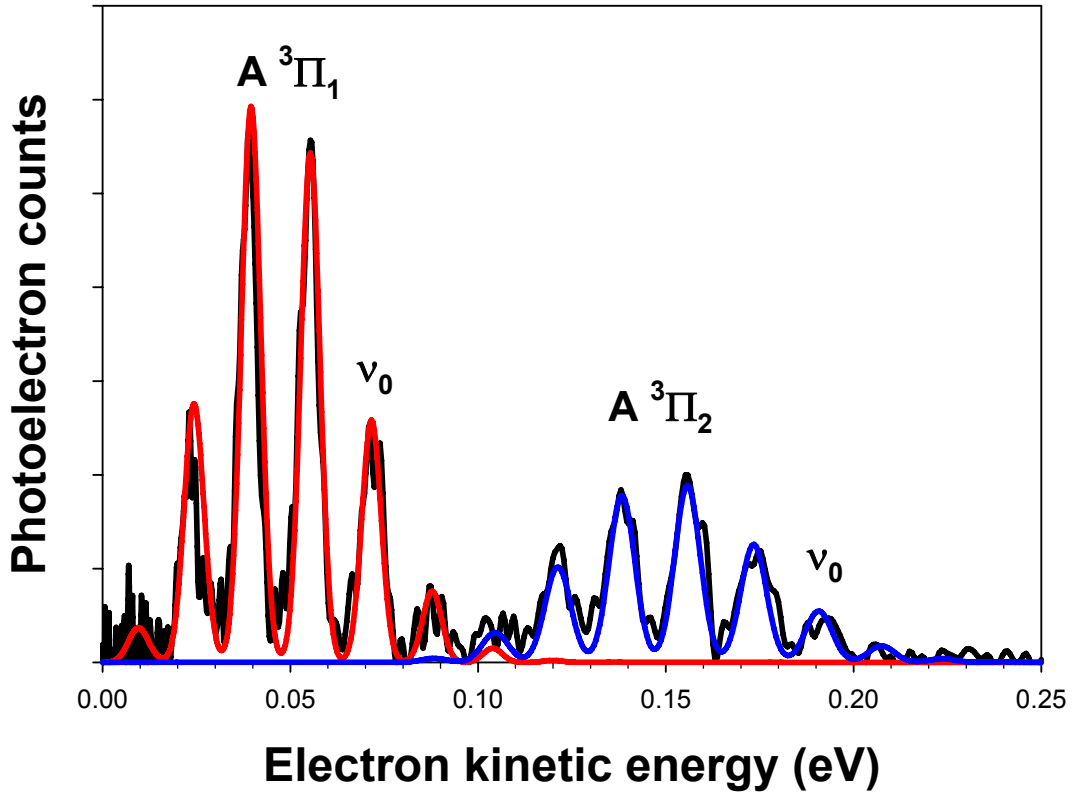

Figure 3.11 Simulated photoelectron spectra of the excited triplet **A** states of the IBr. The red spectrum represents the continuous simulation for the $^3\Pi_1$ state, with the blue lines representing the continuous simulation for the $^3\Pi_2$ state. The simulation was performed with an anion temperature of 100 K and an anion bond length of 3.025(.01) Å.

3.6 First Excited A $^3\Pi_1$ State of IBr

Of the three prominent features in our spectra, the first-excited **A** $^3\Pi_1$ state contains the most accurate measurements in our spectra. The **A** $^3\Pi_1$ state has been previously studied by several groups for many years now.[14,15,32] This state appears in our spectra with an electron binding energy of 4.041(5) eV that corresponds to an electron kinetic energy of 72 meV. Using our measured electron kinetic energy and the measurement by Suzuki[14] of the separation between the **A** $^3\Pi_1 \leftarrow$ **X** $^1\Sigma$ states, of 1.525 eV, we are able to provide a more accurate electron affinity than from the $^3\Pi_2$ state. This measurement allows for an updated value of the electron affinity of IBr of 2.51(1) eV. Previous measurements using chemi-ionization of heteronuclear halogen collisions previously placed the electron affinity at 2.55 eV.[37,38] Our measurement is internally consistent between the two excited triplet states. A vibrational progression with a spacing of 138(5) cm^{-1} is present in our photoelectron spectra, which compares well to Suzuki's previous measurement of 135.2 cm^{-1}.[14] A reported equilibrium bond length of 2.8583 Å[36] for the $^3\Pi_1$ state allows us to confirm the anion bond length using the previous measurement from the $^3\Pi_2$ state. The spectroscopic information obtained from these excited triplet states is used in determining thermochemical properties of the anion.

Measurement of the electron affinity allows for thermochemical properties to be calculated and compared to previous measurements. The bond dissociation energy (D_0) for IBr^- can be calculated by using the equation

$$D_0(IBr^-) = EA(IBr) + D_0(IBr) - EA(Br). \qquad (3.1)$$

Our measured electron affinity for IBr^- is 2.51(1) eV. The best determined measurement of the bond dissociation energy (D_0) of IBr is 1.8184(2) eV,[8] and the electron affinity of Br is 3.363583(4) eV.[23] These measured values place the bond dissociation energy of the anion at

0.97(1) eV. This measurement differs by 136 meV from a previous measurement of 1.10(4) eV by the Lineberger group obtained with a crude photofragment translation energy release method.[18] It compares well to a previous calculation of 0.963 eV.[18] We assign the discrepancy between bond dissociation energies to the technique previously used to measure the anion bond dissociation energy.

Upon dissociation of the neutral I–Br bond, the products are the same when starting from the ground (**X**) electronic or excited (**A**) triplet states. All yield iodine and bromine in their ground electronic state ($^2P_{3/2}$).[6,30] In the case of the anion when the I–Br bond dissociates, the Br atom will contain the extra electron (^1S). This occurs because bromine has a higher electron affinity than iodine.

3.7 Conclusion

Using a negative-ion photoelectron spectrometer, we recorded a set of photoelectron spectra of IBr^- and measured vibrational frequencies and splitting energies of three electronic states. Using the information collected from the photoelectron spectra, we measured an updated electron affinity of 2.51(1) eV by using the measured-splitting energy between the anion and excited triplet states and the known splitting energy between the excited triplet states and the neutral ground state. This new electron affinity measurement allowed us to measure a bond dissociation energy of the anion of 0.97(1) eV. This value compares well to the calculated value of 0.963 eV and updates the previous measurement of 1.10(4) eV.

The two photoelectron spectra shown in Figures 3.5 and 3.10 were recorded at separate times but correspond well to each other. Thus the binding energies of the electronic states are confirmed with two separate measurements. The values of the excited **A** $^3\Pi_1$ and $^3\Pi_2$ states are reported from the magnified photoelectron spectra and confirmed in the full spectra. The full photoelectron spectrum is utilized in the measurement of the vertical detachment energy of the ground **X** state. The absence of an origin in the ground state

confirms the large bond length, resulting in poor Franck-Condon overlap and the large progression observed in the transition to the neutral. The vibrational spacing in the excited $^3\Pi_{1,2}$ states agrees extremely well to those of previous measurements, confirming our electronic states.

The spectrum of IBr^- (Figure 3.5) is similar to that of I_2^- (Figure 3.4),[22] which we suspected would be the case. We also predict that when IBr is solvated with CO_2, the spectrum will be similar to that of solvated I_2.[22] Solvation of IBr should result in an increase of binding energies and a spreading of the peak distribution as the electron-binding energy is distributed over the molecule and solvent. This set of spectra for the bare IBr^- will lead to further discoveries once a set of spectra are collected for the solvation of $IBr^-(CO_2)_n$.

References for Chapter III

1 D. W. Arnold, S. E. Bradforth, E. H. Kim, and D. M. Neumark, Journal of Chemical Physics **102** (9), 3510 (1995).

2 B. J. Greenblatt, M. T. Zanni, and D. M. Neumark, Journal of Chemical Physics **112** (2), 601 (2000).

3 A. Sanov, T. Sanford, S. Nandi, and W. C. Lineberger, Journal of Chemical Physics **111** (2), 664 (1999).

4 R. Mabbs, K. Pichugin, and A. Sanov, Journal of Chemical Physics **122** (17), 174305 (2005).

5 R. Mabbs, E. Surber, and A. Sanov, Journal of Chemical Physics **122** (5), 054308 (2005).

6 W. S. McGivern, R. J. Li, P. Zou, T. Nguyen, and S. W. North, Chemical Physics **249** (2-3), 237 (1999).

7 A. Stolow, A. E. Bragg, and D. M. Neumark, Chemical Reviews **104** (4), 1719 (2004).

8 E. Wrede, S. Laubach, S. Schulenburg, A. J. Orr-Ewing, and M. N. R. Ashfold, Chemical Physics Letters **326** (1-2), 22 (2000).

9 Y. S. Kim, Y. J. Jung, and K. H. Jung, Journal of Chemical Physics **107** (10), 3805 (1997).

10 K. P. Lawley, D. Austin, J. Tellinghuisen, and R. J. Donovan, Molecular Physics **62** (5), 1195 (1987).

11 M. Shapiro, M. J. J. Vrakking, and A. Stolow, Journal of Chemical Physics **110** (5), 2465 (1999).

12 P. Vogt, M. Schmitt, and W. Kiefer, Chemical Physics Letters **243** (1-2), 64 (1995).

13 M. J. J. Vrakking, D. M. Villeneuve, and A. Stolow, Journal of Chemical Physics **105** (13), 5647 (1996).

14 T. Yukiya, N. Nishimiya, and M. Suzuki, Journal of Molecular Spectroscopy **214** (2), 132 (2002).

15 X. N. Zheng, M. C. Heaven, and J. Tellinghuisen, Journal of Molecular Spectroscopy **164** (1), 135 (1994).

16 V. Dribinski, J. Barbera, J. P. Martin, A. Svendsen, M. A. Thompson, R. Parson, and W. C. Lineberger, Journal of Chemical Physics **125** (13), 133405 (2006).

17 T. Sanford, D. Andrews, J. Rathbone, M. Taylor, F. Muntean, M. Thompson, A. B. McCoy, R. Parson, and W. C. Lineberger, Faraday Discussions **127**, 383 (2004).

18 T. Sanford, S. Y. Han, M. A. Thompson, R. Parson, and W. C. Lineberger, Journal of Chemical Physics **122** (5), 054307 (2005).

19 T. J. Sanford, Ph.D. Thesis, University of Colorado, 2004.

20 A. V. Davis, R. Wester, A. E. Bragg, and D. M. Neumark, Journal of Chemical Physics **118** (3), 999 (2003).

21 E. Surber, R. Mabbs, and A. Sanov, Journal of Physical Chemistry A **107** (40), 8215 (2003).

22 H. Gomez, T. R. Taylor, and D. M. Neumark, Journal of Chemical Physics **116** (14), 6111 (2002).

23 C. Blondel, P. Cacciani, C. Delsart, and R. Trainham, Physical Review A **40** (7), 3698 (1989).

24 D. Hanstorp and M. Gustafsson, Journal of Physics B-Atomic Molecular and Optical Physics **25** (8), 1773 (1992).

25 R. S. Mulliken, Journal of Chemical Physics **55** (1), 288 (1971).

26 G. J. Rathbone, T. Sanford, D. Andrews, and W. C. Lineberger, Chemical Physics Letters **401** (4-6), 570 (2005).

27 W. C. Wiley and I. H. McLaren, Review of Scientific Instruments **26** (12), 1150 (1955).

28 L. Minnhagen, Arkiv for Fysik **21** (5), 415 (1962).

29 V. Dribinski, A. Ossadtchi, V. A. Mandelshtam, and H. Reisler, Review of Scientific Instruments **73** (7), 2634 (2002).

30 J. Pittner and P. Jungwirth, Chemical Physics Letters **321** (3-4), 281 (2000).

31 K. M. Ervin, T. M. Ramond, G. E. Davico, R. L. Schwartz, S. M. Casey, and W. C. Lineberger, Journal of Physical Chemistry A **105** (48), 10822 (2001).

32 D. R. T. Appadoo, P. F. Bernath, and R. J. Leroy, Canadian Journal of Physics **72** (11-12), 1265 (1994).

33 D. T. Radzykewycz, C. D. Littlejohn, M. B. Carter, J. O. Clevenger, J. H. Purvis, and J. Tellinghuisen, Journal of Molecular Spectroscopy **166** (2), 287 (1994).

34 W. Holzer, W. F. Murphy, and H. J. Bernstein, Journal of Chemical Physics **52** (1), 399 (1970).

35 X. N. Zheng, M. C. Heaven, and J. Tellinghuisen, Chemical Physics Letters **195** (2-3), 273 (1992).

36 J. O. Clevenger, Q. P. Ray, J. Tellinghuisen, X. Zheng, and M. C. Heaven, Canadian Journal of Physics **72** (11-12), 1294 (1994).

37 D. J. Auerbach, M. M. Hubers, A. P. M. Baede, and J. Los, Chemical Physics **2** (1), 107 (1973).

38 A. P. M. Baede, Physica **59** (3), 541 (1972).

Photoelectron Velocity Map Imaging Spectra of CuH^- and CuH_2^-

4.1 Introduction

While conducting studies on the copper-methoxy and copper methanol anions,[1] we became interested in studying copper hydride anions. We attempted to identify all possible species in the mass spectrum around the copper anion. The hydrides stood out as having possible contamination from the bare copper anion. After recording the photoelectron spectra of the copper hydride anions, we performed a literature search that revealed a photoelectron spectra of these simple molecules has not been previously reported. CuH has been studied previously by many different groups dating back to the 1920s. The most extensive studies were performed by Ringström in 1966. A series of publications by the Andrews group reported studies of copper hydrides utilizing H_2 matrix infrared spectra. These matrix infrared spectra were assigned using DFT calculations of the corresponding neutral molecules.

Reactions of the form $M + H_2 \rightarrow MH + H$ are important prototypes for the process of hydrogen splitting on transition metals. These reactions can proceed through an intermediate MH_2. One class of intermediates, the copper hydrides, has been the subject of numerous theoretical and experimental studies. These hydrides are important for understanding the absorption of hydrogen onto metal surfaces in heterogeneous catalysis.[2] As a result, there have been a number of spectroscopic[3-10] and computational[2,9,11-19] studies of copper monohydride, while the copper dihydride has been primarily limited to theoretical studies.

Copper monohydride emission and absorption spectra were first observed more than eighty years ago.[4] The next major advance was Ringström's 1966 study,[7] in which he characterized five CuH electronic states. Since then, several groups have characterized a number of CuH singlet and triplet states.[6,8-10,20-23] The most recent work was performed by

Andrews and co-workers on laser-ablated Cu atoms with hydrogen in low temperature matrices.[3,9] The experimental studies were accompanied by increasingly sophisticated calculations of the energies and properties of the low-lying states of CuH.[9,12-15,18,24,25] Notably missing in the experimental work of copper hydride, however, has been detection of the lowest triplet state, **a** $^3\Sigma^+$. This state is a prominent feature of the CuH^- photoelectron spectrum reported here.

Copper dihydride has proven much more difficult to investigate experimentally and theoretically than the monohydride. The difficulty is the complex electronic structure of CuH_2, which includes bent and linear excited states, conical intersections, and multiple important electronic configurations. Only recently have elaborate calculations begun to provide consistent electronic structures of CuH_2.[13] Most theoretical work has addressed barriers to CuH_2 formation, CuH_2 energies relative to Cu (^2S) + H_2 and CuH + H, adiabatic correlations, and conical intersections.[2,3,9,13,16,17] Theory has shown that the ground state sits approximately 0.45 eV above the Cu (^2S) + H_2 asymptote, with a barrier of about 1.4 eV from the reactants.[7,8,10,13] However, calculations have shown the CuH_2 molecule to be unstable with respect to decomposition to CuH + H.

On the experimental front, Andrews and co-workers recently detected infrared absorptions in a hydrogen matrix that they could attribute to CuH_2 and CuH_2^-.[3,9] However, there have been no reports for the detection of isolated CuH_2. Previous matrix attempts to obtain copper dihydride only provided evidence for CuH.[6] A major finding was that the formation of copper dihydride must be accomplished by reacting excited Cu (^2P) atoms and H_2 molecules to form the metastable intermediate CuH_2.[6,12,13,26]

In this chapter, I report the production and photoelectron spectra of CuH^- and CuH_2^- anions. The CuH_2^- photoelectron spectra give electron affinities of the copper dihydride and

the direct observations of a previously unobserved linear HCuH intermediate in the hydrogen-splitting reaction and the lowest triplet state of CuH.

4.2 Experiment

The photoelectron spectroscopy of copper hydrides is carried out using a velocity map-imaging photoelectron spectrometer, described previously in Chapter 2.[27] The sputter ion source gas consists of argon saturated with water vapor at 45 psi. The gas mixture is expanded into the chamber using a pulsed General Valve (series 9). The emerging molecular beam initiates a discharge between a copper cathode (–3 kV) and a stainless steel pin held at ground potential, producing Cu^- anions and small clusters. The anions react with the gas mixture producing a variety of anions, including CuH^- and CuH_2^-.[28] The ion of interest is mass selected by a time-of-flight mass spectrometer. A typical mass spectrum is displayed in Figure 4.1. The ion selected is intersected with a 2 mJ (355 or 600 nm) laser pulse in a velocity map-imaging photoelectron spectrometer.[27,29] The three dimensional photoelectron image is reconstructed using the BASEX inversion algorithm.[30] The photoelectron energy scale is calibrated using well known Cu ^2S, $^2D_{3/2,5/2} \leftarrow Cu^-$ ^1S transitions[31] and is displayed in Figure 4.2. For electron kinetic energies below 200 meV, electron-binding energies can be determined with an accuracy of ±0.005 eV or better.[27]

The interpretation of the experimental results was aided by DFT calculations by the Gaussian suite of programs[32] using the B3LYP method with the 6-311++G(3dp,3df) and SDD basis sets for hydrogen and copper, respectively. These calculations supplement the extensive earlier theoretical studies.[5,6,9,13-15,17] The optimized geometries and vibrational frequencies of the anion and neutral obtained in the earlier calculations are utilized in Franck-Condon simulations of the photoelectron spectra using the PESCAL program.[33] Only the absolute value of Δr can be determined from the harmonic Franck-Condon simulations, and the sign of Δr must be obtained from calculated structures of the anion and neutral.

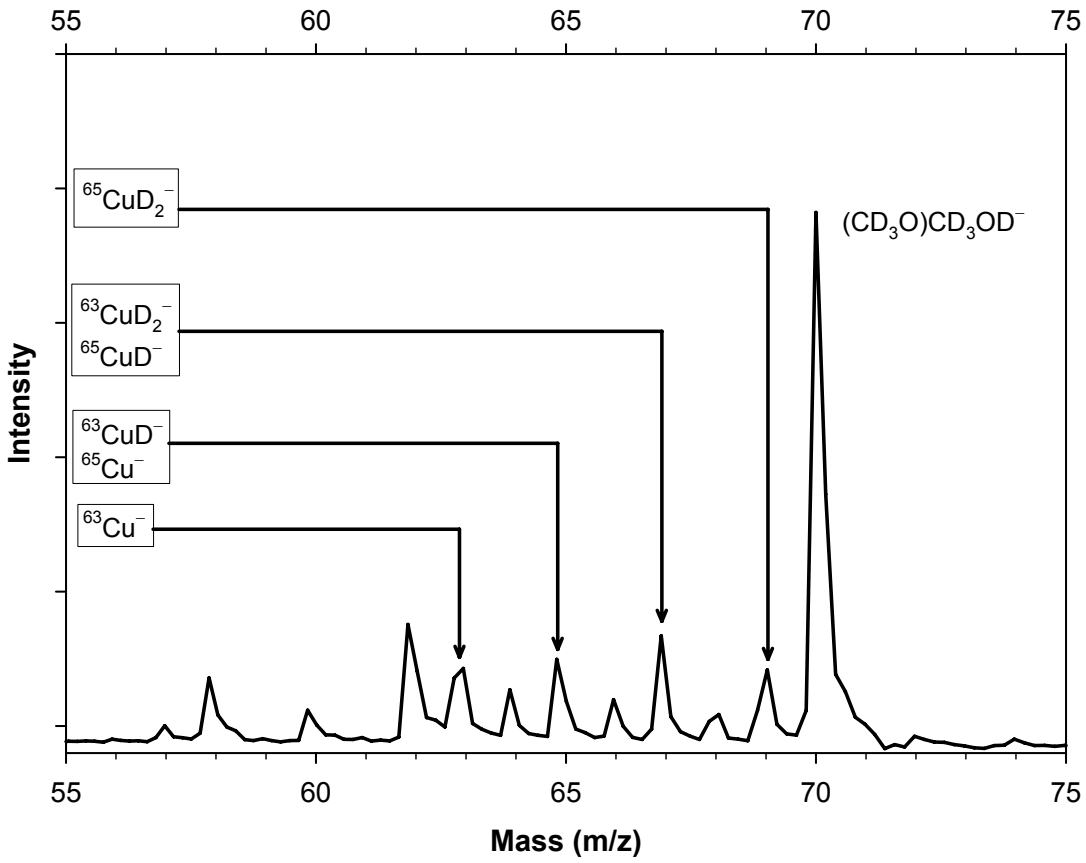

Figure 4.1 Time-of-flight mass spectrum obtained from a pulsed source. Mass peaks are labeled accordingly. Sputtered copper with methanol-d_4.

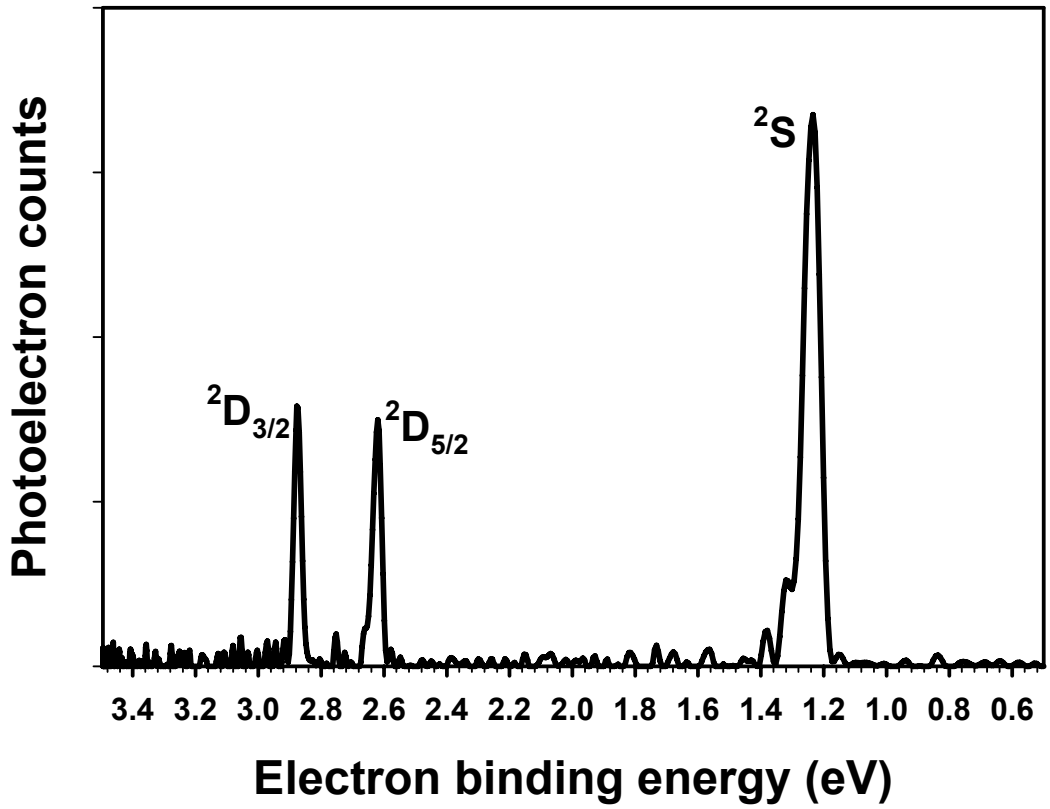

Figure 4.2 355 nm Cu^- photoelectron spectra. Transitions to the three lowest-lying electronic states of Cu are shown and labeled for reference.

4.3 Results and Discussion

4.3.1 CuH and CuD

The CuH $^1\Sigma^+$ ground state arises from the combination of the Cu $3d^{10}4s$ and the H 1s orbitals giving a σ^2 bonding HOMO. Adding an additional electron forms the anion in the $^2\Sigma^+$ state, a $\sigma^2\sigma^*$ configuration.[14] The lowest energy excited **a** $^3\Sigma$ state of CuH arises from mixing of the Cu $3d^{10}4s$ and H^* 1s orbitals. It is formed by photodetachment from the σ orbital in the anion, giving rise to a $\sigma\sigma^*$ configuration. Both states are accessible by single electron photodetachment from $\sigma^2\sigma^*$ **X** $^2\Sigma^+$ CuH^-. The lowest-excited CuH singlet state, **A** $^1\Sigma$, does not arise from this configuration, but rather is formed from the Cu^* $3d^94s^2$ and H 1s orbitals, giving rise to a $d^9\sigma^2\sigma^*$ configuration,[14] which is also accessible by photodetachment of a Cu d-electron from CuH^-. The energy difference between the **X** $^1\Sigma^+$ and **A** $^1\Sigma$ states is well known,[7] but the **a** $^3\Sigma$ state has not previously been observed. Figure 4.4 depicts the photoelectron spectra of CuH^- recorded at 355 nm; the CuH^- photoelectron spectra are completely consistent with the qualitative expectations described above. Comparison of the observed peak separations with the known CuH **A** $^1\Sigma\leftarrow$ **X** $^1\Sigma$ splitting enables the identification of the transitions shown in Figures 4.4 and 4.6.

Raw Image BASEX Reconstructed Image

Figure 4.3 Photoelectron image of CuH^- recorded at 355 nm. The raw image is on the left side, and the BASEX-reconstructed image is on the right side.

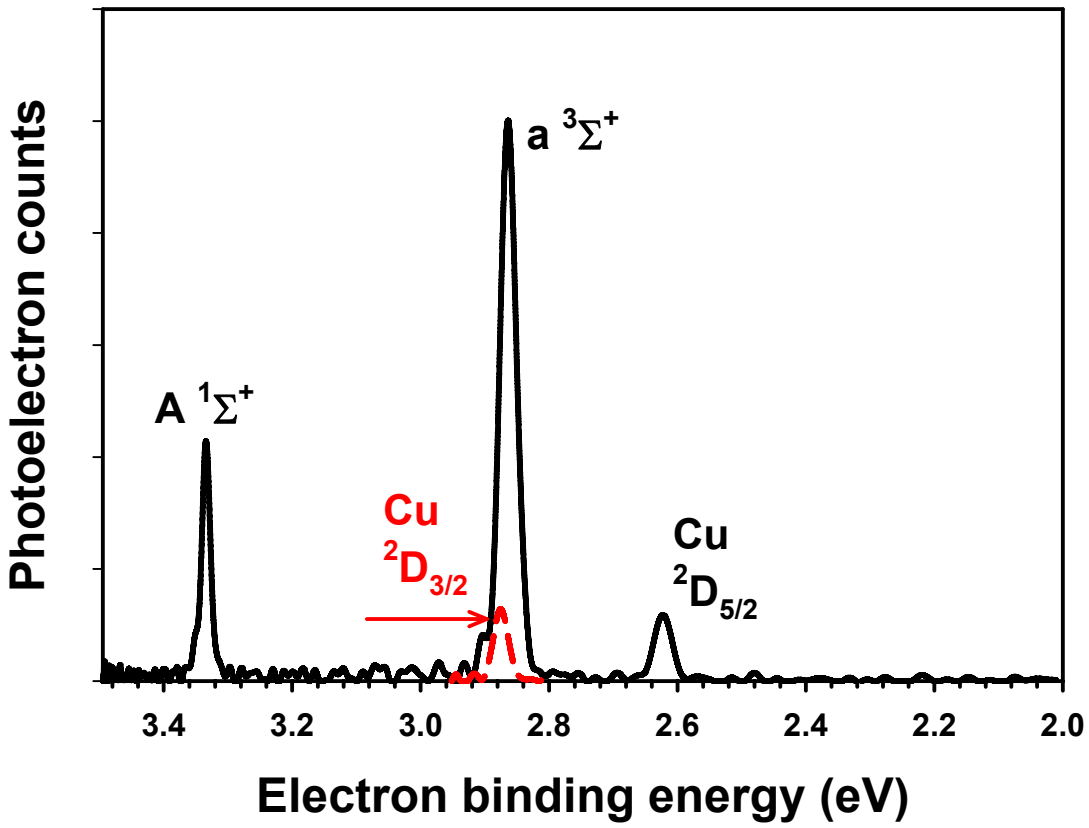

Figure 4.4 Photoelectron spectra of CuH^- recorded at 355 nm. They are obtained from the integration of the BASEX image in Figure 4.3. The Cu $^2D_{3/2}$ state is displayed underneath the $^3\Sigma$ state of CuH. The spectrum has been cut off at 2 eV to focus the attention on the excited states.

As the lowest electron kinetic energies are most accurately determined, I derived the electron affinity of CuH from the energy of the transition to produce the **A** $^1\Sigma$ CuH state. The result is EA(CuH) = 0.444(6) eV. Two peaks are seen, corresponding to ν=0 and 1 of **X** $^1\Sigma$ CuH, with a separation of 1835(50) cm^{-1}, in reasonable agreement with the very accurate 1866 cm^{-1} obtained by Brault and Bernath.[10] This short vibrational progression allows the use of the Franck-Condon simulation program to obtain $|\Delta r|$(**X** CuH – **X** CuH^-) = 0.104(3) Å. As the added electron in the anion is antibonding, I obtain r_e(**X** CuH^-) = 1.567(3) Å. A measurement of the anion's equilibrium bond length is placed at 1.567(3) Å. Through the use of the Franck-Condon simulations, the neutral bond length was fixed, while the anion bond length was adjusted until a representative spectrum was reproduced.

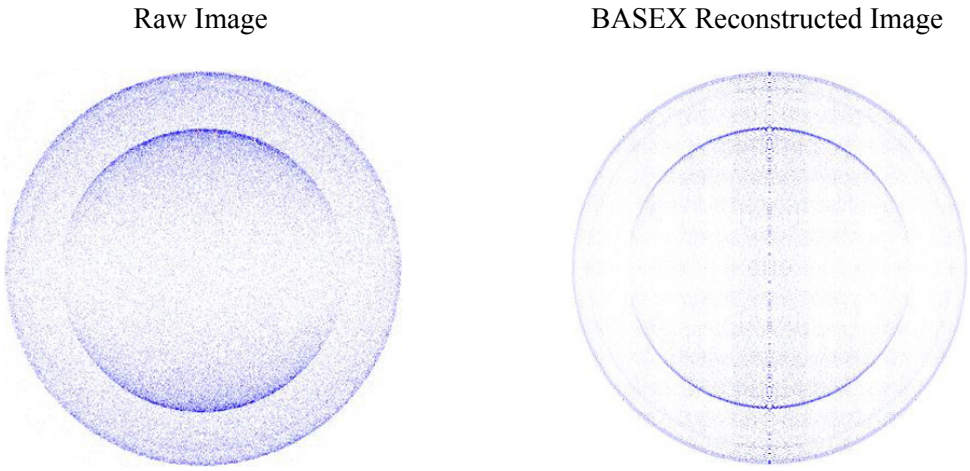

Figure 4.5 Photoelectron image of CuH^- recorded at 600 nm. The raw image is on the left side, and the BASEX-reconstructed image is on the right side.

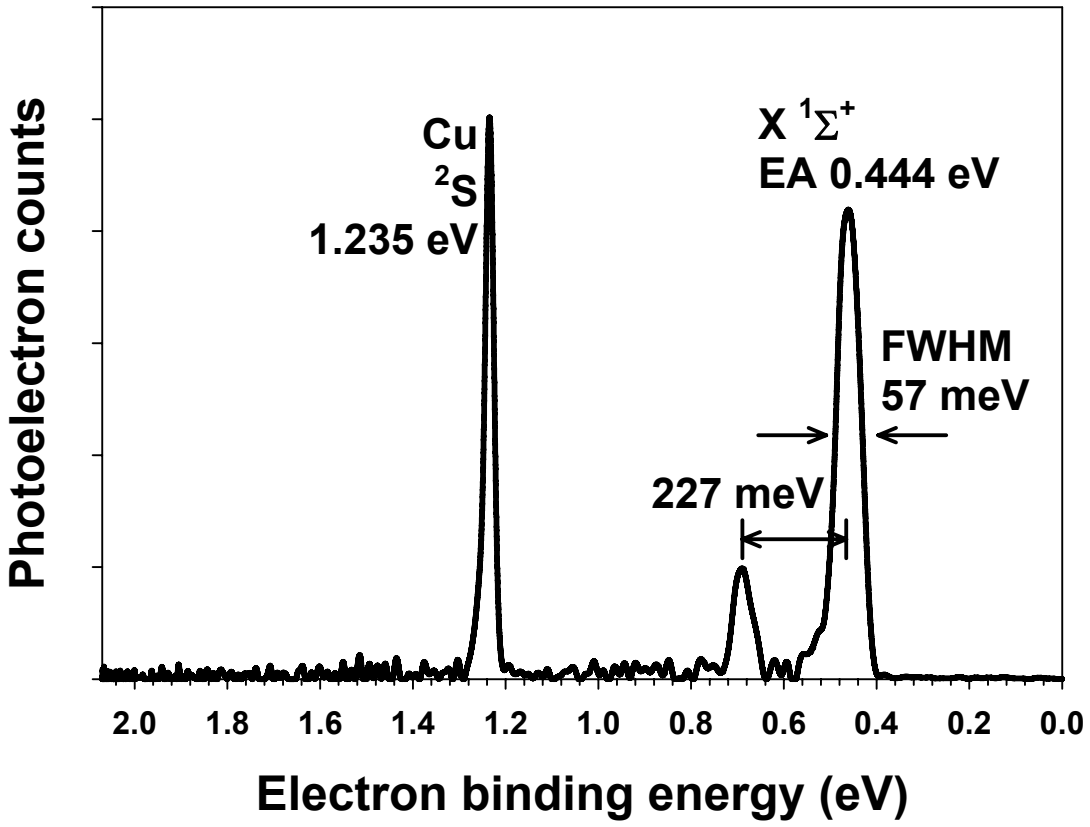

Figure 4.6 Photoelectron spectrum of CuH^- recorded at 600 nm, obtained from integration of the BASEX image in Figure 4.5.

Measurement of the electron affinity allows for the measurement of the dissociation energy (D_0) of the anion. Utilizing the value $D_0(CuH) = 2.84(4)$ eV, measured by Rao[34] in a thermochemical cycle with EA(CuH), gives $D_0(\mathbf{X}\ CuH^- \rightarrow Cu^- + H) = 2.05(6)$ eV; the weaker anion bond is expected because of the antibonding character of the added electron. Though not shown here the photoelectron spectrum of CuD^- was recorded to confirm our spectral assignments. It is included in Appendix C. Table 4.1 summarizes our view of the "best" thermochemical values for those states of CuH and CuH^- reported here. I use the present results where appropriate.

Table 4.1 Recommended spectroscopic constants for ^{63}CuH and ^{63}CuD. Values marked with an asterisk are obtained from spectra reported in this chapter.

State	$T_{0\text{-}0}$ (eV)	$\omega_{1\text{-}0}$ (cm^{-1})	r_e (Å)
^{63}CuH **A** $^1\Sigma^+$	2.890[b]	1610.4[c]	1.5663[g]
^{63}CuH **a** $^3\Sigma^+$	2.418(6)*	1762[a,f]	1.567(5)[e,*]
^{63}CuH **X** $^1\Sigma^+$	0	1866.4[d]	1.46263[c]
$^{63}CuH^-$ **X** $^2\Sigma^+$	-0.444(6)*	1564[f]	1.567(3)*
^{63}CuD **A** $^1\Sigma^+$	2.892[b]	1171.9[b]	1.566(3)[b]
^{63}CuD **a** $^3\Sigma^+$	2.425(6)*	1174[a,f]	1.567(5)[e,*]
^{63}CuD **X** $^1\Sigma^+$	0	1346.2[c]	1.4625(5)[c]
$^{63}CuD^-$ **X** $^2\Sigma^+$	-0.439(6)*	1115[f]	1.567(3)*

a – Calculated at the CASSCF level by Marian [15].
b – Measured by Ringström [7].
c – Reported in Herzberg [35].
d – Measured by Brault using Fourier transform emission spectroscopy [10].
e – based upon non-observation of a $\Delta v = +1$ transition in the photoelectron spectrum.
f – DFT calculations obtained from the B3LYP method and the 6-311++G(3dp,3df)/SDD basis sets for hydrogen and copper respecively
g- Measured by Bernath in an infrared emission spectra [8]

Contamination from the copper anion appears in our photoelectron spectra. It occurs because of the mass separation of 1 amu between Cu^- and CuH^-, combined with the large photodetachment cross section of copper. The 600 nm spectra displays the Cu ^2S state, and the Cu $^2D_{5/2}$ state is present in the 355 nm spectra. The copper $^2D_{3/2}$ state is encompassed by the **a** $^3\Sigma$ state of CuH and is shown in the spectra (Figure 4.4) as a trace located underneath the **a** peak. The excitation energy of the previously unobserved **a** $^3\Sigma$ state, 2.425(6) eV, is determined by measurement of the **A** $^1\Sigma^+$ - **a** $^3\Sigma$ splitting and compared it to the ~2.29 eV obtained in several calculations.[14-16] A vibration progression is not observed in our spectra, indicating that the detached electron was nonbonding and r_e(**a** $^3\Sigma^+$)=1.567(5) Å, the same as for the anion. This result compares well with the calculated bond length of 1.54 Å.[15]

The peak with the highest-binding energy corresponds to the known separation between the ground state and the first-excited state of the singlet state, **A** $^1\Sigma^+$.[7,15] The photon energy was insufficient to access the ν=1 transition, precluding measurement of either the bond length or vibration frequency. Previous experimental studies give r_e(**A** $^1\Sigma^+$ CuH) = 1.572 Å, with ω_e = 1610cm^{-1}.[7,35]

4.3.2 CuH_2 and CuD_2

The ground state configuration of copper dihydride has C_{2v} symmetry with a $(5a_1)^2(3b_2)^1$ orbital configuration, yielding a bent $^2B_2$ state. When an extra electron is added, the lowest energy configuration of the anion rearranges into a linear $(3\sigma_g)^2(2\sigma_u)^2$ configuration, giving rise to the **X** $^1\Sigma^+$ state. The sputter ion source yields intense beams of CuH_2^-. Electron photodetachment produces both the bent $^2B_2$ CuH_2 and a low-lying **A** $^2\Sigma_g^+$ excited state with a geometry very similar to that of the anion.[13] Thus, both of these states should be observed in the CuH_2^- photoelectron spectrum: the ground state should have

extensive, but poorly resolved, vibrational progressions, and the excited state should have a sharp near-diagonal transition dominating the spectra. These qualitative expectations are exactly what is observed in the 355 nm photoelectron spectrum of CuD_2^-, as seen in Figure 4.8. The velocity map image is presented in Figure 4.7. Photoelectron spectra of CuH_2^- and CuD_2^- were recorded to confirm the spectral assignments, but we report only on the latter, as this provided a sharper photoelectron spectrum. The photoelectron spectrum of CuH_2^- is included in Appendix C.

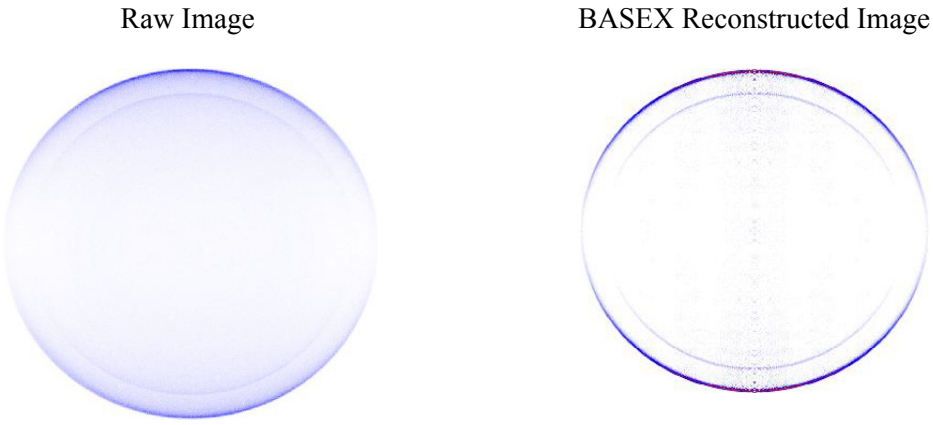

Figure 4.7 Photoelectron image of CuD_2^- recorded at 355 nm. The raw image is on the left side, and the BASEX reconstructed image is on the right side.

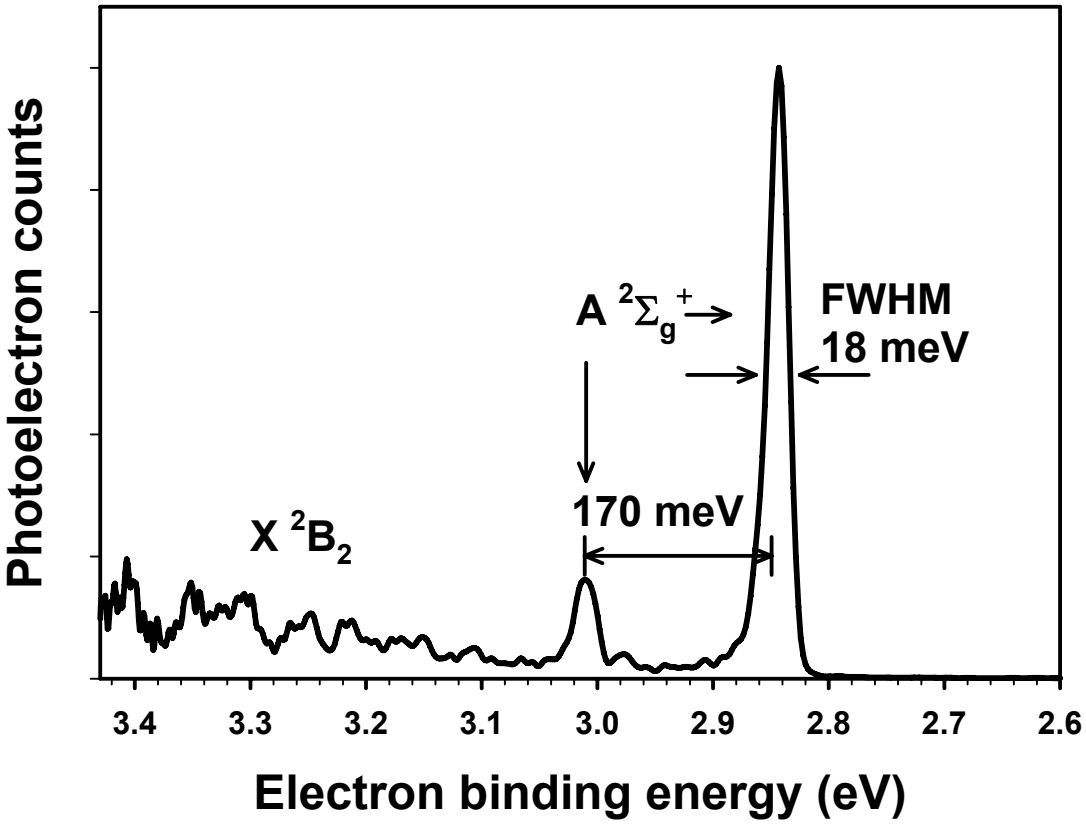

Figure 4.8 Photoelectron spectrum of $^{65}CuD_2^-$ at 355 nm. The intense peak is assigned as the transition **A** $^2\Sigma_g$ in CuD_2, with a symmetric stretch of 1369(40) cm^{-1}. An extended vibrational progression is present at higher-binding energies and is assigned as the **X** $^2B_2$ ground state.

The photoelectron spectrum is dominated by a strong transition to the linear-excited $\mathbf{A}\,^2\Sigma_g^+$ state of CuD_2. Photodetachment occurs from the $3\sigma_g$ orbital in the anion, as this has been shown to be lower in energy than detachment from the $2\sigma_u$ orbital. This result contrasts with other IB transition metal hydrides where the $2\sigma_u$ orbital is lower.[11-13] A short progression in the symmetric stretch mode is observed with a frequency of 1370(40) cm^{-1}; the assignment to a vibrational progression was confirmed by hydrogen substitution. A binding energy of 2.841(5) eV is measured for the **A** state in the photoelectron spectra. Photoelectron ejection is strongly peaked parallel to the laser polarization vector, with an anisotropy β of 1.8(1), consistent with photodetachment removing an electron from the $3\sigma_g$ orbital in the anion.[11-13] With the observed $\nu_{0\text{-}1}$ vibration and the use of the PESCAL program, the equilibrium bond length of the anion is calculated using a harmonic Franck-Condon intensity analysis. The **A** state bond length is fixed to the values calculated by Chambaud at 1.52 Å.[13] From these calculated values, a change in the equilibrium bond length is calculated at |Δr(Cu-H)| to be 0.04 Å. Our DFT calculations show the anion to have the longer Cu-H bond length, providing the sign associated with |Δr(Cu-H)| above. As $\mathbf{A}\,^2\Sigma_g^+$ CuH2 has not been previously observed, we employ the much higher level $\mathbf{A}\,^2\Sigma_g^+$ CuH_2 bond length calculated by Chambaud (1.52 Å)[13] to obtain the anion bond length in the anion as 1.56(2) Å. A simulation of the spectra calculated in PESCAL using the calculated geometries and frequencies is shown in Figure 4.9. Table 4.2 summarizes my view of the "best" thermochemical values for those states of CuH_2 and CuH_2^- reported here, using the present results where appropriate.

Table 4.2 Recommended spectroscopic constants for $^{65}CuD_2$ and $^{65}CuH_2$. Values marked with an asterisk are obtained from spectra reported in this chapter

State	Electron binding energy (eV)	ν (cm^{-1})				H-Cu-H r_e (Å)
		ν_1	ν_2	ν_3	ν_4	
$^{65}CuD_2$ **A** $^2\Sigma_g^+$	2.841(5)*	592.8[f]	592.8[f]	1211[f]	1369(40)[d*]	1.52[a]
$^{65}CuD_2$ **X** $^2B_2$	2.60(5)[b]	1196[f]	450(60)[d] (458.5[c])	1291[f]		1.468[a]
$^{65}CuD_2^-$ **X** $^1\Sigma_g^+$	0*	470[f]	470[f]	1065[f]	1107.3[c]	1.56(3)*
$^{65}CuH_2$ **A** $^2\Sigma_g^+$	2.853(5)*	817[g]	817[g]	1808[g]	1884(40)[d*]	1.52[a]
$^{65}CuH_2$ **X** $^2B_2$	2.60(5)[a]	1935[e]	636.5[c] (685[e])	1799[e]		1.468[a]
$^{65}CuH_2^-$ **X** $^1\Sigma_g^+$	0*	655[f]	655[f]	1065[f]	1517.8[c]	1.56(3)*

a – From Chambaud X-A separation, MRCISD.[13]
b – Chambaud [12], X-A separation as a above, corrected for H-D zero point differences, using the calculated harmonic CuH_2 vibrational energies.
c - IR absorption in a hydrogen matrix.[9]
d – Measured in photoelectron spectra
e – Chambaud anharmonic frequencies calculated at the MRCISD level.[13]
f – DFT calculations obtained from the B3LYP method and the 6-311++G(3dp,3df)/SDD basis sets for hydrogen and copper respecively
g – MP2-MP4 calculations performed by Fitzpatrick.[17]

The extended, unresolved vibrational progression present in the spectrum arises from transitions to high vibrational levels in the $^2B_2$ ground state. The extent of the progression arises from the large geometry difference between the linear anion and the bent neutral ground state. This progression is observed as a series of concentric rings radiating outward from the center of the photoelectron image toward the outer ring, which is assigned to the **A** state, as shown in Figure 4.7. Calculations by Chambaud[13] place the $^2B_2$ ground state ~0.2 eV below the A $^2\Sigma_g^+$ state, at least 0.3 eV below the binding energy where we first observe the extended progression. We cannot quantitatively simulate this progression, because the potential energy surfaces are to poorly known to obtain vibrational energy levels in the bent, linear, and transition regions. Moreover, the experimental spectra exhibit no clear vibrational peaks. Even a vertical detachment energy cannot be obtained from the data. Even though fully resolved vibration peaks are not observed, one can estimate a frequency of 450(60) cm^{-1} for the bending mode. This frequency compares well to the 458 cm^{-1} measured by Andrews and co-workers in a D_2 matrix, which provided the few experimentally measured values for copper dihydrides.[9] Nevertheless, the extended vibrational progression is consistent with the large predicted geometric change. If we use the calculated geometries for both states, employ harmonic vibrational frequencies, and assume the electronic transition matrix elements are the same for both ground and excited states, then we obtain the simulation shown in Figure 4.9. The only point to this qualitative CuH_2 **X** $^2B_2$ simulation is that both the absence of signal at the $^2B_2$ origin (2.6 eV) and the intensity of the extended progression in the energy range observed are consistent with expectations. With this simulation, the ground state of the copper dihydride should possess a symmetric H–Cu–H bond length of 1.468 Å with a bond angle of 121.6°.[13]

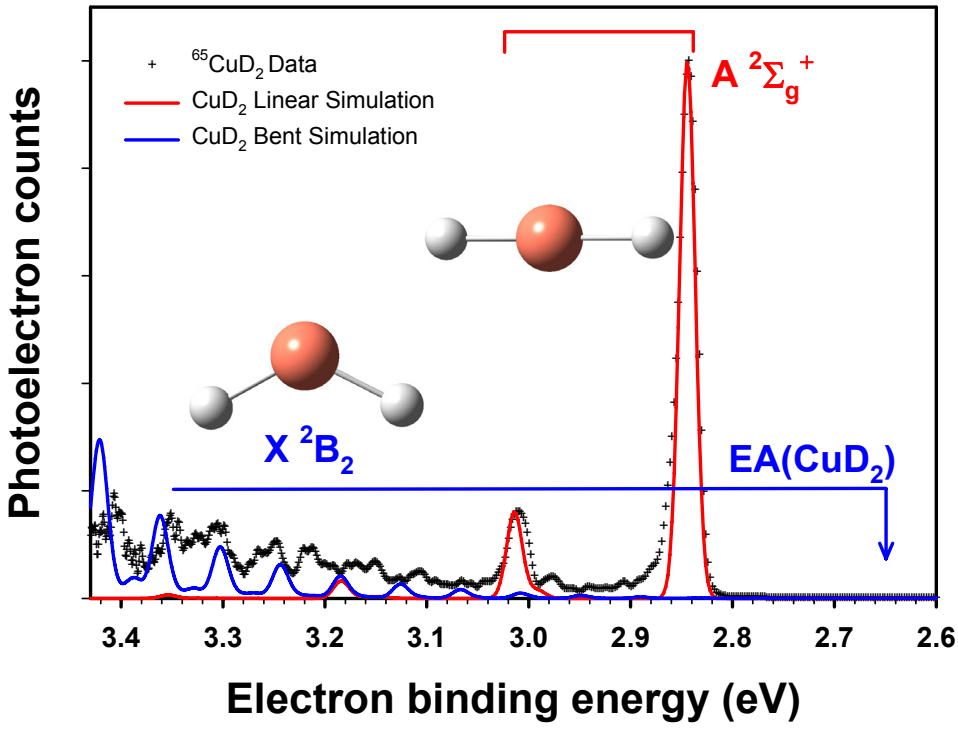

Figure 4.9 Comparison of the photoelectron spectrum of CuD_2 with the simulated spectrum. As a consequence of the large geometry difference between the linear anion and bent ground state, there is no detectable photoelectron signal at $EA(CuD_2)$, as indicated by a vertical arrow. The simulation does not consider the major effects of the bent→linear transition and must be considered as being very qualitative.

While we cannot resolve transitions in the extended vibrational progression in the ground state of copper dihydride, we can obtain EA(CuH_2) as the difference between the measured electron-binding energy of HCuH $\mathbf{A}\,^2\Sigma_g^+$ (2.853(5) eV) and the calculated separation between the $\mathbf{A}\,^2\Sigma_g^+$ state and CuH_2 $\mathbf{X}\,^2B_2$ ground state (0.255 eV).[13] This energy difference is obtained from Chambaud's MRCISD calculation of the splitting between these states (0.192 eV), but increased by 63 meV to account for zero point energies in both states by using Chambaud's CuH_2 **X** and **A** state harmonic frequencies.[13] If we estimate the uncertainty in the calculation to be 20%, or 0.05 eV, we obtain EA(CuH_2) = 2.60(5) eV. The mixing of measured and calculated energies is largely justified by the fact that the measured energy is an order of magnitude larger than the calculation correction used to obtain the electron affinity. Similarly, we find EA(CuD_2) = 2.60(5) eV.

This determination of EA(CuH_2) allows an estimate of the anion dissociation energy using a similar mix of calculation and measured energies. This strategy is justified by the fact that the theoretically determined quantities make a much smaller contribution to the dissociation energy than do the experimental ones. Chambaud reports D_e(CuH_2 $\mathbf{X}\,^2B_2$ – CuH + H) to be 1.32 eV.[13] Again, zero point corrections give D_0 to be 1.05 eV. Here we crudely estimate that the error in the calculated dissociation energy might be 0.2 eV. This dissociation energy, coupled with the electron affinities of CuH and CuH_2, form a thermochemical cycle to give $D_0(HCuH^- \rightarrow CuH^- + H)$ = 3.2(2) eV. Even with the large uncertainty, it is clear that this bond is much stronger in the anion than in the ground state of the neutral molecule. Since we know from the first study that $D_0(CuH^- \rightarrow Cu^- + H)$=2.05(6) eV, this result also allows us to conclude that removing the first hydrogen atom from $HCuH^-$ is significantly easier than removing the second one.

4.4 Conclusion

The use of a dc-sputtering discharge source provides a way to produce significant quantities of copper hydride anions. The negative ion velocity map-imaging photoelectron spectra provide quantitative electron-binding and dissociation energies, yielding new insight into the bonding and structure of these small molecules. The photoelectron spectra of CuH^- exhibit three electronic transitions from the anion to the neutral state. The most prominent feature of our spectra is the excited **a** $^3\Sigma^+$ state, which contrasts with previous experimental work, lacking this feature.

An extended weak vibrational progression consistent with the bending mode of the ground state of CuH_2 is observed in the photoelectron spectra. However this progression provides an unreliable measurement of the vibrational frequency. The absence of a defined origin corresponding to the ground state is consistent with previous geometry calculations and spectral simulations. The distinct intense feature of our photoelectron spectra is assigned to the first excited $\mathbf{A}\,^2\Sigma_g^+$ state of copper dihydride, because of predictions resulting from previous geometry calculations. We have shown previous theory on copper hydrides correlates well with our experimental results. More work on the copper dihydrides still need to be done to provide a better splitting energy between the **X** and **A** states and a measurement the vibrational frequencies of the ground state. The ion production technique employed here will be useful for studies of other transition metal hydrides and may provide new insights into the use of transition metals for hydrogen-splitting processes.

References for Chapter IV

1 D. H. Andrews, Ph.D. Thesis, University of Colorado, 2006.

2 P. E. M. Siegbahn, M. R. A. Blomberg, and C. W. Bauschlicher Jr., Journal of Chemical Physics **81** (3), 1373 (1984).

3 L. Andrews and X. F. Wang, Journal of the American Chemical Society **125** (38), 11751 (2003).

4 R. Frerichs, Z. Phys. **20**, 170 (1923).

5 J. Niu, B. K. Rao, P. Jena, and M. Manninen, Physical Review B **51** (7), 4475 (1995).

6 G. A. Ozin and C. Gracie, Journal of Physical Chemistry **88** (4), 643 (1984).

7 U. Ringström, Arkiv för fysik **32**, 211 (1966).

8 J. Y. Seto, Z. Morbi, F. Charron, S. K. Lee, P. F. Bernath, and R. J. Le Roy, Journal of Chemical Physics **110** (24), 11756 (1999).

9 X. F. Wang, L. Andrews, L. Manceron, and C. Marsden, Journal of Physical Chemistry A **107** (41), 8492 (2003).

10 R. S. Ram, P. F. Bernath, and J. W. Brault, Journal of Molecular Spectroscopy **113** (2), 269 (1985).

11 J. García-Prieto, M. E. Ruiz, and O. Novaro, Journal of the American Chemical Society **107** (20), 5635 (1985).

12 J. García-Prieto, M. E. Ruiz, E. Poulain, G. A. Ozin, and O. Novaro, Journal of Chemical Physics **81** (12), 5920 (1984).

13 M. Guitou-Guichemerre and G. Chambaud, Journal of Chemical Physics **122** (20), 204325 (2005).

14 M. Hliwa, J. C. Barthelat, M. Pelissier, and F. Spiegelmann, Chemical Physics Letters **132** (2), 205 (1986).

15 C. M. Marian, Journal of Chemical Physics **94** (8), 5574 (1991).

16 M. T. Nguyen, M. A. McGinn, and N. J. Fitzpatrick, Journal of the Chemical Society-Faraday Transactions II **82**, 1427 (1986).

17 M. T. Nguyen, M. A. McGinn, and N. J. Fitzpatrick, Journal of Chemical Society, Faraday Transitions **82** (2), 69 (1986).

18 R. Pouamerigo, M. Merchan, I. Nebotgil, P. A. Malmqvist, and B. O. Roos, Journal of Chemical Physics **101** (6), 4893 (1994).

19 M. E. Ruiz, J. García-Prieto, and O. Novaro, Journal of Chemical Physics **80** (4), 1529 (1984).

20 C. M. Brown and M. L. Ginter, Journal of Molecular Spectroscopy **80** (1), 145 (1980).

21 W. Fernando, L. C. Obrien, and P. F. Bernath, Journal of Molecular Spectroscopy **139** (2), 461 (1990).

22 T. D. Varberg and K. M. Evenson, Journal of Molecular Spectroscopy **164** (2), 531 (1994).

23 S. P. Beaton and K. M. Evenson, Journal of Molecular Spectroscopy **142** (2), 336 (1990).

24 E. G. Para, E. Martinez, and J. M. Alvarino, Journal of Quantitative Spectroscopy & Radiative Transfer **30** (5), 439 (1983).

25 F. Castano, J. Dejuan, and E. Martinez, Spectrochimica Acta Part a-Molecular and Biomolecular Spectroscopy **38** (5), 545 (1982).

26 G. A. Ozin, J. G. McCaffrey, and D. F. McIntosh, Pure and Applied Chemistry **56** (1), 111 (1984).

27 G. J. Rathbone, T. Sanford, D. H. Andrews, and W. C. Lineberger, Chemical Physics Letters **401** (4-6), 570 (2005).

28 F. Muntean, M. S. Taylor, A. B. McCoy, and W. C. Lineberger, Journal of Chemical Physics **121** (12), 5676 (2004).

29 A. Eppink and D. H. Parker, Review of Scientific Instruments **68** (9), 3477 (1997).

30 V. Dribinski, A. Ossadtchi, V. A. Mandelshtam, and H. Reisler, Review of Scientific Instruments **73** (7), 2634 (2002).

31 R. C. Bilodeau, M. Scheer, and H. K. Haugen, Journal of Physics B: Atomic, Molecular and Optical Physics **31** (17), 3885 (1998).

32 M. J. Frisch, G. W. Trucks, H. B. Schlegel, G. E. Scuseria, M. A. Robb, J. R. Cheeseman, J. J. A. Montgomery, T. Vreven, K. N. Kudin, J. C. Burant, J. M. Millam, S. S. Iyengar, J. Tomasi, V. Barone, B. Mennucci, M. Cossi, G. Scalmani, N. Rega, G. A. Petersson, H. Nakatsuji, M. Hada, M. Ehara, K. Toyota, R. Fukuda, J. Hasegawa, M. Ishida, T. Nakajima, Y. Honda, O. Kitao, H. Nakai, M. Klene, X. Li, J. E. Knox, H. P. Hratchian, J. B. Cross, C. Adamo, J. Jaramillo, R. Gomperts, R. E. Stratmann, O. Yazyev, A. J. Austin, R. Cammi, C. Pomelli, J. W. Ochterski, P. Y. Ayala, K. Morokuma, G. A. Voth, P. Salvador, J. J. Dannenberg, V. G. Zakrzewski, S. Dapprich, A. D. Daniels, M. C. Strain, O. Farkas, D. K. Malick, A. D. Rabuck, K. Raghavachari, J. B. Foresman, J. V. Ortiz, Q. C. A. G. Baboul, S. Clifford, J. Cioslowski, B. B. Stefanov, G. Liu, A. Liashenko, P. Piskorz, I. Komaromi, R. L. Martin, D. J. Fox, T. Keith, M. A. Al-Laham, C. Y. Peng, A. Nanayakkara, M. Challacombe, P. M. W. Gill, B. Johnson, W. Chen, M. W. Wong, C. Gonzalez, and J. A. Pople, Gaussian 03 (Gaussian Inc., Pittsburgh PA, 2003).

33 K. M. Ervin, T. M. Ramond, G. E. Davico, R. L. Schwartz, S. M. Casey, and W. C. Lineberger, Journal of Physical Chemistry A **105** (48), 10822 (2001).

34 V. M. Rao, M. L. P. Rao, and P. T. Rao, Journal of Quantitative Spectroscopy & Radiative Transfer **25** (6), 547 (1981).

35 K. Huber and G. Herzberg, *Molecular Spectra and Molecular Structure, Constants of Diatomic Molecules*. (Van Nostrand Reinhold, New York, 1979).

Photoelectron Velocity Map-Imaging Spectroscopy of $CuCD_3O^-$

5.1 Introduction

The studies on copper methoxide developed out of curiosity during the investigation of the photoelectron spectra of copper methanol.[1] Our interest began with the idea that other species may be present in the mass spectra, shown in Figure 5.1. In an attempt to identify all relevant species in our mass spectra, a photoelectron spectrum was collected for the species on either side of the copper methanol anion, the molecule of interest. Upon examination of the spectra, we realized that copper methoxy was the relevant species, since it is the deprotanated form of the copper methanol complex. It is hypothesized to have a similar structure to that of copper hydroxide $CuOH^-$,[2,3] where the methyl group has been replaced by hydrogen.

A photoelectron spectrum of copper hydroxide was obtained by Misaizu,[4] but the spectra contained contamination from copper water, as they are only separated by one amu. This is the closest related system that has been previously reported. The copper hydroxide anion has a structure consisting of a bond between the copper and oxygen atom, with the hydrogen pointed towards the electronegative copper in a bent structure. The copper methoxide has a similar structure with a bond between the copper and oxygen with the copper atom sitting between two of the deuterium atoms, the third points away from the copper. Because a complete analysis has not been performed on copper methoxy, it will only be reported on very briefly here. A publication at a later date will report on copper methoxy in detail.

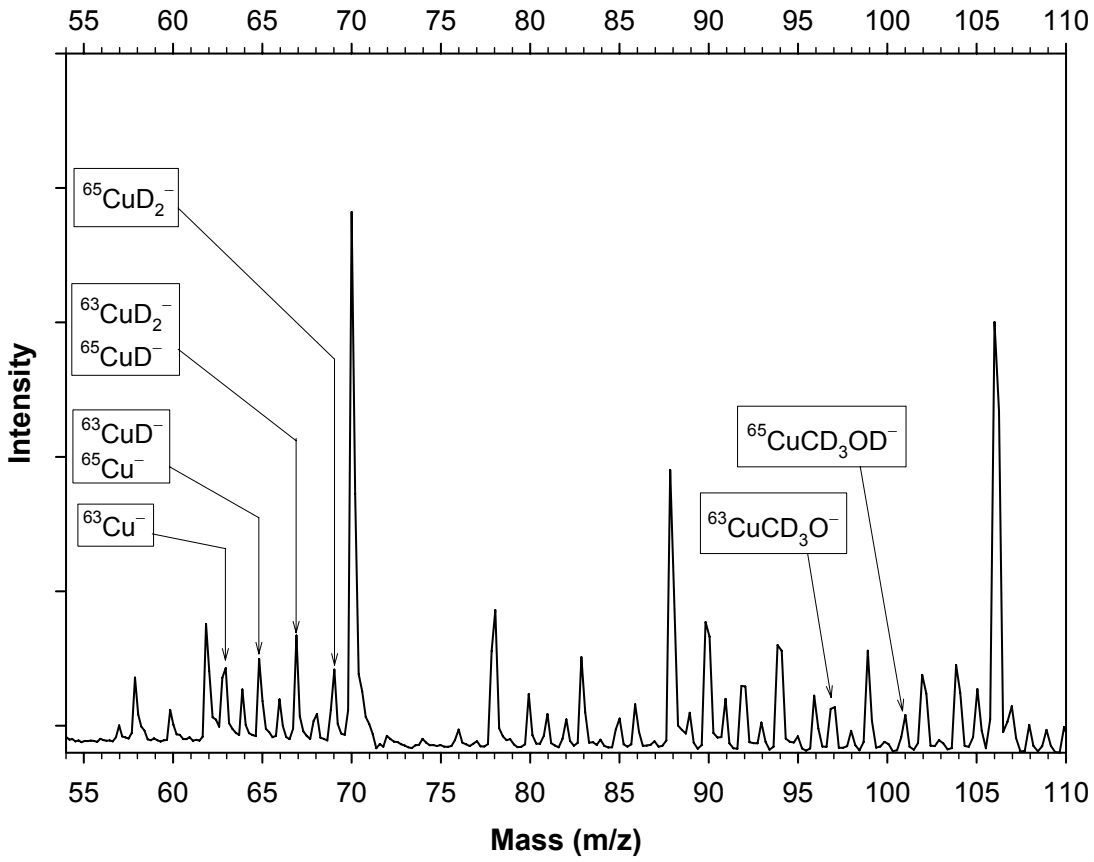

Figure 5.1 Time-of-flight mass spectrum obtained from a pulsed source. Peaks are labeled accordingly.

5.2 Brief Results

Two spectra were recorded, the first at a wavelength of 355 nm, as shown in Figure 5.3. The second was at 500 nm, as shown in Figure 5.5. Four electronic states were observed in the 355 nm spectra. A ground **X** ^{1}A' state, the first-excited triplet **A** ^{3}A' state, and two unidentified excited states. Only the ground **X** ^{1}A' state was observed in the 500 nm spectra. The ground state originated at 1.077(5) eV, which corresponds to the electron affinity. A vibrational progression was observed with a vibrational spacing of 528(50) cm^{-1}. This frequency has not yet been attributed to any part of the molecule.

The term-splitting energy between the ground state and first-excited state is 1.701(5) eV. We observed it with an electron binding energy of 2.778(5) eV. An observed vibrational progression of 520(50) cm^{-1} is present in the first-excited state of copper methoxy. As this vibrational progression is close to that of the ground state, the progression may correspond to the same type of vibration present in both the ground and excited states. A second-excited state is present with an electron-binding energy of 3.133(5) eV, corresponding to a splitting energy of 2.056(5) eV. Only one mode is observed for this second-excited state, and it isn't as prominent as the other electronic states. A third electronic state is observed in the spectra with the origin at 3.271(5) eV. This is separated from the ground state origin by 2.194(5) eV. A vibration is observed with a spacing of 335(50) cm^{-1}, that differs from the previous vibrations, indicating a new mode has been observed.

Aside from the electron-binding energies observed in the spectra and the vibrational spacing of the ground and first-excited states, not much is known about the copper methoxide molecule. A greater understanding of this molecule will be presented at a later date. Copper methoxy will be compared to the copper hydroxide molecule and investigated with *ab initio* calculations. The goal is to find the optimized geometries and energetics of the molecule.

Raw Image BASEX Reconstructed Image

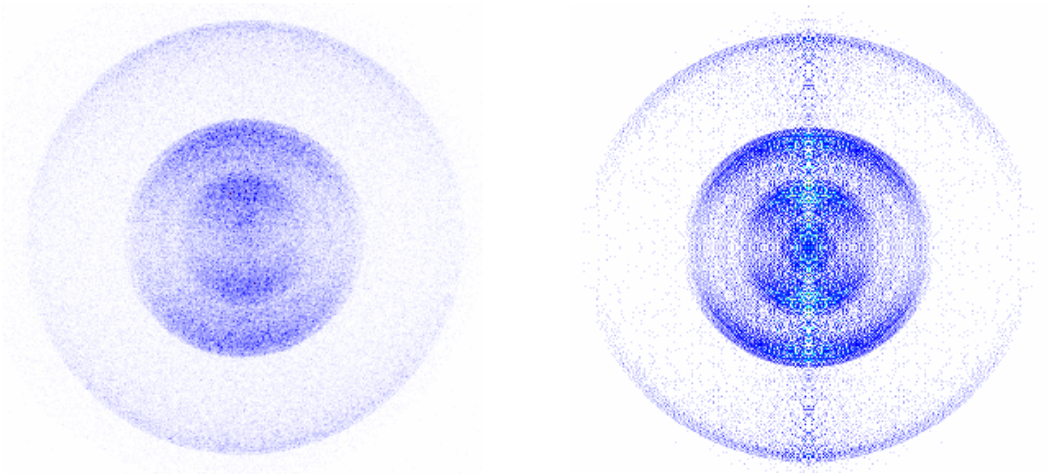

Figure 5.2 The raw $CuCD_3O^-$ photoelectron image is displayed on the left hand side, and the BASEX reconstructed image is presented on the right hand side. The image was recorded with a wavelength of 355 nm.

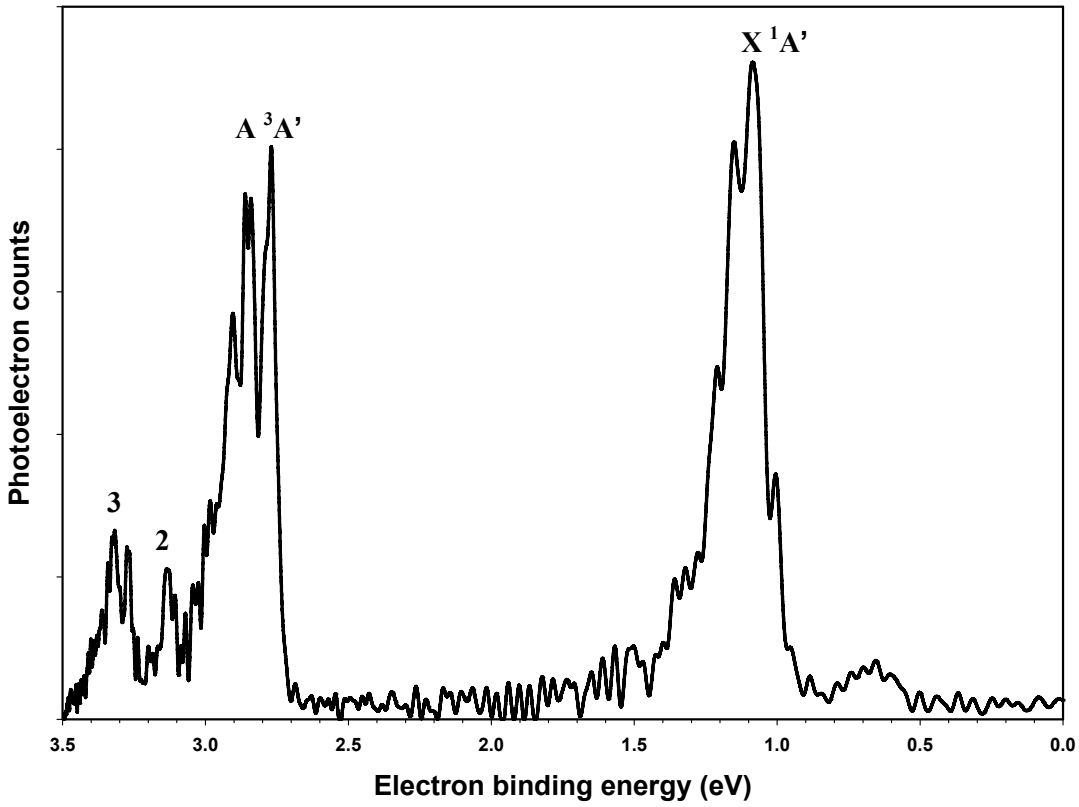

Figure 5.3 Photoelectron spectra of $CuCD_3O^-$ recorded at a wavelength of 355 nm.

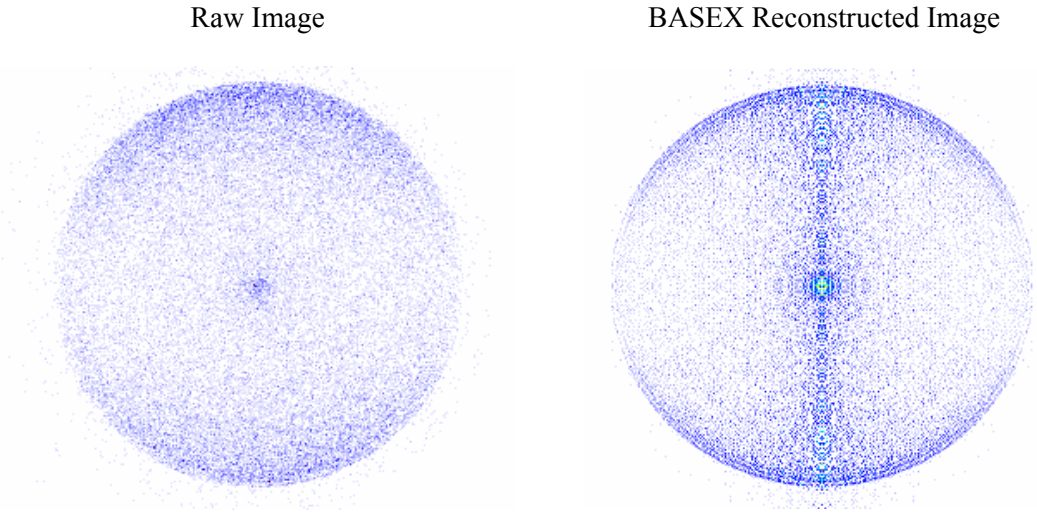

Figure 5.4 The raw $CuCD_3O^-$ photoelectron image is displayed on the left hand side, and the BASEX reconstructed image is presented on the right hand side. The image was recorded with a wavelength of 500 nm.

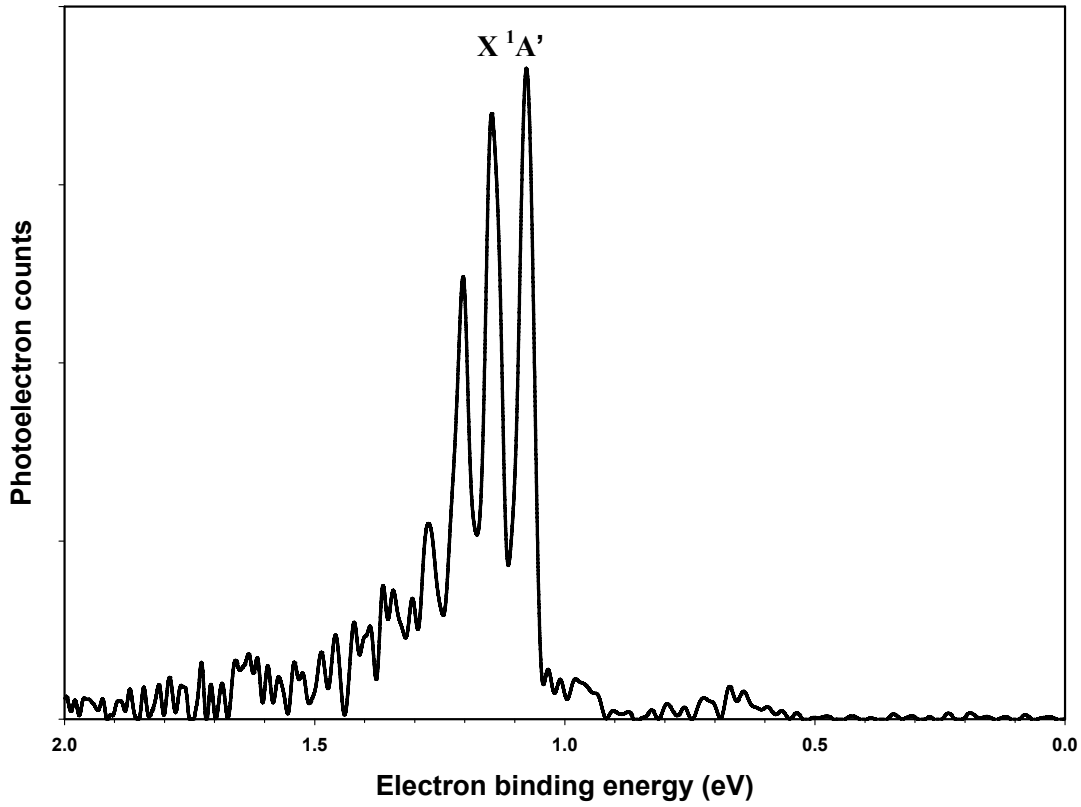

Figure 5.5 Photoelectron spectra of $CuCD_3O^-$ recorded at a wavelength of 500 nm.

References for Chapter V

1 D. H. Andrews, Ph.D. Thesis, University of Colorado, 2006.

2 S. Y. Wang, A. Paul, N. J. DeYonker, Y. Yamaguchi, and H. F. Schaefer, Journal of Chemical Physics **123** (1) (2005).

3 C. G. Zhan and S. Iwata, Chemical Physics Letters **232** (1-2), 72 (1995).

4 F. Misaizu, K. Tsukamoto, M. Sanekata, and K. Fuke, Surface Review and Letters **3** (1), 405 (1996).

Bibliography

Advances in Gas Phase Ion Chemistry, edited by N. G. Adams and L. M. Babcock (JAI Press Inc., 1992), Vol. 1.

D. H. Andrews, Ph.D. Thesis, University of Colorado, 2006.

L. Andrews and X. F. Wang, Journal of the American Chemical Society **125** (38), 11751 (2003).

D. R. T. Appadoo, P. F. Bernath, and R. J. Leroy, Canadian Journal of Physics **72** (11-12), 1265 (1994).

D. W. Arnold, S. E. Bradforth, E. H. Kim, and D. M. Neumark, Journal of Chemical Physics **102** (9), 3510 (1995).

D. J. Auerbach, M. M. Hubers, A. P. M. Baede, and J. Los, Chemical Physics **2** (1), 107 (1973).

A. P. M. Baede, Physica **59** (3), 541 (1972).

S. P. Beaton and K. M. Evenson, Journal of Molecular Spectroscopy **142** (2), 336 (1990).

P. F. Bernath, *Spectra of atoms and molecules*. (Oxford University Press, New York, 1995).

R. C. Bilodeau, M. Scheer, and H. K. Haugen, Journal of Physics B: Atomic, Molecular and Optical Physics **31** (17), 3885 (1998).

S. J. Blanksby and G. B. Ellison, Accounts of Chemical Research **36** (4), 255 (2003).

C. Blondel, P. Cacciani, C. Delsart, and R. Trainham, Physical Review A **40** (7), 3698 (1989).

C. M. Brown and M. L. Ginter, Journal of Molecular Spectroscopy **80** (1), 145 (1980).

W. G. Brown, Physics Review **42**, 355 (1932).

S. H. V. Bruckner, S. Ludwig, Journal of Modern Optics **40** (2), 187 (1993).

F. Castano, J. Dejuan, and E. Martinez, Spectrochimica Acta Part a-Molecular and Biomolecular Spectroscopy **38** (5), 545 (1982).

D. W. Chandler and P. L. Houston, Journal of Chemical Physics **87** (2), 1445 (1987).

J. O. Clevenger, Q. P. Ray, J. Tellinghuisen, X. Zheng, and M. C. Heaven, Canadian Journal of Physics **72** (11-12), 1294 (1994).

Coherent, *Coherent Laser Systems*. (Coherent, Santa Clara, CA, 2000).

A. V. Davis, R. Wester, A. E. Bragg, and D. M. Neumark, Journal of Chemical Physics **118** (3), 999 (2003).

L. Dinu, A. Eppink, F. Rosca-Pruna, H. L. Offerhaus, W. J. van der Zande, and M. J. J. Vrakking, Review of Scientific Instruments **73** (12), 4206 (2002).

V. Dribinski, J. Barbera, J. P. Martin, A. Svendsen, M. A. Thompson, R. Parson, and W. C. Lineberger, Journal of Chemical Physics **125** (13), 133405 (2006).

V. Dribinski, A. Ossadtchi, V. A. Mandelshtam, and H. Reisler, Review of Scientific Instruments **73** (7), 2634 (2002).

P. C. Engelking, G. B. Ellison, and W. C. Lineberger, Journal of Chemical Physics **69** (5), 1826 (1978).

A. Eppink and D. H. Parker, Review of Scientific Instruments **68** (9), 3477 (1997).

K. M. Ervin, J. Ho, and W. C. Lineberger, Journal of Chemical Physics **91** (10), 5974 (1989).

K. M. Ervin, T. M. Ramond, G. E. Davico, R. L. Schwartz, S. M. Casey, and W. C. Lineberger, Journal of Physical Chemistry A **105** (48), 10822 (2001).

W. Fernando, L. C. Obrien, and P. F. Bernath, Journal of Molecular Spectroscopy **139** (2), 461 (1990).

Z. G. Figen and O. Aytur, Optics Express **13** (13), 4896 (2005).

R. Frerichs, Z. Phys. **20**, 170 (1923).

M. J. Frisch, G. W. Trucks, H. B. Schlegel, G. E. Scuseria, M. A. Robb, J. R. Cheeseman, J. J. A. Montgomery, T. Vreven, K. N. Kudin, J. C. Burant, J. M. Millam, S. S. Iyengar, J. Tomasi, V. Barone, B. Mennucci, M. Cossi, G. Scalmani, N. Rega, G. A. Petersson, H. Nakatsuji, M. Hada, M. Ehara, K. Toyota, R. Fukuda, J. Hasegawa, M. Ishida, T. Nakajima, Y. Honda, O. Kitao, H. Nakai, M. Klene, X. Li, J. E. Knox, H. P. Hratchian, J. B. Cross, C. Adamo, J. Jaramillo, R. Gomperts, R. E. Stratmann, O. Yazyev, A. J. Austin, R. Cammi, C. Pomelli, J. W. Ochterski, P. Y. Ayala, K. Morokuma, G. A. Voth, P. Salvador, J. J. Dannenberg, V. G. Zakrzewski, S. Dapprich, A. D. Daniels, M. C. Strain, O. Farkas, D. K. Malick, A. D. Rabuck, K. Raghavachari, J. B. Foresman, J. V. Ortiz, Q. C. A. G. Baboul, S. Clifford, J. Cioslowski, B. B. Stefanov, G. Liu, A. Liashenko, P. Piskorz, I. Komaromi, R. L. Martin, D. J. Fox, T. Keith, M. A. Al-Laham, C. Y. Peng, A. Nanayakkara, M. Challacombe, P. M. W. Gill, B. Johnson, W. Chen, M. W. Wong, C. Gonzalez, and J. A. Pople, Gaussian 03 (Gaussian Inc., Pittsburgh PA, 2003).

J. García-Prieto, M. E. Ruiz, and O. Novaro, Journal of the American Chemical Society **107** (20), 5635 (1985).

J. García-Prieto, M. E. Ruiz, E. Poulain, G. A. Ozin, and O. Novaro, Journal of Chemical Physics **81** (12), 5920 (1984).

H. Gomez, T. R. Taylor, and D. M. Neumark, Journal of Chemical Physics **116** (14), 6111 (2002).

B. J. Greenblatt, M. T. Zanni, and D. M. Neumark, Journal of Chemical Physics **112** (2), 601 (2000).

M. Guitou-Guichemerre and G. Chambaud, Journal of Chemical Physics **122** (20), 204325 (2005).

D. Hanstorp and M. Gustafsson, Journal of Physics B-Atomic Molecular and Optical Physics **25** (8), 1773 (1992).

M. Hliwa, J. C. Barthelat, M. Pelissier, and F. Spiegelmann, Chemical Physics Letters **132** (2), 205 (1986).

W. Holzer, W. F. Murphy, and H. J. Bernstein, Journal of Chemical Physics **52** (1), 399 (1970).

W. Hong, L. E. Halliburton, D. Perlov, K. T. Stevens, R. K. Route, and R. S. Feigelson, Optical Materials **26** (4), 437 (2004).

K. Huber and G. Herzberg, *Molecular Spectra and Molecular Structure, Constants of Diatomic Molecules*. (Van Nostrand Reinhold, New York, 1979).

Y. S. Kim, Y. J. Jung, and K. H. Jung, Journal of Chemical Physics **107** (10), 3805 (1997).

N. V. Kondratyuk, A. A. Shagov, K. L. Demidchik, A. M. Yurkin, and A. E. Kokh, Quantum Electronics **30** (3), 253 (2000).

K. P. Lawley, D. Austin, J. Tellinghuisen, and R. J. Donovan, Molecular Physics **62** (5), 1195 (1987).

R. Mabbs, K. Pichugin, and A. Sanov, Journal of Chemical Physics **122** (17), 174305 (2005).

R. Mabbs, K. Pichugin, E. Surber, and A. Sanov, Journal of Chemical Physics **121** (1), 265 (2004).

R. Mabbs, E. Surber, and A. Sanov, Journal of Chemical Physics **122** (5), 054308 (2005).

C. M. Marian, Journal of Chemical Physics **94** (8), 5574 (1991).

J. Martin. (Personal Communication)

W. S. McGivern, R. J. Li, P. Zou, T. Nguyen, and S. W. North, Chemical Physics **249** (2-3), 237 (1999).

L. Minnhagen, Arkiv för fysik **21** (5), 415 (1962).

F. Misaizu, K. Tsukamoto, M. Sanekata, and K. Fuke, Surface Review and Letters **3** (1), 405 (1996).

R. S. Mulliken, Journal of Chemical Physics **55** (1), 288 (1971).

F. Muntean, M. S. Taylor, A. B. McCoy, and W. C. Lineberger, Journal of Chemical Physics **121** (12), 5676 (2004).

M. E. Nadal, P. D. Kleiber, and W. C. Lineberger, The Journal of Chemical Physics **105** (2), 504 (1996).

M. E. Nadal, P. D. Kleiber, and W. C. Lineberger, Journal of Chemical Physics **105** (2), 504 (1996).

M. T. Nguyen, M. A. McGinn, and N. J. Fitzpatrick, Journal of the Chemical Society-Faraday Transactions II **82**, 1427 (1986).

M. T. Nguyen, M. A. McGinn, and N. J. Fitzpatrick, Journal of Chemical Society, Faraday Transitions **82** (2), 69 (1986).

J. Niu, B. K. Rao, P. Jena, and M. Manninen, Physical Review B **51** (7), 4475 (1995).

M. Ostermeyer, K. Mittler, and R. Menzel, Physical Review A **59** (5), 3975 (1999).

G. A. Ozin and C. Gracie, Journal of Physical Chemistry **88** (4), 643 (1984).

G. A. Ozin, J. G. McCaffrey, and D. F. McIntosh, Pure and Applied Chemistry **56** (1), 111 (1984).

E. G. Para, E. Martinez, and J. M. Alvarino, Journal of Quantitative Spectroscopy & Radiative Transfer **30** (5), 439 (1983).

R. Parson, J. Faeder, and N. Delaney, Journal of Physical Chemistry A **104** (43), 9653 (2000).

J. Pittner and P. Jungwirth, Chemical Physics Letters **321** (3-4), 281 (2000).

R. Pouamerigo, M. Merchan, I. Nebotgil, P. A. Malmqvist, and B. O. Roos, Journal of Chemical Physics **101** (6), 4893 (1994).

D. T. Radzykewycz, C. D. Littlejohn, M. B. Carter, J. O. Clevenger, J. H. Purvis, and J. Tellinghuisen, Journal of Molecular Spectroscopy **166** (2), 287 (1994).

R. S. Ram, P. F. Bernath, and J. W. Brault, Journal of Molecular Spectroscopy **113** (2), 269 (1985).

T. M. Ramond, G. E. Davico, R. L. Schwartz, and W. C. Lineberger, Journal of Chemical Physics **112** (3), 1158 (2000).

V. M. Rao, M. L. P. Rao, and P. T. Rao, Journal of Quantitative Spectroscopy & Radiative Transfer **25** (6), 547 (1981).

G. J. Rathbone, T. Sanford, D. Andrews, and W. C. Lineberger, Chemical Physics Letters **401** (4-6), 570 (2005).

U. Ringström, Arkiv för fysik **32**, 211 (1966).

M. E. Ruiz, J. García-Prieto, and O. Novaro, Journal of Chemical Physics **80** (4), 1529 (1984).

T. Sanford, D. Andrews, J. Rathbone, M. Taylor, F. Muntean, M. Thompson, A. B. McCoy, R. Parson, and W. C. Lineberger, Faraday Discussions **127**, 383 (2004).

T. Sanford, S. Y. Han, M. A. Thompson, R. Parson, and W. C. Lineberger, Journal of Chemical Physics **122** (5), 054307 (2005).

T. J. Sanford, Ph.D. Thesis, University of Colorado, 2004.

A. Sanov, T. Sanford, L. J. Butler, J. Vala, R. Kosloff, and W. C. Lineberger, Journal of Physical Chemistry A **103** (49), 10244 (1999).

A. Sanov, T. Sanford, S. Nandi, and W. C. Lineberger, Journal of Chemical Physics **111** (2), 664 (1999).

J. Y. Seto, Z. Morbi, F. Charron, S. K. Lee, P. F. Bernath, and R. J. Le Roy, Journal of Chemical Physics **110** (24), 11756 (1999).

M. Shapiro, M. J. J. Vrakking, and A. Stolow, Journal of Chemical Physics **110** (5), 2465 (1999).

P. E. M. Siegbahn, M. R. A. Blomberg, and C. W. Bauschlicher Jr., Journal of Chemical Physics **81** (3), 1373 (1984).

A. Stolow, A. E. Bragg, and D. M. Neumark, Chemical Reviews **104** (4), 1719 (2004).

H. Su, S. H. Tang, Y. Q. Qin, W. J. Zhang, and A. L. Liu, Journal Of The Optical Society Of America B-Optical Physics **21** (12), 2102 (2004).

E. Surber, R. Mabbs, and A. Sanov, Journal of Physical Chemistry A **107** (40), 8215 (2003).

M. A. Thompson and R. Parson. (Personal Communication)

T. D. Varberg and K. M. Evenson, Journal of Molecular Spectroscopy **164** (2), 531 (1994).

J. Verdeyen, *Laser Electronics*, 3 ed. (Prentice Hall, Upper Saddle River, 1995).

P. Vogt, M. Schmitt, and W. Kiefer, Chemical Physics Letters **243** (1-2), 64 (1995).

M. J. J. Vrakking, D. M. Villeneuve, and A. Stolow, Journal of Chemical Physics **105** (13), 5647 (1996).

X. F. Wang, L. Andrews, L. Manceron, and C. Marsden, Journal of Physical Chemistry A **107** (41), 8492 (2003).

S. Y. Wang, A. Paul, N. J. DeYonker, Y. Yamaguchi, and H. F. Schaefer, Journal of Chemical Physics 123 (1) (2005).

Imaging in Molecular Dynamics Technology and Applications, edited by B. Whitaker (Cambridge University Press, 2003).

W. C. Wiley and I. H. McLaren, Review of Scientific Instruments **26** (12), 1150 (1955).

E. Wrede, S. Laubach, S. Schulenburg, A. J. Orr-Ewing, and M. N. R. Ashfold, Chemical Physics Letters **326** (1-2), 22 (2000).

A. J. Yencha, R. J. Donovan, A. Hopkirk, and D. Shaw, Journal of Physical Chemistry **92** (19), 5523 (1988).

J. M. Yu. Anikeev, Optical and Quantum Electronics **31**, 545 (1999).

T. Yukiya, N. Nishimiya, and M. Suzuki, Journal of Molecular Spectroscopy **214** (2), 132 (2002).

R. N. Zare, *Angular Momentum*. (Wiley, New York, 1988).

C. G. Zhan and S. Iwata, Chemical Physics Letters 232 (1-2), 72 (1995).

L. Zhang, D. H. Li, Q. L. Zhang, C. Y. Li, Z. Y. Wei, B. H. Feng, P. M. Fu, and Z. G. Zhang, Optics Communications **250** (1-3), 174 (2005).

X. N. Zheng, M. C. Heaven, and J. Tellinghuisen, Chemical Physics Letters **195** (2-3), 273 (1992).

X. N. Zheng, M. C. Heaven, and J. Tellinghuisen, Journal of Molecular Spectroscopy **164** (1), 135 (1994).

Appendix A. Laser Fundamentals

The laser system utilized in the photoelectron imaging spectrometer is a Coherent Infinity XPO laser system, utilizing a pulsed Nd:YAG laser. The laser system has its fundamental laser pulse created in a diode-pumped solid state (DPSS) laser, producing 1064 nm using an Nd:YAG prism in a ring resonator, capable of producing a repetition rate between 0.1 – 100 Hz. The pulse exiting the DPSS takes a dual pass through a flashlamp-pumped Nd:YAG rods amplifying the 1064 nm laser pulse. Amplification of the fundamental is controlled by the user between 1 – 600 mJ. The amplified pulse undergoes frequency doubling in an angle tuned BBO crystal producing 532 nm pulses. The residual 1064 nm pulses is combined with the 532 nm pulses in another angle tuned BBO crystal producing 355 nm pulses, the third harmonic of the laser. At this point the 355 nm laser pulse is the most intense, and is either utilized in a optical parametric oscillator (OPO) followed by frequency doubling allowing for the formation of 210 – 600 nm pulses or the pulses out of the OPO are utilized as is after being separated from the residual 1064 and 532 nm laser pulses.

The 355 nm pulses that are used for pumping the OPO undergo a difference frequency mixing in a double pass BBO cavity, producing a signal and idler beam. The idler beam is tunable from 710 – 2000 nm, while the signal beam is tunable between 410 – 710 nm. The signal beam is then doubled in an angle tuned BBO crystal and compensator. The OPO system has a limitation as the signal and idler beams approach each other, reaching the degeneracy of the OPO. As the OPO approached the degeneracy the line width of the laser pulses increases exponentially.

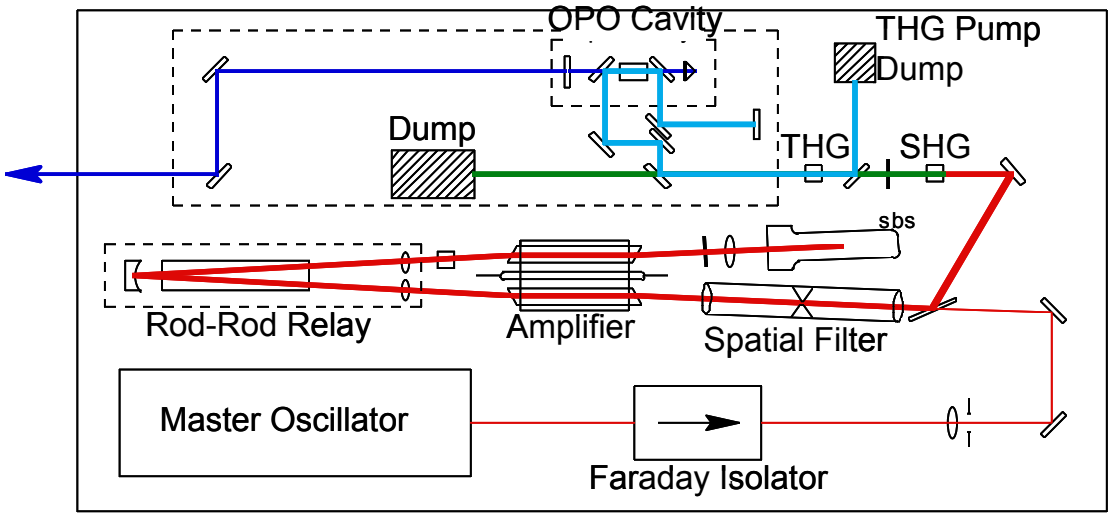

Figure A.1 *Optical Components of the Infinity XPO Laser System*

The heart of the Infinity system, consists of two Neodymium-doped Yttrium Aluminum Garnet (Nd:YAG) rods. They are used as the gain medium for the laser system. The pumping of the Nd:YAG rods with a flash lamp promotes electron in the gain medium into an excited state. The configuration of the electrons is limited according to the laws of quantum mechanics which also limit how the energy of the excited electrons can be released. The excited system can be stimulated to return to the ground state. When this occurs, a photon with identical properties to the incoming one is emitted. The process is called stimulated emission and it is the underlying mechanism of all laser action. It provides a way of generating large numbers of identical photons in a controlled way. Stimulated emission occurs with a probability of B_{21} that is related to the spontaneous emission A_{21} in equation A.1:

$$\frac{A_{21}}{B_{21}} = \frac{8\pi n^2 n_g h\nu^3}{c^3}. \qquad \text{(A.1)}$$

If there are N_2 numbers of excited systems, the de-excitation rate due to stimulated emission can be written as $B_{21}\, N_2\, P$, where P is the pumping rate, which is related to the energy density in the external field.

If the system is in the ground state when it is exposed to an external field oscillating at its resonance frequency, it can absorb an energy quantum and end up in an excited state through a process called stimulated absorption. The two processes, stimulated absorption and emission are symmetrical with respect to each other. This symmetry means that an incoming photon does not distinguish between the upper and lower energy states; hence they occur with equal probability, i.e., $B_{21} = B_{12}$.

The processes just described are called radiative since they involve the creation or annihilation of a photon. In addition to these processes, there are also various nonradiative de-excitation and excitation mechanisms such as collisions with other systems and electron

impact. Under normal conditions all of these processes occur simultaneously.

Since stimulated emission is the process by which laser light is generated, we would like to arrange things so that this process dominates over the others. The only way to do this is to have a greater number of systems in the higher-lying state so that $B_{21} N_2 > B_{12} N_1$. In other words, $N_2 > N_1$. The situation when there are more systems in the higher-lying state is called population inversion. It is a necessary condition for lasing action to take place. It is not possible to achieve population inversion in a two-level system[1,2]. A higher-level system is required to achieve population inversion, with a minimum of three and preferably four levels.

The Nd:YAG system has a four level scheme (Figure A.2). It has a narrow fluorescence line width that displays a low-lasing threshold and high gain. By pumping the Nd:YAG rods with 1.53 eV of energy to an excited state, the electron quickly relaxes to the $^4F_{3/2}$ level. This is a long lived state, $\tau \approx 230$ μs. The transition taking place is the $^4I_{11/2} \leftarrow {}^4F_{3/2}$. It has an energy separation of 1.16 eV, corresponding to a wavelength of 1064 nm. From the $^4I_{11/2}$ state the electron quickly decays down to the $^4I_{9/2}$ ground state.

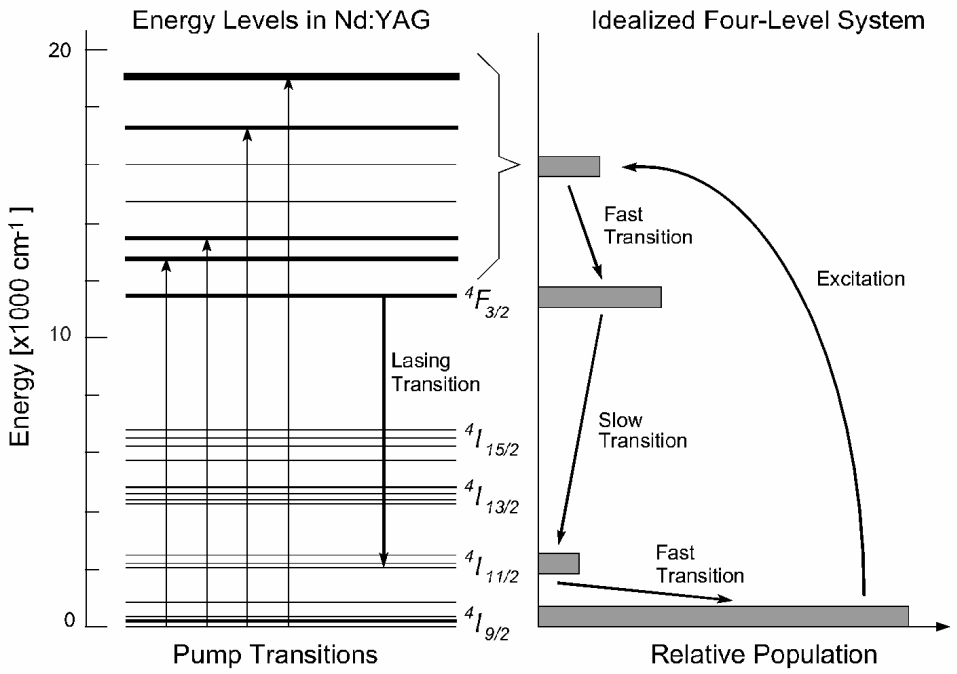

Figure A.2 *Energy Levels for a Nd:YAG System and a Four Level System*

Placing the Nd:YAG rods within a resonator allows for the feedback necessary for a stimulated emission process. It also confines the laser field within the gain medium. In the case of our laser system, the resonator consists of several optics and cells used for the confinement of the beam and control of the beam properties.

The flash lamp for pumping the Nd:YAG rods creates a thermal gradient across the rod diameter, because radiation from the flash lamp is absorbed into the rods. The temperature gradient, in turn, gives rise to a stress gradient because the hotter regions in the center of the rod will try to expand more than the cooler surface regions. The resulting stress gradient gives rise to a refractive index gradient across the rod surface. Since the radial and tangential stress components are different, the refractive indices along these two directions will be different as well. As a consequence the electromagnetic vector components of the incoming radiation along the radial and tangential directions will experience different refractive indices, resulting in the two waves travel at different speeds through the rods.

The pulse exhibits horizontal polarization as it enters the first amplifying rod. Because of the difference in refractive index along the radial and tangential directions, the exiting pulse has acquired an elliptical polarization in all points across its spatial mode except for those that coincide with the two diameters that are parallel and perpendicular to the polarization state of the incoming pulse. If the pulse exiting the first rod, exhibiting elliptical polarization, is allowed to directly propagate through the second rod, the degree of ellipticity will increase, i.e., double.[1]

After the pulse has been reflected in the Stimulated Brillouin Scattering Cell (SBS Cell) and passed through the two rods a second time, the vertically polarized component will be reflected out of the laser amplifier by the thin-film polarizer. If the polarization state is poorly defined as the beam strikes the thin-film polarizer, a large fraction of it will end up in the Faraday isolator. This energy is not available in the output beam, and it can also disturb

the stability of the oscillator. It is important that the beam is in a well-defined polarization state as it goes through the quarter-wave plate positioned between the second rod and the SBS cell.

To compensate for the phase difference induced by the birefringence in the first rod, a 90° polarization rotator is positioned between the two rods. Light entering the first rod (from the left), which has vertical polarization, will experience a phase retardation between the radial and tangential components. Before the pulse enters the second rod, the polarization is rotated 90°. The component that was radial in the first rod is now tangential, and the tangential component in the first rod is now the radial. The phase retardation that was induced in the first rod will be compensated by the second rod; the net result will be light that is again linearly polarized, but now rotated 90°. The same correction will take place as the pulse goes through its second pass through the rods; the net result will be vertically linearly polarized light.

When light waves are scattered by density waves in a medium, a backwards-traveling and frequency-shifted component can be created in a process called Brillouin scattering. The density waves can be excited thermally or by the laser field itself. In the latter case, this phenomenon is called Stimulated Brillouin Scattering, or SBS. As is typical for processes that are self amplifying, a threshold must be exceeded for it to occur. As a long as the fluency is below this threshold value, the process does not take place at all. When the fluency exceeds the threshold value, the signal grows exponentially until the onset of saturation. When the leading edge of the laser pulse returns through the rods, it will decrease the gain. The effect of this can be seen in the trailing end of the laser pulse where there is a sudden drop in intensity.[3,4]

Typically a Chlorofluorocarbon (CFC) is used in a SBS Cell. In the case of the Infinity laser, CFC_{113} is used (CFC_{113} is CCl_2FCClF_2). The laser beam is focused out of the Nd:YAG rod into the SBS Cell, while in the cell the field generated in the backwards

direction by SBS is also the phase conjugate of the incident field. The beam profile is restored to its original shape as opposed to a distorted beam shape. No polarization information is retained in the phase conjugate process. The polarization state of the beam is not reversed or corrected; these effects occur in the oscillator and beam path.

Primarily 1064 nm radiation is emitted from the Nd:YAG rods. However, most applications require wavelengths in the visible to ultraviolet range. We achieve this wavelength shift with a fundamentally nonlinear processes known as harmonic generation. With the advent of lasers, it became possible to create electric fields large enough to saturate the polarization of a dielectric medium. This technique did not permit the induction of a polarization on the dielectric medium that related to the electric-field strength in a linear way. As a result, the polarization relationship can be thought of as a Taylor-series expansion, giving rise to nonlinear terms.

$$P = \varepsilon \mathrm{X} E, \qquad P = \varepsilon(\mathrm{X}_1 E + \mathrm{X}_2 E^2 + \mathrm{X}_3 E^3 + \ldots), \tag{A.2}$$

where E is the electric field vector, ε is the permittivity of free space, and X is the electrical susceptibility that is characteristic for the polarized material. When the polarization relationship is expanded, it gives rise to higher-order nonlinear susceptibilities. These higher-order susceptibility terms are typically small compared to the first-order term unless the electric field is very large; then the nonlinear terms have an effect on the field.[2]

The oscillations of the electric field can be described by the function

$$E = E_0 \sin(\omega t). \tag{A.3}$$

By substituting this value into the polarization term in A.2 we obtain

$$P = \varepsilon \mathrm{X}_1 E \sin(\omega t) + \frac{1}{2} \varepsilon \mathrm{X}_2 E^2 (1 - \cos(2\omega t)) + \ldots . \tag{A.4}$$

The second-order term shows that a wave having twice the frequency of the fundamental wavelength can be formed in a nonlinear medium. This is Second Harmonic Generation, or SHG.

To generate power in the second harmonic, the phase of the two waves must match. This is where phase matching must come into play. It is achieved through the birefringence of the materials being used. There is an angle Θ_m for which the refractive index of the fundamental beam is equal to the refractive index of the frequency-doubled beam. By changing the angle at which the beam propagates into the crystal, we allow phase matching to occur in the crystal via frequency doubling. The refractive indices for both the incoming and frequency-doubled beams, are temperature dependent. Thus phase matching of the beams can be tuned by adjusting the temperature of the crystal. If the temperature of the crystal changes once phase matching has been achieved, the efficiency of the doubling will decrease because of improper overlap of the phases. The heating of the crystal to a constant temperature followed by phase matching of the waves, reduces the chances of the crystal heating and reduce the efficiency of the doubling due to a change in the refractive indexes.

Higher-order harmonic generation is accomplished by frequency mixing in a second crystal. Third Harmonic Generation is accomplished by frequency mixing of 1064 nm radiation and frequency-doubled radiation in a second crystal that is phase matched with the two incoming beams. Since energy is conserved, the resulting wavelength is given by

$$\frac{1}{\frac{1}{1064}+\frac{1}{532}},$$

qual to 355 nm radiation. Fourth Harmonic Generation is accomplished via doubling of the 532 nm radiation, yielding 266 nm radiation. The crystal utilized for producing the Second, Third and Fourth Harmonic generation is a BBO Crystal.[2,5,6]

At the heart of the system is a tunable Optical Parametric Oscillator (OPO). The OPO consists of a nonlinear crystal. In this case it is a beta barium borate (BBO) crystal. The Third Harmonic (355 nm) pump laser beam is passed through the first of two BBO crystals, and two wavelengths come out (Figure A.3). The two are the signal (shorter wavelength) and idler beams (longer wavelengths). The relationship between the wavelengths is strictly given by the equation:

$$\frac{1}{\lambda_{pump}} = \frac{1}{\lambda_{signal}} + \frac{1}{\lambda_{idler}} \text{ or in frequency } \nu_{pump} = \nu_{signal} + \nu_{idler} . \qquad \text{(A.5)}$$

As long as this condition is met and the phase matching condition is satisfied, the parametric device will provide tunable gain.[1]

By passing the signal output beam through a second BBO crystal we produce a second Harmonic effect on the signal beam. All the conditions for frequency doubling of the signal output must be met as was true when the 1064 nm light was doubled. Phase matching of the signal beam and of the output beam must occur. This is done through tuning the angle of the crystal, to maximize the phase matching.

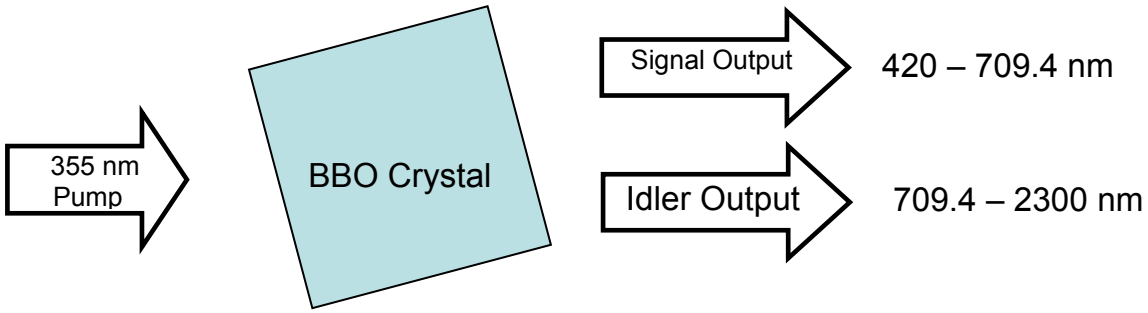

Figure A.3 *Schematic for 1st Crystal in OPO Cavity*

The simplest type of optical parametric oscillator consists of a crystal placed between two mirrors that provide optical feedback at either the signal or idler wavelengths. An oscillation is created within the cavity to provide the feedback, just like in a laser.

For gain to be present in a parametric device, there has to be proper synchronization of the optical phases of the three interacting waves. The optical phases differs from the gain medium of a laser where the gain is only dependent on the intensity of the pump beam, with no dependence on its phase or direction. The phase matching condition in OPOs is typically obtained by using a birefringent crystal. By changing the orientation of the crystal, we change the index of refraction of the crystal. Since the wavelength is dependent upon the index of refraction, improper crystal orientation eliminates wavelengths that don't fulfill the condition; thus this method is a means of tuning to different wavelengths.

The Infinity laser contains a Porro prism as an end mirror and a flat output coupler comprising the OPO cavity. The Porro prism allows the two beams to pass through different parts of the nonlinear crystal; the end result is that the forward and backward signal beams see different regions of gain. The active gain angle space is restricted and produces an output of high brightness and coherence.

To pulse the laser, the Infinity laser system consists of a diode-pumped master oscillator consisting of two concave mirrors, a Nd:YAG prism, and an acousto-optical modulator arranged to form a ring resonator (Figure A.4). This ring cavity allows for two counter-propagating waves to be present. Only one of these waves is useful; to use the other beam, a loss mechanism is introduced. This mechanism can also be used to Q-switch the cavity. An acousto-optical modulator (AOM) is used in the pulsing of the laser.

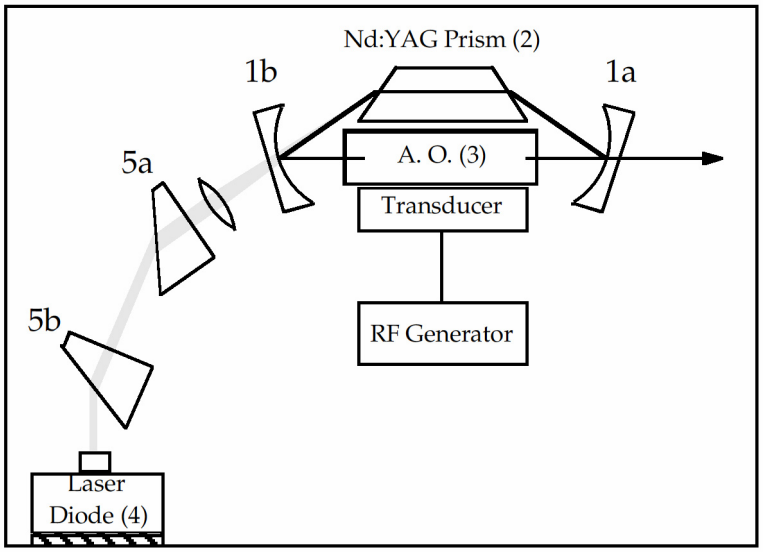

Figure A.4 *Diagram of the Maser Oscillator Cavity*

The acousto-optical modulator serves as the Q-switching mechanism of the laser by regulating the round-trip cavity losses. The way it does this is by diffraction of the optical wave against the acoustical wave induced in the material of the AOM. When the modulator is switched and acoustic wave becomes resonant within the material, periodic variations are set up in the refractive indices of the materials. When the optical wave strikes this refractive index grating, two beams are created. One is shifted up and the other down by the frequency of the acoustic wave, because of photon-phonon interactions within the medium.[1,7-10]

By switching the acoustic field, energy is diffracted out of the main beam, resulting in the loss mechanism. As the transducer is switched off, the acoustic wave decays, allowing the beam to pass through the crystal without any loss, thereby creating a laser pulse until the transducer is switched back on. Since there are two waves within the oscillator, one wave is able to pass through undisturbed, creating a continuous wave laser with only minimal power. This second wave acts as a seed for allowing the next laser pulse to build up in power.

A Faraday isolator is utilized in the scheme of the laser to prevent back-scattering light from the amplifier from going into the oscillator and damaging it. The Faraday isolator rotates the polarization of light 45º in a uniform manner. The amount of polarization rotation is given by $\theta = VfH_z dz$, where θ is the polarization rotation angle, V is the Verdet constant of the optical element being used, f is the frequency of radiation, H_z is the longitudinal component of the magnetic intensity vector, and dz if the optical path length. The Faraday isolator consists of two polarizers sandwiched in between a high-strength rare earth permanent magnet. The incoherent light traveling in the forward direction becomes polarized (vertically in our case) by the input polarizer. The Faraday rotator will rotate the polarization 45° to the right, while the output polarizer will allow all the light to escape and continue. Light traveling in the backward direction becomes polarized (45° to the right in this case) by

the output polarizer. The Faraday rotator will rotate the polarization 45° more to the right so that it is horizontally polarized. The input polarizer, which is vertically aligned, will block this light. The reason to use a Faraday isolator as opposed to a 1/4 wave plate is the rotation of the radiation is insensitive to the direction of propagation. This feature allows for better isolation of the light polarization, allowing for greater beam stability.[1]

By placing an amplifier after the oscillator high power output is obtained. The optical setup in the Infinity is a multipass configuration. This allows the amplifier to be used both as a small signal amplifier (first pass) and as a low-gain and high-energy-extraction efficiency amplifier (second pass). Amplifying the beam noise in the form of amplification of spontaneous emission (ASE) is a problem. ASE will decrease the energy available to the lasing beam, because of saturation of the amplification medium, producing an incoherent beam. The ASE is minimized through spatial filters. Because ASE diverges quickly, it can easily be eliminated from the laser emission.

As stated before, the Infinity system utilizes two Nd:YAG rods. It is a challenge to control the pulse traveling through the amplifier, since both rods must experience the same relative environment. Assuming that the two rods are close to identical and symmetrically loaded, the beam in the first rod must be imaged into the second rod. The imaging, performed by two lenses and a concave mirror, is done so that the transverse coordinates remain unaltered while the coaxial coordinates are flipped around the center of the rods (Figure A.5). This arrangement not only performs part of the polarization control, but also compensates for small residual asymmetries in the pumping of the rods. The relay cell is inserted in the beam path to avoid laser-induced air breakdown at the focal points formed by the imaging system.

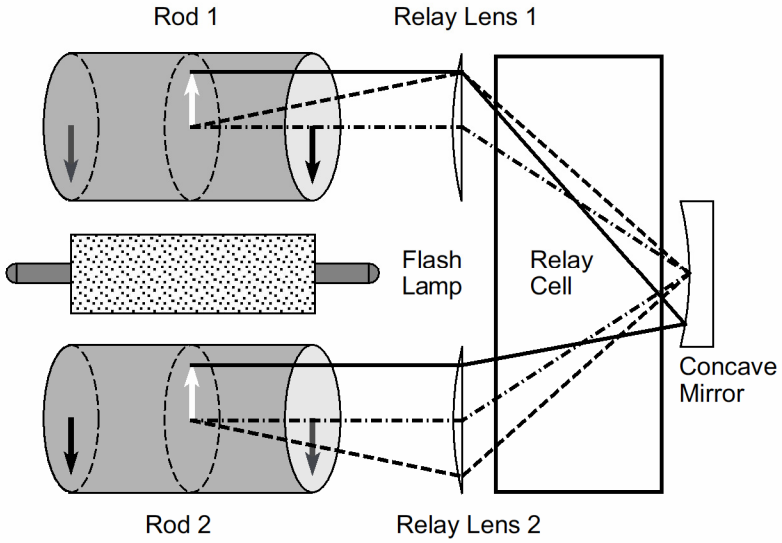

Figure A.5 *Diagram for Nd:YAG rod assembly, including imaging of beam onto rods*

Several types of optical components readily found in other laser systems can also be found in the Infinity XPO laser system. However, their arrangement is unique to this laser system. By utilizing the space in the laser head, an efficient laser cavity was developed. Through the use of an AOM and a Q-switch, pulses on the order of 3 ns and a repetition rate ranging from 10–100 Hz can easily be created. High gain is obtained because of the dual Nd:YAG rods. This ability to obtain high gain in a short pulse was coupled to a tunable OPO cavity. The ability for continuous tunablility from 210–2300 nm through the OPO system allows this laser system to be very efficient in producing almost any wavelength needed without requiring a dye laser.

References for Appendix A

1 Coherent, *Coherent Laser Systems*. (Coherent, Santa Clara, CA, 2000).

2 J. Verdeyen, *Laser Electronics*, 3 ed. (Prentice Hall, Upper Saddle River, 1995).

3 S. H. V. Bruckner, S. Ludwig, Journal of Modern Optics **40** (2), 187 (1993).

4 J. M. Yu. Anikeev, Optical and Quantum Electronics **31**, 545 (1999).

5 W. Hong, L. E. Halliburton, D. Perlov, K. T. Stevens, R. K. Route, and R. S. Feigelson, Optical Materials **26** (4), 437 (2004).

6 N. V. Kondratyuk, A. A. Shagov, K. L. Demidchik, A. M. Yurkin, and A. E. Kokh, Quantum Electronics **30** (3), 253 (2000).

7 Z. G. Figen and O. Aytur, Optics Express **13** (13), 4896 (2005).

8 M. Ostermeyer, K. Mittler, and R. Menzel, Physical Review A **59** (5), 3975 (1999).

9 H. Su, S. H. Tang, Y. Q. Qin, W. J. Zhang, and A. L. Liu, Journal Of The Optical Society Of America B-Optical Physics **21** (12), 2102 (2004).

10 L. Zhang, D. H. Li, Q. L. Zhang, C. Y. Li, Z. Y. Wei, B. H. Feng, P. M. Fu, and Z. G. Zhang, Optics Communications **250** (1-3), 174 (2005).

Appendix B. Photoelectron Simulations of CuH

The following section contains several photoelectron simulations performed in the PESCAL program. All simulations are of the neutral CuH molecule in its ground electronic state. All neutral parameters were held constant, with an equilibrium bond length of 1.46263 Å and a vibrational frequency of 1835 cm^{-1}. The only parameter held constant on the anion was that of the calculated frequency of 1564 cm^{-1}. With the anion bond length varied between 1.534 and 1.600 Å in 0.003 Å steps, a best fit was obtained by comparing the second vibration and the level of the background noise.

All graphs have the ^2S state of copper neutral present, and the ground electronic $^1\Sigma$ state of copper hydride plotted in black. All graphs are plotted with the electron kinetic energy (eKE) on the x-axis and the photoelectron counts on the y-axis. Each graph has the corresponding simulated anion bond length on the graph, with the fit plotted in red and a corresponding stick spectrum indicating the position of the peak plotted in blue.

The graphs are arranged in decreasing order starting with 1.600 Å and ending with 1.534 Å. Each simulation was performed as an independent Morse oscillator, with each peak having a Gaussian profile with a 10 meV distribution at full-width at half-maximum. From these graphs the, anion bond length is estimated to be 1.567(3) Å.

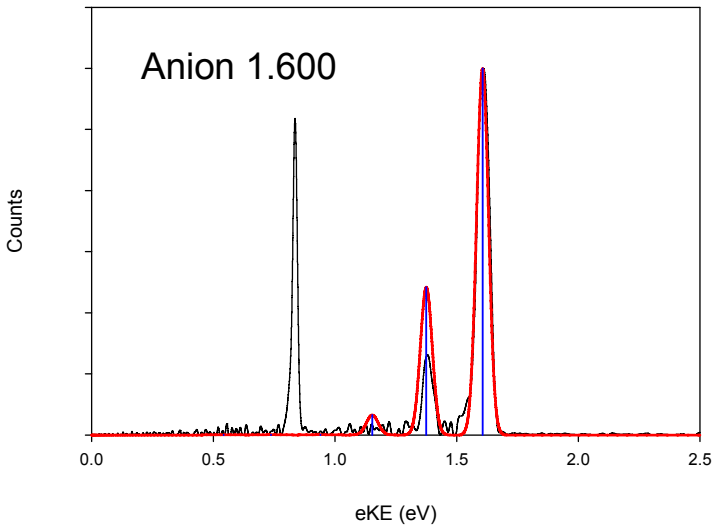

Figure B.1 ***Simulated spectra of the CuH neutral ground state with an anion bond length of 1.600 Å and a neutral bond length of 1.46263 Å.***

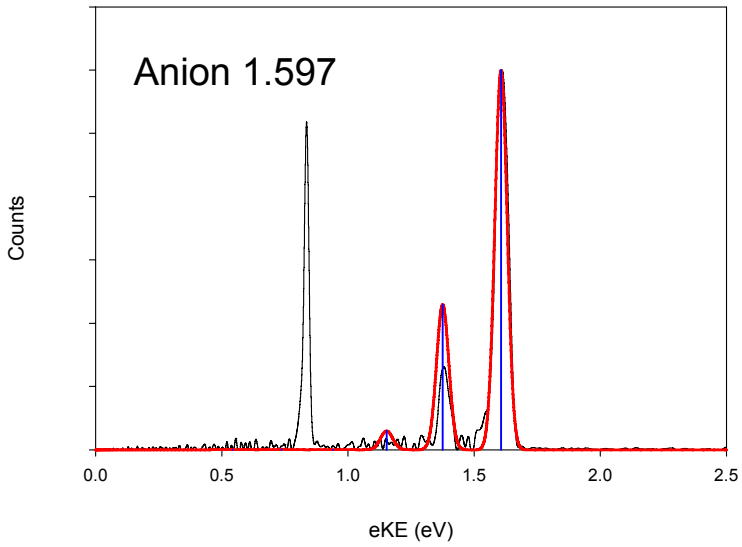

Figure B.2 ***Simulated spectra of the CuH neutral ground state with an anion bond length of 1.597 Å and a neutral bond length of 1.46263 Å.***

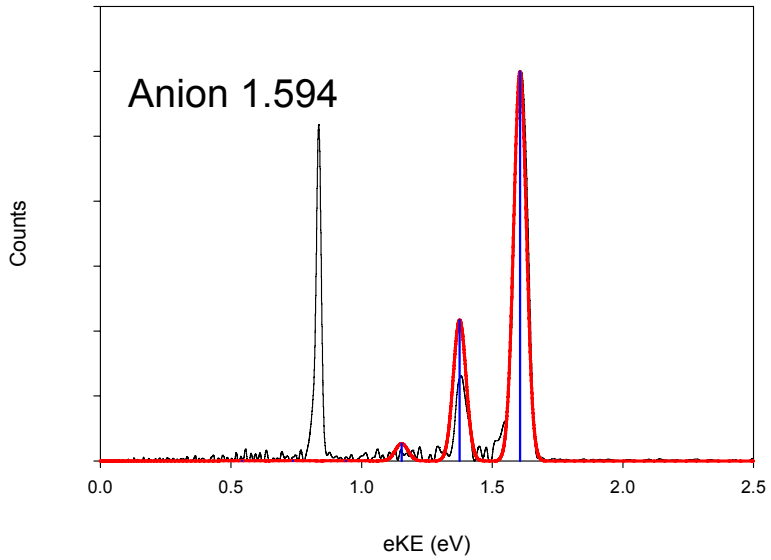

Figure B.3 ***Simulated spectra of the CuH neutral ground state with an anion bond length of 1.594 Å and a neutral bond length of 1.46263 Å.***

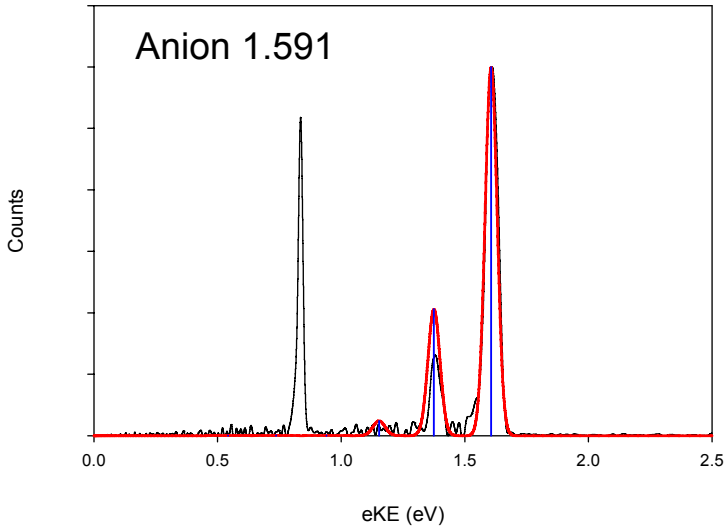

Figure B.4 ***Simulated spectra of the CuH neutral ground state with an anion bond length of 1.591 Å and a neutral bond length of 1.46263 Å.***

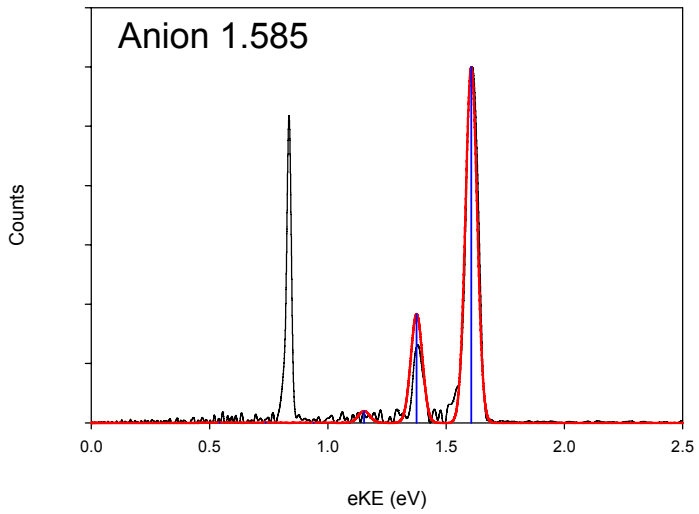

Figure B.5 ***Simulated spectra of the CuH neutral ground state with an anion bond length of 1.585 Å and a neutral bond length of 1.46263 Å.***

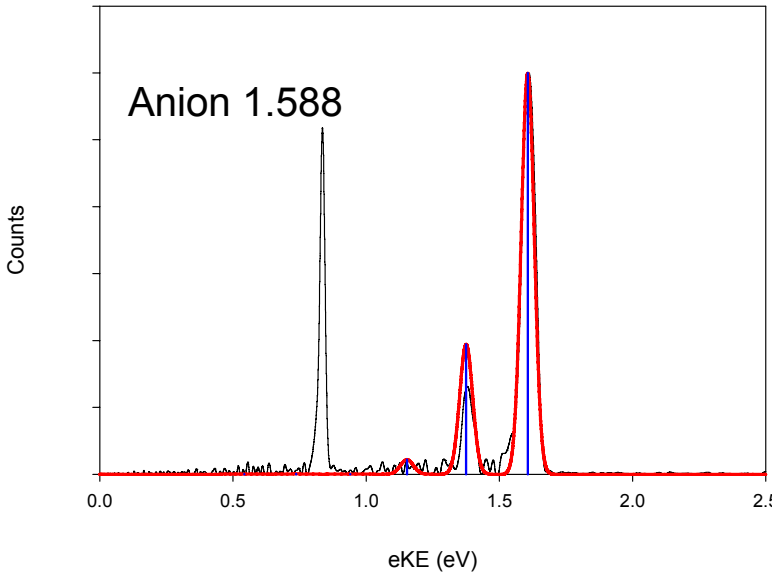

Figure B.6 ***Simulated spectra of the CuH neutral ground state with an anion bond length of 1.588 Å and a neutral bond length of 1.46263 Å.***

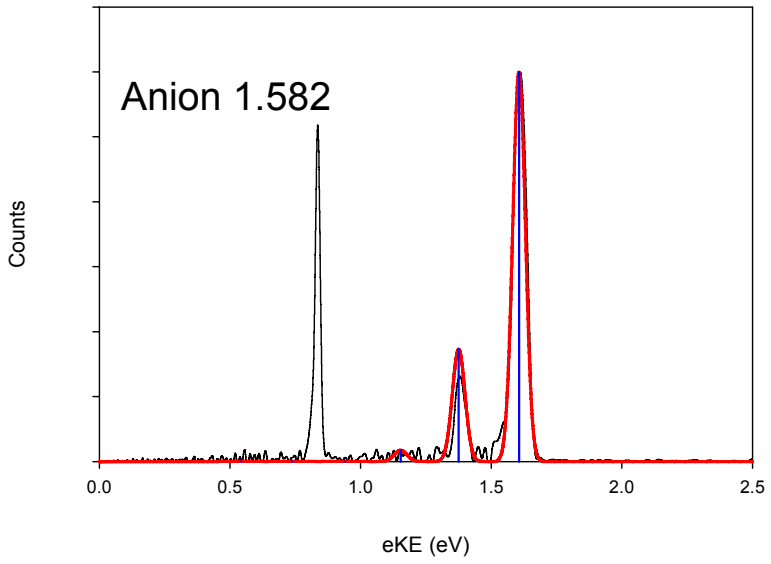

Figure B.7 ***Simulated spectra of the CuH neutral ground state with an anion bond length of 1.582 Å and a neutral bond length of 1.46263 Å.***

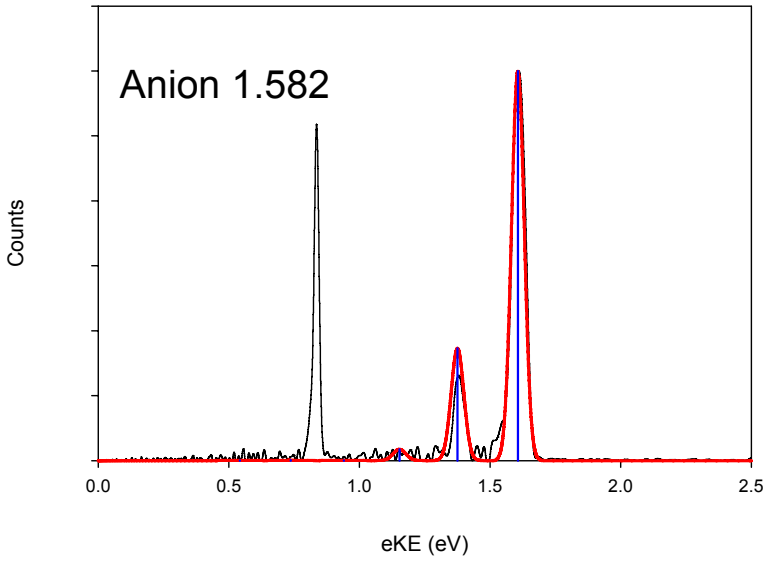

Figure B.8 ***Simulated spectra of the CuH neutral ground state with an anion bond length of 1.582 Å and a neutral bond length of 1.46263 Å.***

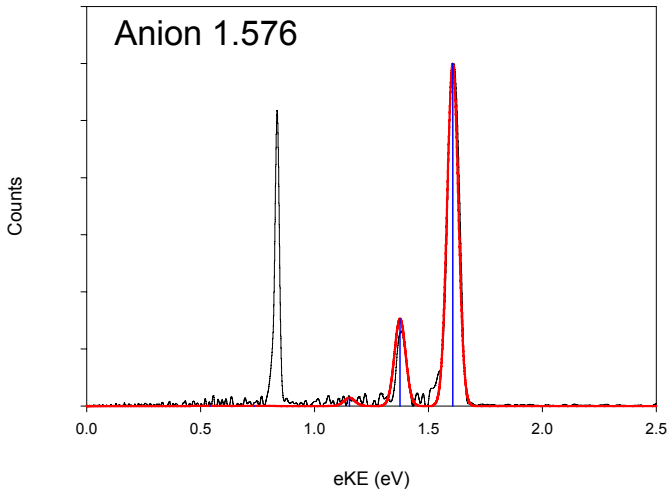

Figure B.9 ***Simulated spectra of the CuH neutral ground state with an anion bond length of 1.576 Å and a neutral bond length of 1.46263 Å.***

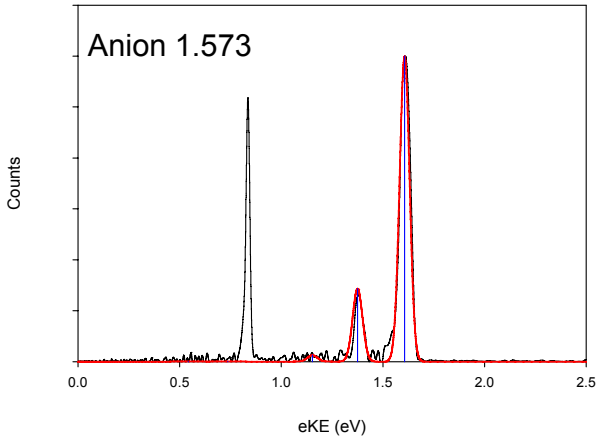

Figure B.10 ***Simulated spectra of the CuH neutral ground state with an anion bond length of 1.573 Å and a neutral bond length of 1.46263 Å.***

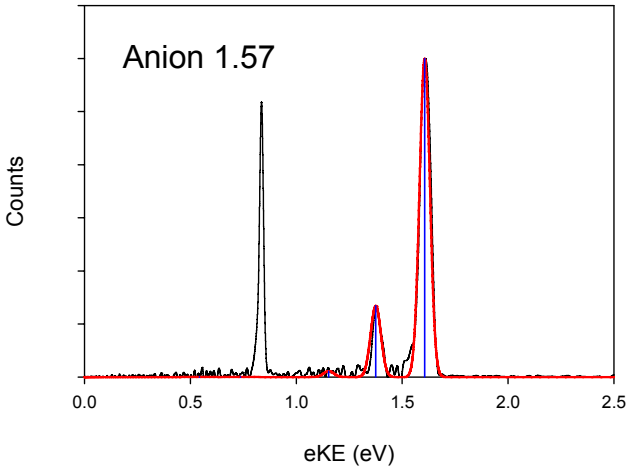

Figure B.11 ***Simulated spectra of the CuH neutral ground state with an anion bond length of 1.570 Å and a neutral bond length of 1.46263 Å.***

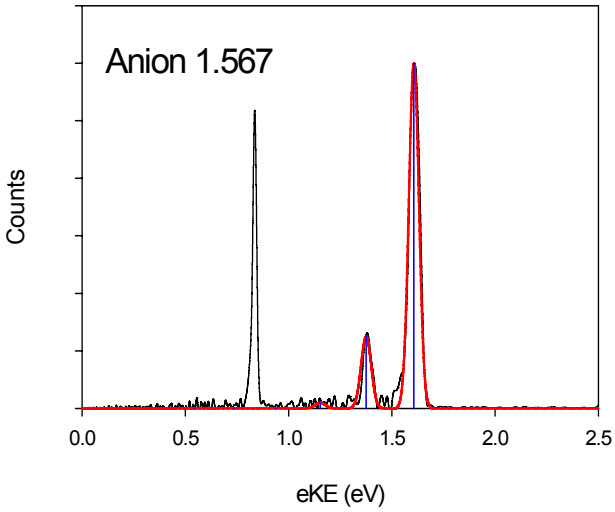

Figure B.12 ***Simulated spectra of the CuH neutral ground state with an anion bond length of 1.567 Å and a neutral bond length of 1.46263 Å.***

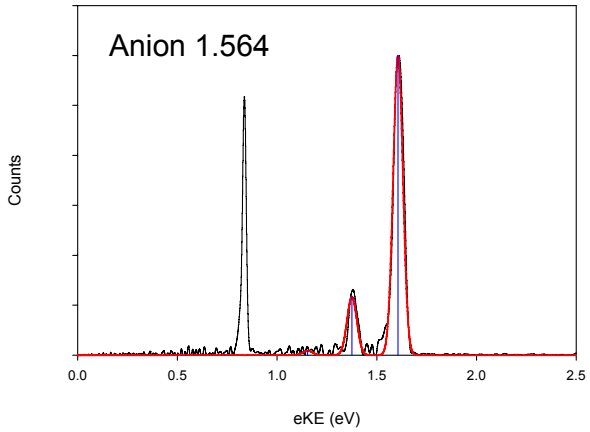

Figure B.13 ***Simulated spectra of the CuH neutral ground state with an anion bond length of 1.564 Å and a neutral bond length of 1.46263 Å.***

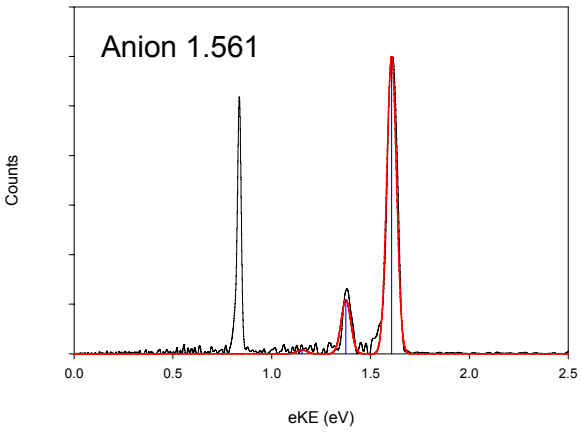

Figure B.14 ***Simulated spectra of the CuH neutral ground state with an anion bond length of 1.561 Å and a neutral bond length of 1.46263 Å.***

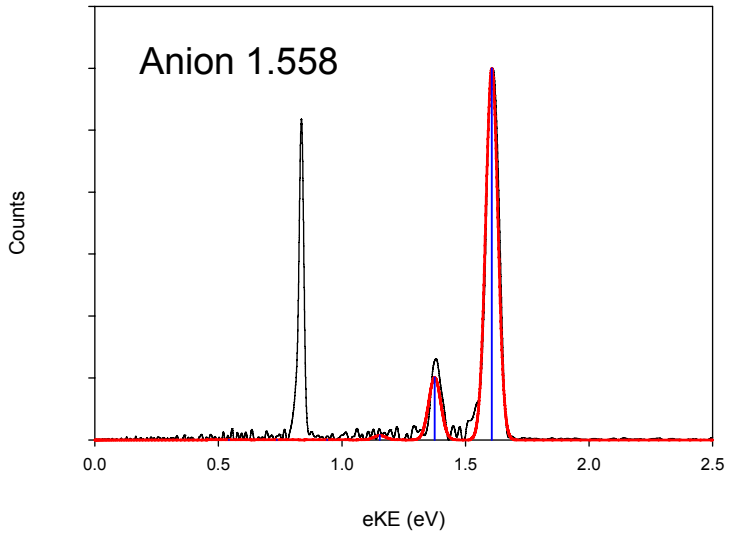

Figure B.15 ***Simulated spectra of the CuH neutral ground state with an anion bond length of 1.558 Å and a neutral bond length of 1.46263 Å.***

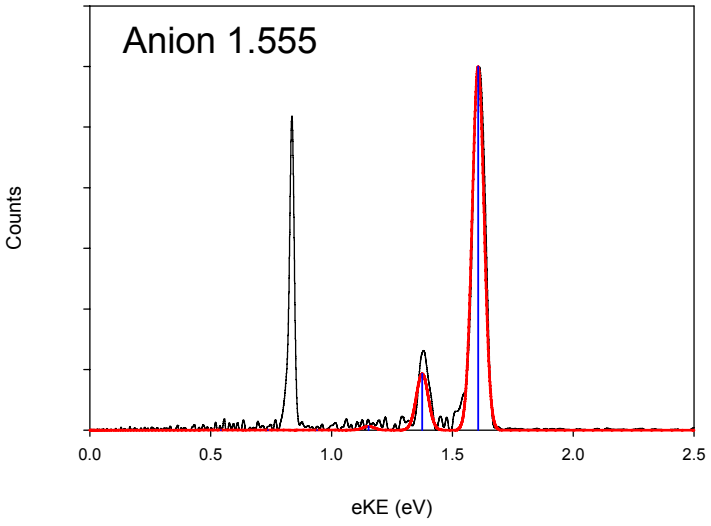

Figure B.16 ***Simulated spectra of the CuH neutral ground state with an anion bond length of 1.555 Å and a neutral bond length of 1.46263 Å.***

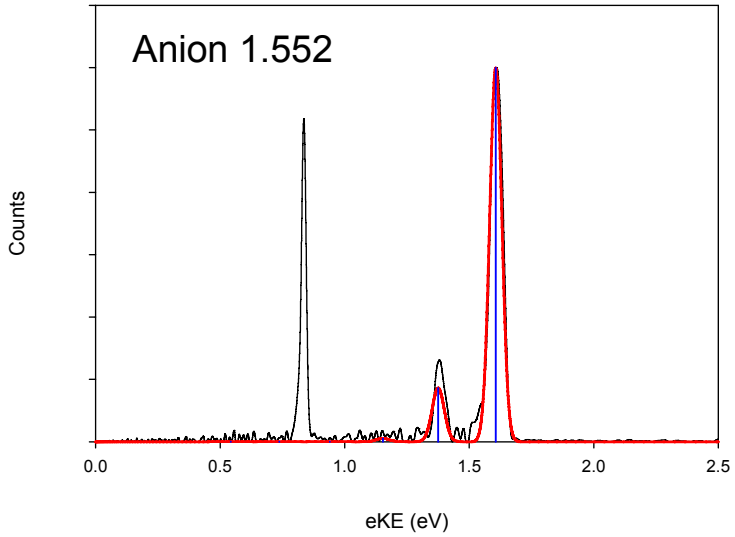

Figure B.17 ***Simulated spectra of the CuH neutral ground state with an anion bond length of 1.552 Å and a neutral bond length of 1.46263 Å.***

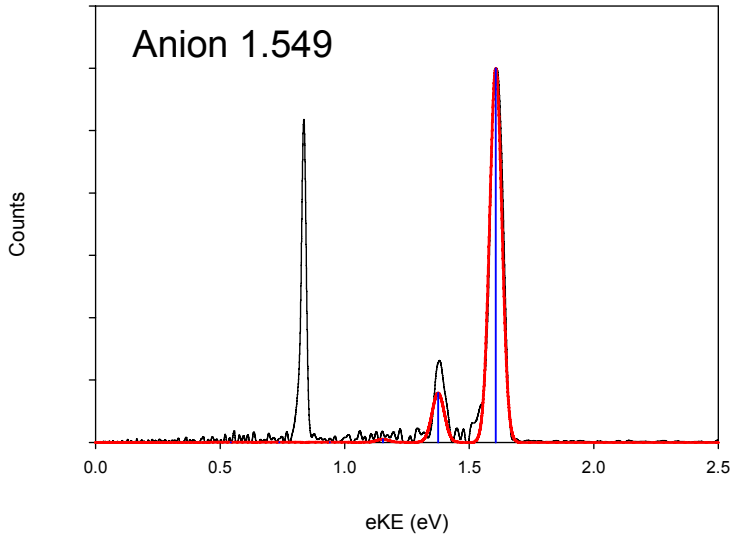

Figure B.18 ***Simulated spectra of the CuH neutral ground state with an anion bond length of 1.549 Å and a neutral bond length of 1.46263 Å.***

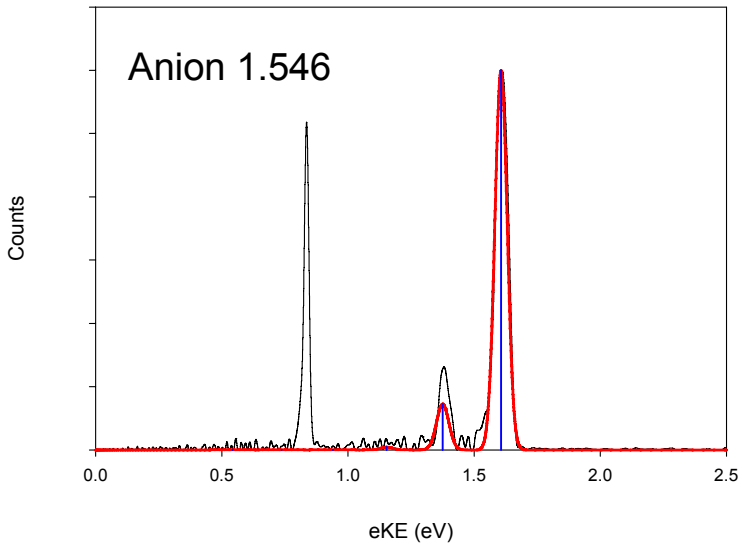

Figure B.19 ***Simulated spectra of the CuH neutral ground state with an anion bond length of 1.546 Å and a neutral bond length of 1.46263 Å.***

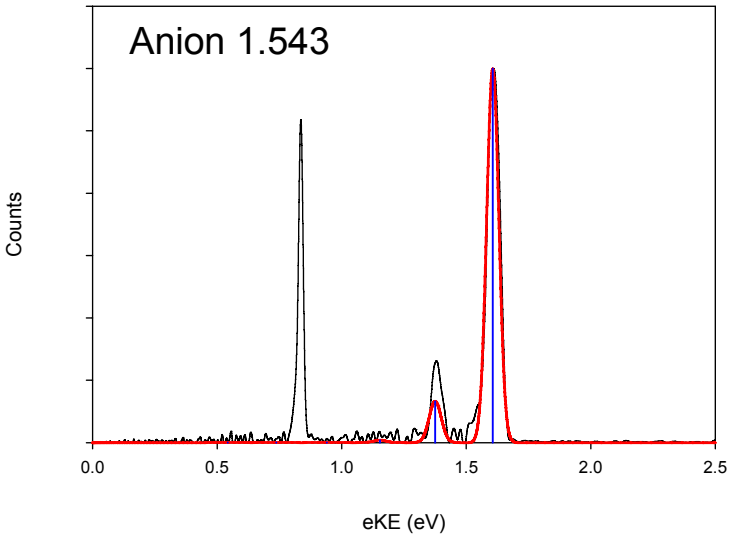

Figure B.20 ***Simulated spectra of the CuH neutral ground state with an anion bond length of 1.543 Å and a neutral bond length of 1.46263 Å.***

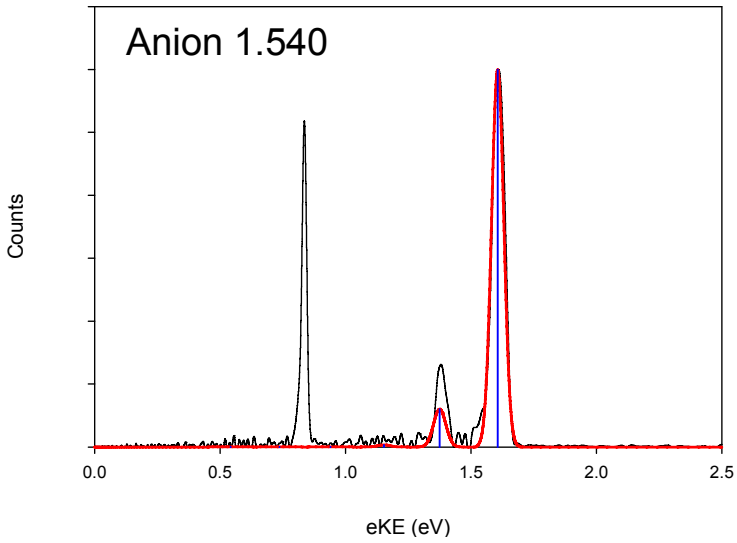

Figure B.21 ***Simulated spectra of the CuH neutral ground state with an anion bond length of 1.540 Å and a neutral bond length of 1.46263 Å.***

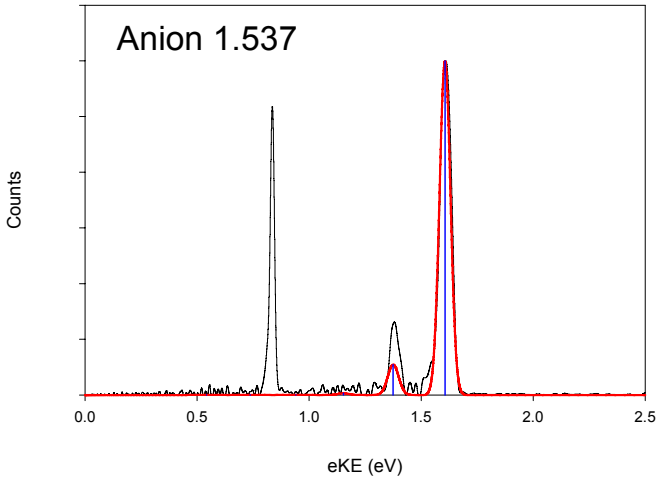

Figure B.22 ***Simulated spectra of the CuH neutral ground state with an anion bond length of 1.537 Å and a neutral bond length of 1.46263 Å.***

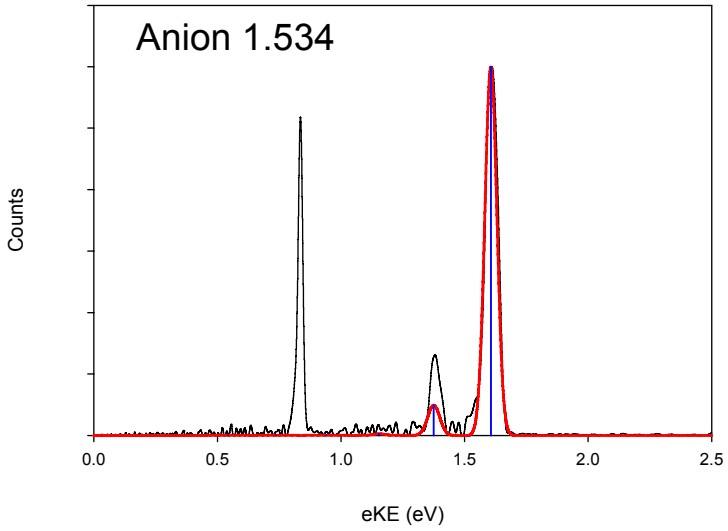

Figure B.23 ***Simulated spectra of the CuH neutral ground state with an anion bond length of 1.534 Å and a neutral bond length of 1.46263 Å.***

Appendix C. Photoelectron Spectra of Copper Hydrides

Appendix C contains the photoelectron spectra of CuD^- and CuH_2^- as they were not included in Chapter 4.

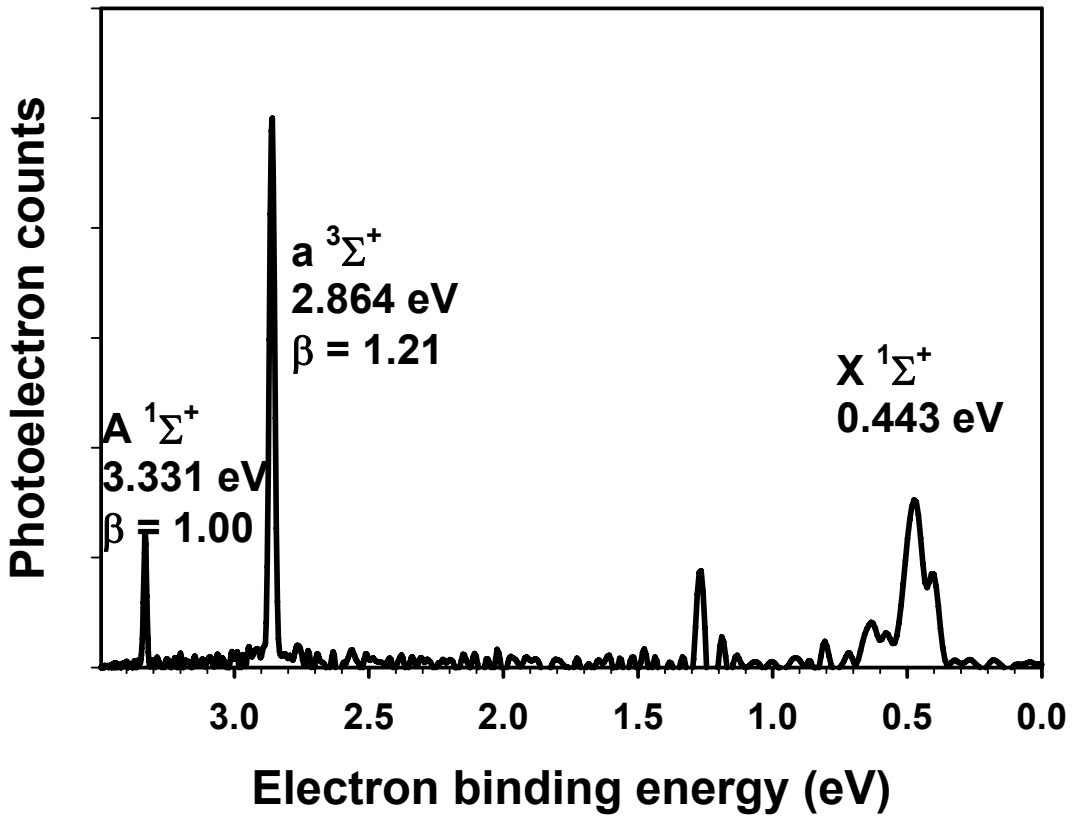

Figure C.1 Photoelectron spectra of CuD^- recorded at 355 nm.

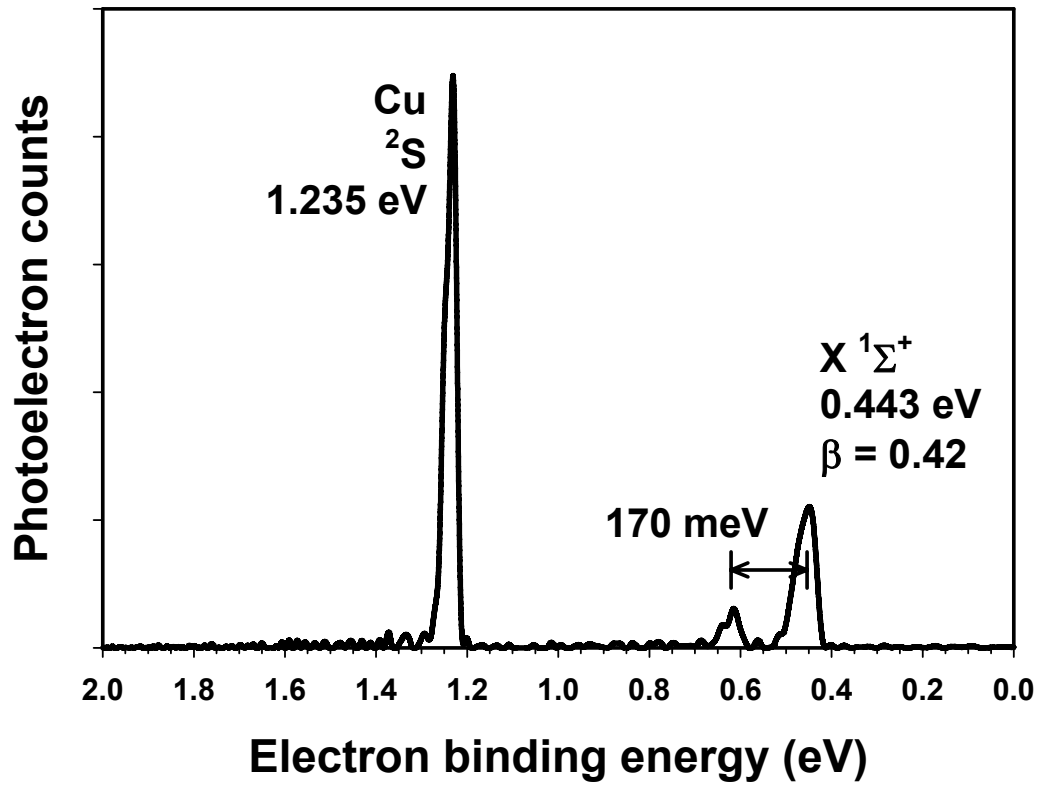

Figure C.2 Photoelectron spectra of CuD^- recorded at 600 nm.

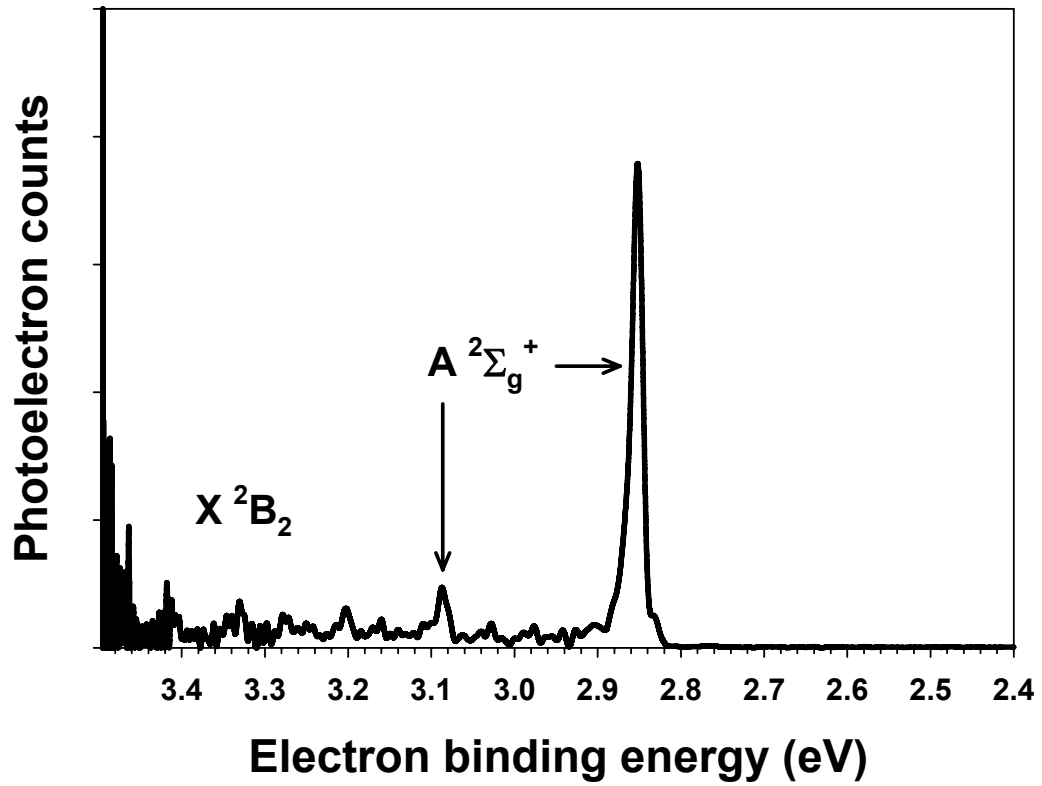

Figure C.3 Photoelectron spectra of CuH_2^- recorded at 355 nm.